



Immunotherapy With 5, 15-DPP Mediates Macrophage M1 Polarization and Modulates Subsequent *Mycobacterium tuberculosis* Infectivity in rBCG30 Immunized Mice

Faraz Ahmad^{1†}, Mohd. Saad Umar¹, Nazoora Khan¹, Fauzia Jamal¹, Pushpa Gupta², Swaleha Zubair³, Umesh Datta Gupta² and Mohammad Owais^{1*}

OPEN ACCESS

Edited by:

Yong-Sung Kim,
Ajou University, South Korea

Reviewed by:

Roland Lang,
University Hospital Erlangen, Germany
Luc Van Kaer,
Vanderbilt University, United States

*Correspondence:

Mohammad Owais
owais_lakhnawi@yahoo.com

†Present address:

Faraz Ahmad,
ICMR-National Institute of Pathology,
New Delhi, India

Specialty section:

This article was submitted to
Vaccines and Molecular Therapeutics,
a section of the journal
Frontiers in Immunology

Received: 07 May 2021

Accepted: 04 October 2021

Published: 29 October 2021

Citation:

Ahmad F, Umar MS, Khan N,
Jamal F, Gupta P, Zubair S, Gupta UD
and Owais M (2021) Immunotherapy
With 5, 15-DPP Mediates
Macrophage M1 Polarization
and Modulates Subsequent
Mycobacterium tuberculosis Infectivity
in rBCG30 Immunized Mice.
Front. Immunol. 12:706727.
doi: 10.3389/fimmu.2021.706727

¹ Molecular Immunology Lab, Interdisciplinary Biotechnology Unit, Aligarh Muslim University, Aligarh, India, ² Bio-Safety Level (BSL)-3 Animal Experimentation Facility, Indian Council of Medical Research (ICMR)-National Japanese Leprosy Mission for Asia (JALMA) Institute for Leprosy and Other Mycobacterial Diseases, Agra, India, ³ Department of Computer Science, Aligarh Muslim University, Aligarh, India

Tuberculosis (TB) is a significant and continuing problem worldwide, with a death toll of around 1.5 million human lives annually. BCG, the only vaccine against TB, offers a varied degree of protection among human subjects in different regions and races of the world. The majority of the population living near the tropics carries a varying degree of tolerance against BCG due to the widespread prevalence of non-tuberculous mycobacteria (NTM). Interestingly, ~90% of the *Mycobacterium tuberculosis* (*Mtb*) infected population restrain the bacilli on its own, which strengthens the notion of empowering the host immune system to advance the protective efficacy of existing mycobacterial vaccines. In general, *Mtb* modulates IL-10/STAT3 signaling to skew host mononuclear phagocytes toward an alternatively activated, anti-inflammatory state that helps it thrive against hostile immune advances. We hypothesized that modulating the IL-10/STAT3 driven anti-inflammatory effects in mononuclear cells may improve the prophylactic ability of TB vaccines. This study investigated the immunotherapeutic ability of a porphyrin based small molecule inhibitor of IL-10/STAT3 axis, 5, 15-diphenyl porphyrin (DPP), in improving anti-TB immunity offered by second generation recombinant BCG30 (rBCG30-ARMF-II[®]) vaccine in mice. The DPP therapy potentiated vaccine induced anti-TB immunity by down-modulating anti-inflammatory responses, while simultaneously up-regulating pro-inflammatory immune effector responses in the immunized host. The employed DPP based immunotherapy led to the predominant activation/proliferation of pro-inflammatory monocytes/macrophages/DCs, the concerted expansion of CD4+/CD8+ effector and central memory T cells, alongside balanced Th17 and Treg cell amplification, and conferred augmented resistance to aerosol *Mtb* challenge in rBCG30 immunized BALB/c mice.

Keywords: tuberculosis, vaccine, immunotherapeutics, IL-10 (interleukin 10), 5, 15-diphenylporphyrin

INTRODUCTION

As a strategy to counter immune onslaught, *Mycobacterium tuberculosis* (*Mtb*), the causative agent of human tuberculosis (TB), evokes anti-inflammatory responses in the host (1–6). It is tempting to speculate that the down-modulation of anti-inflammatory machinery with simultaneous mobilization of pro-inflammatory effectors, may serve as a deliberate host approach to control *Mtb* infection. Several recent studies have established that mononuclear phagocytes are crucial for imparting protection against *Mtb* infection (7–10). Interestingly, they also possess T cell-like memory capacity against re-infection (9, 11, 12). Along this line, the relatively modest potency of TB vaccines developed to date suggests that most of the T-cell targeting candidate TB vaccines do not contribute to any significant advancement in anti-TB prophylaxis programs. This and the above-specified observations, in turn, indicate the need to develop effective prophylactic strategies that can simultaneously activate both innate and adaptive arms of the immune system.

As a crucial component of first-line immune defense, mononuclear phagocytes, especially macrophages, encounter *Mtb* early during an invasion. It is well established that mononuclear phagocytes restrict the replication of invading *Mtb* long before the involvement and participation of specialized T cells (13). The macrophage subpopulation displaying pro-inflammatory classical or M1 phenotypes play a crucial role in the efficient clearance of invading *Mtb* (14). To withstand the immune onslaught, *Mtb* subverts inflicted macrophages to switch toward an anti-inflammatory M2 phenotype (6, 14–16). However, prolonged inflammation in chronic granulomatous infections (*cf. Schistosoma mansoni*) (17) is detrimental and triggers immunopathological consequences in the host. In general exuberant innate inflammation is associated with poor resolution of TB (18). Thus, a well-coordinated and temporally balanced expansion of both pro- and anti-inflammatory monocytes/macrophages is essential for achieving optimal protection against *Mtb*.

The role of IL-10 in exacerbating anti-mycobacterial immunity is well established (19–21) and has been reviewed elsewhere (22). The administration of IL-10 neutralizing monoclonal antibody during BCG vaccination ameliorated protection against subsequent *Mtb* challenge, in both- susceptible and resistant mice strains (23). Furthermore, immunization of IL-10 knockout mice with BCG resulted in elevated anti-mycobacterial immunity upon challenge with *Mtb* (24). Considering these facts, it is tempting to explore strategies that can simultaneously reinforce both the innate and adaptive arms of the immune system as a means to achieve desirable prophylaxis against *Mtb*. On this line, IL-10 mediated activation of JAK-STAT pathway and subsequent STAT3 activity is well established (5, 25, 26). STAT3 is a long established therapeutic target in cancer (27, 28). IL-10 driven STAT3 signaling in macrophages has been associated with the development of ocular angiogenesis and macular degeneration (26). Administration of the small molecule, 5,15-di phenyl porphyrin (DPP), a selective inhibitor of IL-10/STAT3 signaling, has been shown to reduce pathologic neovascularization and Age-related Macular Degeneration (AMD) *via* inhibition of alternative activation and

M2 polarization of macrophages (26). DPP is a small molecular weight organic compound containing a central porphyrin ring similar to phytochrome chlorophyll or heme, an integral component of hemoglobin. Due to its natural origin, it is a relatively safe and attractive STAT3 inhibitor over many other synthetic STAT3 antagonists. The role of the IL-10/STAT3 signaling axis has also been discussed recently in multiple reports, implicating this cascade in modulating monocytes/macrophages toward an anti-inflammatory, alternatively activated state conducive for *Mtb* outgrowth (3, 6, 29–33).

Therefore, targeting and transiently disrupting the IL-10/STAT3 axis mediated immune-suppressive effects could be effective. This study tested this approach to improve the anti-TB efficacy of the second-generation rBCG30-ARMF-II[®] vaccine. The vaccine is devoid of antibiotic resistance marker and expresses 2.6 fold more Ag85B than the original construct (34), which was shown to be safe and immunogenic in a phase 1 clinical trial (35). The rBCG30-ARMF-II[®] vaccine provided improved protection against *Mtb* aerosol challenge than classical BCG in guinea pigs (34). It also induced a strong, cross-protective immune response against *M. leprae* antigens in mice (36).

In the present study, we attempted to bolster rBCG30 mediated anti-TB immunity by modulating host IL-10/STAT3 signaling orchestrated anti-inflammatory effects. We administered DPP, a small molecule inhibitor of the IL-10/STAT3 signaling (26, 37), in mice at the post- rBCG30 vaccination stage (designated as Post Vaccination Immunotherapy or PVI). In an alternative approach, DPP was administered post challenge with *Mtb* in already vaccinated (with rBCG30) animals (herein called Post Infection Immunotherapy or PII). The treatment of mice with DPP resulted in a reduced expansion of pathogen permissive AAMs (Alternatively Activated Monocytes/Macrophages) along with the reciprocal predominance of pro-inflammatory CAMs (Classically Activated Monocytes/Macrophages), the cells that resist the establishment of successful *Mtb* infection. The results of the present study suggest that the modulation of the IL-10/STAT3 axis mediated anti-inflammatory effects can be a viable new anti-TB strategy, especially in vaccinated hosts.

RESULTS

Immunotherapy With DPP Skews Mononuclear Phagocytes Toward a Pro-Inflammatory CAM State

Ly6C⁺ mononuclear phagocytes are largely divided into two subpopulations-Ly6C^{hi} and Ly6C^{low}, which are further defined as pro-inflammatory M1 or CAMs/CADCs and anti-inflammatory M2 or AAMs/AADCs, respectively (38–42). There is a direct correlation between expression of Ly6C and the degree of the functional differentiation state of mononuclear phagocytes following infection with *Mtb* (42, 43), and other intracellular pathogens (17, 40). Considering this, we intended to restrict the *Mtb* induced polarization of monocytes/macrophages/DCs toward permissive AAMs/AADCs. We treated rBCG30-immunized animals with DPP, either before (PVI) or after (PII) challenge

with *Mtb*, to transiently block IL-10/STAT3 mediated anti-inflammatory signaling. Transient blockade of IL-10/STAT3 signaling was used as a means to allow augmented differentiation of mononuclear phagocytes into pathogen-clearing CAMs/CADCs. Interestingly, immunotherapy with DPP in rBCG30-immunized animals (PVI) resulted in significant up-regulation of CAM phenotype in monocytes/macrophages, while fewer monocytes/macrophages with AAM phenotype were present among both peritoneal exudates cells (PEC) population (**Figure S1**) and splenic mononuclear cells (**Figure S2**). DPP immunotherapy in rBCG30 vaccinated animals post-challenge with *Mtb* (PII) also resulted in significant augmentation of the CAMs among monocyte/macrophage population from peritoneal exudates (**Figures 1A, B**). Although in the spleen, only monocytes were significantly expanded into CAMs, while macrophages were predominantly AAMs, when compared with either controls or other experimental groups (**Figures 1C, D**).

The relative abundance of splenic CAMs/CADCs and AAMs/AADCs was assessed at 4- and 8-weeks PC 4- and 8-weeks PC as well. At 4 week PC, rBCG30 immunized animals (administered with either PVI or PII) displayed augmented expansion of both monocytes and DCs with pathogen restricting classical phenotype (CAMs/CADCs). While there was a concomitant reduction in the frequency of the pathogen permissive cells bearing alternative phenotype (AAMs/AADCs), as compared to either untreated, BCG- or rBCG30-immunized control groups. In contrast, macrophages from the PII, but not the PVI group, displayed a similar rise in the expansion of CAMs with a relatively reduced expansion of AAMs, when compared with the rBCG30 control animals (**Figure 2**). This increased expansion of CAMs among splenic macrophages from the PII group indicates the systemic induction of M1 polarized environment in infected macrophages, possibly as a direct effect of DPP therapy.

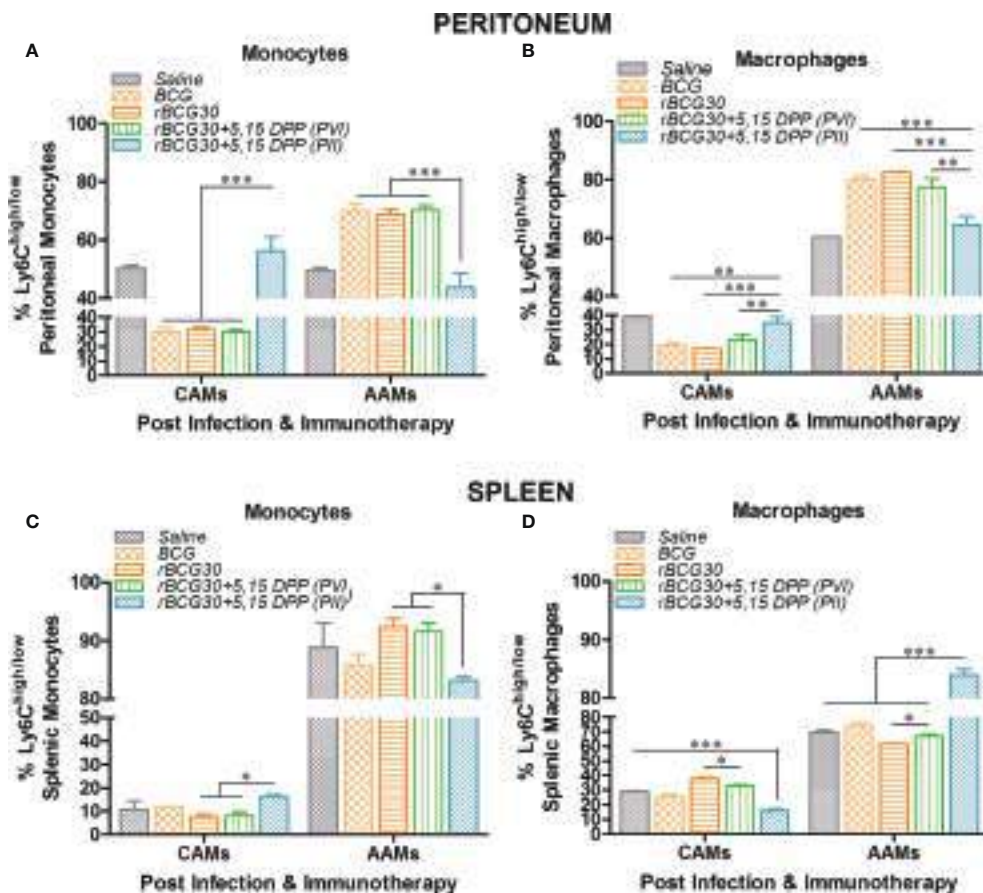


FIGURE 1 | The magnitude and phenotype of peritoneal and splenic monocyte/macrophage populations at 2 weeks post-challenge. Bar graphs in the figure represent percent numbers of Ly6C^{high} CAMs and Ly6C^{low} AAMs among (A, C) CD11b⁺F4/80⁺SSC^{low} monocytes, and (B, D) CD11b⁺F4/80⁺SSC^{low} macrophages. The cells were isolated from either peritoneum (upper panel) or spleen (lower panel) of the mice (n=3) belonging to various experimental groups the next day following completion of post-infection immunotherapy (PII) schedule (2 weeks PC with *Mtb*) and immunophenotyped employing flow cytometry. The results depicted in the figure are representative of two independent experiments and are presented as means \pm SEM of one of the two experiments with similar observations. The statistical significance of the difference between various groups was performed by employing two-way ANOVA followed by Bonferroni's multiple comparison post-test. The *p* values, <0.05(*), <0.01(**), <0.001(***) were considered as significant for analysis and interpretation of experimental data.

Some pathogens, such as *Mtb* (6) and *Brucella* (40) adapt intracellular parasitism and sought shelter in pathogen permissive macrophages of the host. Upon activation, the IL-10/STAT3 axis renders monocytes/macrophages toward an alternative state of activation during *Mtb* infection (6). This generally ensues in the establishment of chronic infection in the host. Taking this into account, we probed the effect of IL-10/STAT3 inhibiting immunotherapy in the modulation of the AAM population during the chronic phase of *Mtb* infection. At week 8 PC, the abundance of CAMs was still significantly higher in the rBCG30 +PPI group, as compared to the rBCG30+PVI group ($p<0.05$,

Figure 3). In addition, the administration of DPP (PII) was successful at restricting the expansion of pathogen permissive AAMs (macrophages) in the rBCG30+PII group even during the late phase of infection, as compared to either rBCG30+PVI or rBCG30 alone groups ($p<0.05$, **Figure 3D**).

DPP Therapy Induces Pro-Inflammatory Cytokines and Dampens the Production of Key Anti-Inflammatory Cytokines

Splenocytes from immunized animals were harvested on day 1 post completion of immunotherapy (either PVI or PII), and

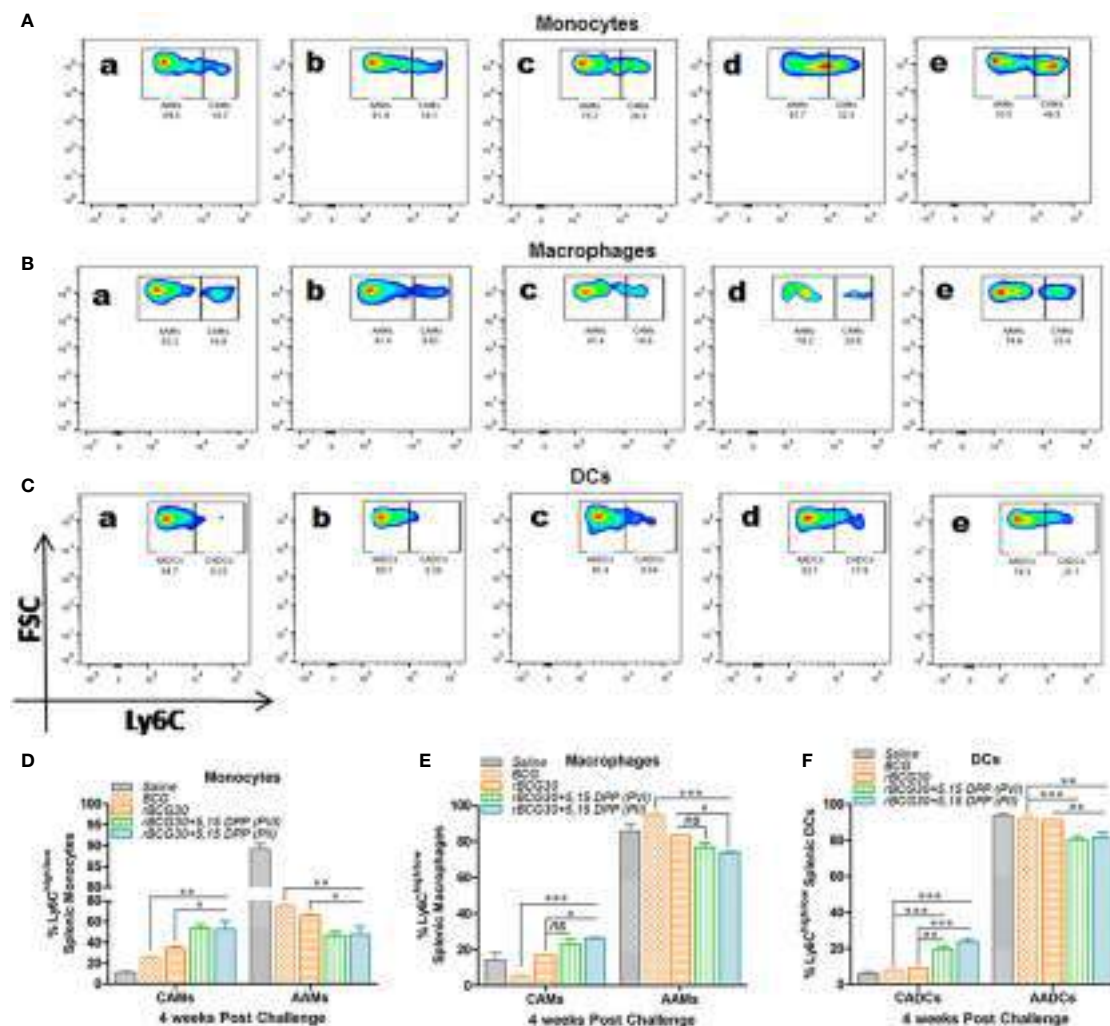


FIGURE 2 | Comparative abundance of the classical and alternative phenotype bearing splenic monocytes/macrophages/DCs at week 4 post-challenge. Representative FACS micrographs (A–C) and corresponding bar graphs (D–F) in the figure represent the percent frequency of Ly6C^{high} CAMs/CADCs and Ly6C^{low} AAMs/AADCs among (A, D) CD11b⁺F4/80⁺SSC^{low} monocytes, (B, E) CD11b⁺F4/80⁺SSC^{low} macrophages, and (C, F) CD11b⁺F4/80⁺SSC^{low} DCs isolated from the spleen of mice belonging to various groups and profiled using flow cytometry. The groups included in the study and depicted in the FACS micrographs were: (a) Saline, (b) BCG, (c) rBCG30, (d) rBCG30+5,15-DPP (PVI), and (e) rBCG30+5,15-DPP (PII). The results depicted in the figure are representative of two independent experiments and are presented as means \pm SEM of one of the two experiments with similar observations. The significance testing of differences between various groups was performed employing two-way ANOVA followed by Bonferroni's multiple comparison post-test. The p values, <0.05 (*), <0.01 (**), <0.001 (***) were considered as significant for analysis and interpretation of data. ns, non-significant.

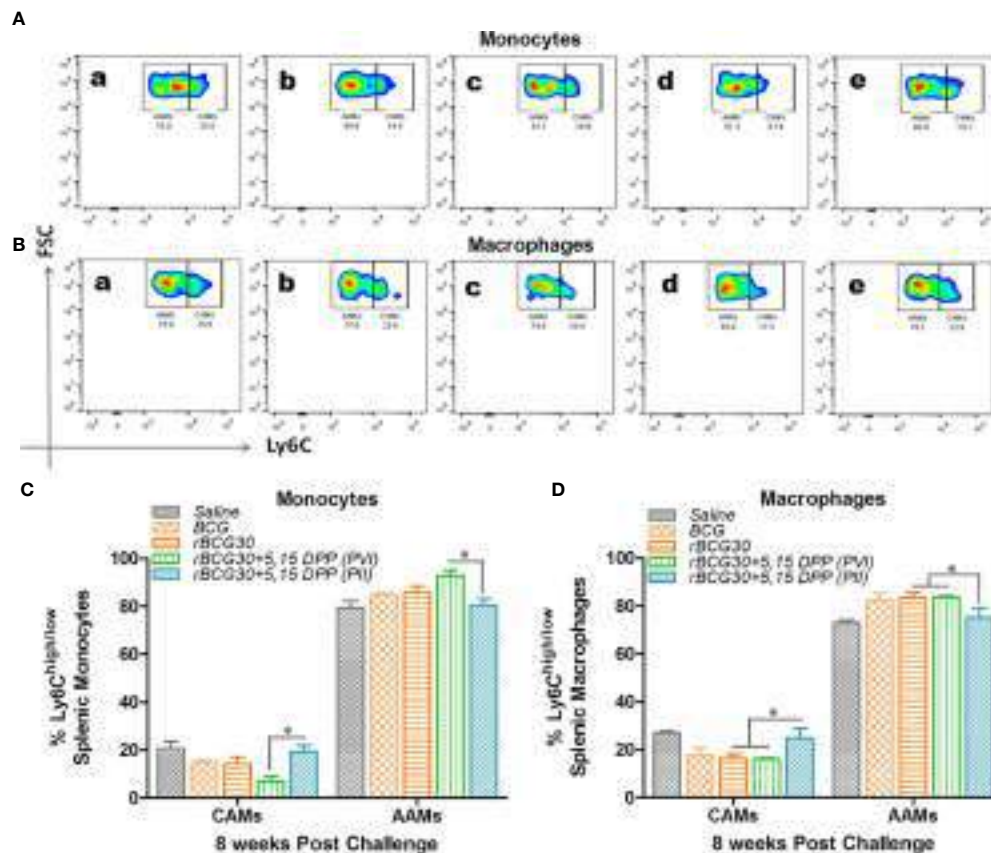


FIGURE 3 | Comparative abundance of classical (CAMs) and alternative (AAMs) splenic monocytes/macrophages at week 8 post-challenge. Representative FACS micrographs and bar graphs in the figure represents the percent frequency of $Ly6C^{high}$ CAMs and $Ly6C^{low}$ AAMs among (A, C) $CD11b^{+}F4/80^{+}SSC^{low}$ monocytes and (B, D) $CD11b^{+}F4/80^{+}SSC^{low}$ macrophages isolated from the spleen of mice ($n=4-5$) belonging to various groups and profiled using flow cytometry. The various groups included in the study and depicted in the FACS micrographs were: (a) Saline, (b) BCG, (c) rBCG30, (d) rBCG30+5,15-DPP (PVI), and (e) rBCG30+5,15-DPP (PII). The results depicted in the figure are representative of two independent experiments and are presented as means \pm SEM of one of the two experiments with similar observations. The significance testing of differences between various groups was performed employing Two-way ANOVA followed by Bonferroni's multiple comparison post-test. The p values, <0.05 (*), <0.01 (**), <0.001 (***) were considered as significant for analysis and interpretation of the data.

cultured *ex vivo* as specified in the method section. Signature anti-inflammatory cytokines IL-10 and IL-4, and pro-inflammatory cytokines IFN- γ , IL-12, IL-1 β , and IL-6, were assessed in the culture supernatant employing sandwich ELISA. The level of Th1 specific pro-inflammatory cytokines, IFN- γ and IL-12, was found to be elevated in animals that received immunotherapy with DPP post vaccination with rBCG30 (PVI). On the other hand, the level of innate pro-inflammatory effectors, either IL-6 or IL-1 β , was not significantly up-regulated, as compared to controls (Figure 4A). However, the employed immunotherapy resulted in diminutive expression of IL-10 and IL-4 cytokines in the culture supernatant. The level of these two cytokines was found to be significantly reduced following DPP treatment in the PVI group (Figure 4B).

The splenocytes obtained from the group of animals vaccinated with rBCG30 and administered DPP for two weeks following *Mtb* challenge (PII scheme) were also assessed for their potential to produce both pro- (IFN- γ , IL-12, IL-1 β , and IL-6) as well as anti- (IL-10 and IL-4) inflammatory cytokines *ex vivo*. Splenic cells from

rBCG30 vaccinated animals (belonging to the PII group) displayed impressive production of Th1 cytokines, IFN- γ , and IL-12 ($p<0.001$, Figure 4C). We observed a significant reduction in the level of anti-inflammatory cytokines IL-10 ($p<0.05$) and IL-4 ($p<0.001$) in the same group of animals, as compared to rBCG30-immunized controls (Figure 4D). Additionally, at 2 weeks PC, the level of either IL-1 β or IL-6 was un-influenced by post-infection immunotherapy, when compared to controls (Figure 4C).

DPP Therapy Up-Regulates Pro-Inflammatory Cytokines Until 8 Weeks Post-Challenge in the Immunized Animals

Splenocytes from various groups of immunized animals were assessed for their potential to produce signature pro- and anti-inflammatory cytokines at 4- and 8-weeks PC. The level of IL-12, the master cytokine of the Th1 cell-mediated immunity, was found to be significantly elevated in the rBCG30+PII group both at 4 ($p<0.001$) and 8 ($p<0.01$) weeks PC (Figure 5A). The expression of IFN- γ , another important effector cytokine of the Th1 type

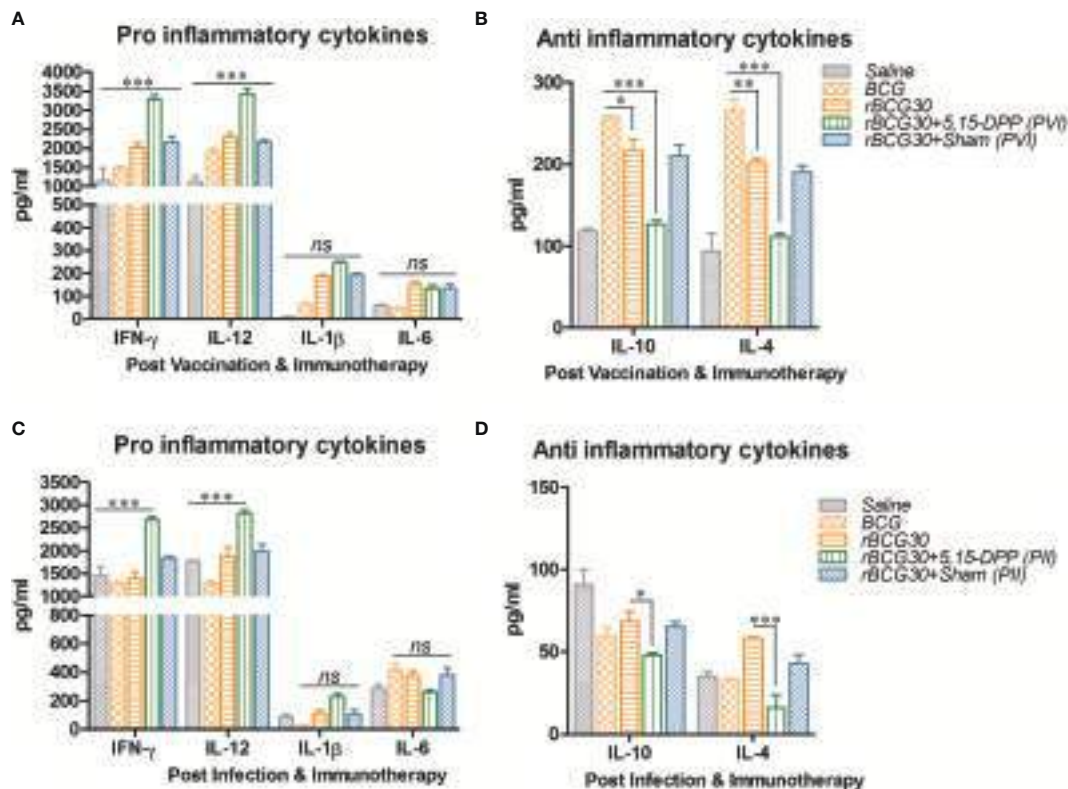


FIGURE 4 | Splenocytes cytokine expression at post vaccination and immunotherapy (PVI) as well as post infection and immunotherapy (PII). The level of signature innate cytokines (IL-1 β and IL-6); Th1 cytokines (IFN- γ and IL-12), and anti-inflammatory cytokines (IL-10 and IL-4), was estimated following (A, B) PVI and (C, D) PII, using sandwich ELISA in the splenocyte culture supernatants belonging to the various immunized groups. Cells were uniformly stimulated with native Ag85B antigen from *Mtb* (5 μ g/ml). Differential expression levels of cytokines in various immunized groups are presented as bar diagrams. The data were analyzed by employing Two-way ANOVA followed by Bonferroni's multiple comparison test and are shown as the means (\pm SEM) of one of the two experiments with similar observations performed in triplicate from the pooled cells of at least three animals per group, where p values; viz. $p < 0.05$ (*), $p < 0.01$ (**), and $p < 0.001$ (***) were considered significant. ns, non-significant.

immunity, was also significantly up-regulated at week 8 PC in the PII group, as compared to rBCG30 alone ($p < 0.001$). There was profuse induction of IFN- γ in the PVI group as well when compared with the rBCG30 alone group ($p < 0.01$) (Figure 5D).

We then assessed another crucial pro-inflammatory cytokine IL-6 in various groups of immunized animals. The cytokine IL-6, besides being a crucial effector of innate immune response in TB (12), is also critical for amplification of Th17 cells responses in *Mtb* infected animals (44). Contrary to the 2 week PC time point (Figure 4C), the level of IL-6 was up-regulated significantly in rBCG30-immunized animals belonging to the PII group at both 4 ($p < 0.001$) and 8 ($p < 0.01$) weeks PC time points (Figure 5B). The level of IL-6 was almost identical in rBCG30+PVI, BCG and saline administered groups of animals at both 4 and 8 weeks PC time points.

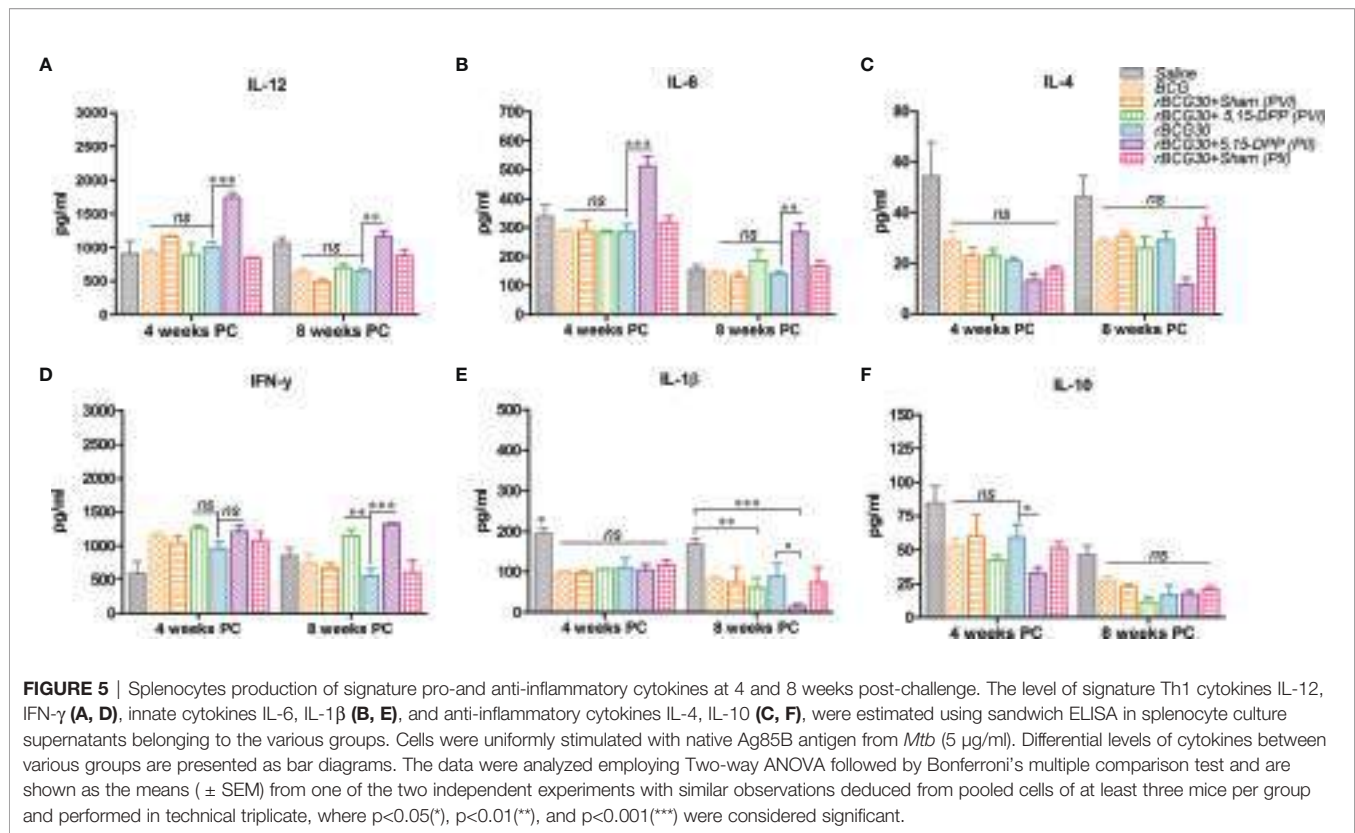
IL-1 β , an important innate cytokine, is primarily a product of either NLRP3 or AIM2 inflammasome assembly and is reported to play a crucial role in regulating the outcome of *Mtb* infection (18, 45). The level of IL-1 β was not significantly influenced by either of the immunotherapeutic strategies employed, until up to 4 weeks PC. Instead, the IL-1 β level was found to be increased in

the saline (*Mtb* infection control) group, as compared with all other experimental or control groups ($p < 0.05$) (Figure 5E). On the other hand, there was a considerable decrease in IL-1 β levels in both the rBCG30+PVI ($p < 0.01$) and rBCG30+PII ($p < 0.001$) groups at week 8 PC (Figure 5E).

The level of signature anti-inflammatory cytokines, IL-10 and IL-4, was probed at stipulated time points post *Mtb* challenge. At 2 weeks PC, the level of both IL-10 and IL-4 was significantly reduced in the rBCG30+PII group (Figure 4D). In contrast, at later time points (4 and 8 weeks PC), differences waned, especially the level of IL-4 (Figure 5C). However, the level of IL-10, the main regulator of anti-mycobacterial immunity, remained low at 4 weeks PC in animals vaccinated with rBCG30 and treated with DPP following *Mtb* challenge (PII) (Figure 5F).

Post-Infection Immunotherapy With DPP Strengthened the Expansion of CD4+ Multifunctional T Cells

Induction of functionally superior multifunctional T cells (MFTs) following immunization and/or infection is an important feature of T cell mediated immunity. Multifunctional T cells are known as



important anti-pathogen effectors that are crucial for immunity and protection against intracellular infectious agents including *Mtb* (46–50). The abundance of antigen specific CD4 $^{+}$ T cells induced in various immunized and immunotherapy groups were assessed *ex vivo* for simultaneous expression of Th1 effector cytokines (IFN- γ and TNF- α) at 2 as well as 4 weeks PC (Figure 6). Interestingly, rBCG30-immunized animals treated with DPP following *Mtb* challenge (PII scheme) produced significantly more CD4 $^{+}$ MFTs, as compared with rBCG30 alone ($p < 0.05$) or rBCG30+PVI group ($p < 0.01$) at 2 weeks PC. In contrast, PVI treated animals did not induce any better level of CD4 $^{+}$ MFTs either at 2 or 4 weeks PC, as compared to rBCG30 controls ($p > 0.05$) (Figures 6A, C). The frequency of CD4 $^{+}$ MFTs induced in saline, BCG, and rBCG30+PVI administered animals was almost identical at 2 weeks PC (Figure 6C). The MFTs response was further evaluated at 4 weeks PC; however, no statistically significant difference was found among experimental or control groups. Nevertheless, the level of induced CD4 $^{+}$ MFTs was still higher in PII treated animals compared to all other immunized groups (Figures 6B, D).

DPP Based Immune-Modulation Scheme Ensues in Development of Effector as Well Central T Cell Memory Following *Mtb* Challenge

Splenocytes isolated from various experimental and control animals were evaluated at 2 week PC for the presence of

central (CD44 $^{\text{high}}$ CD62L $^{\text{high}}$) as well as effector (CD44 $^{\text{high}}$ CD62L $^{\text{low}}$) memory phenotype on both CD4 $^{+}$ and CD8 $^{+}$ T cell population. As is evident from Figure 7, IL-10/STAT3 directed therapy PC with *Mtb* (PII) resulted in an early and significant expansion of effector memory T cells (Tem) in rBCG30 vaccinated mice. Animals in the rBCG30+PII group had a significantly higher percentage of CD4 $^{+}$ and CD8 $^{+}$ Tem cells than animals in either rBCG30 or rBCG30+PVI groups ($p < 0.001$). However, at 2 weeks PC, the frequency of CD4 $^{+}$ central memory T cells (CD4 $^{+}$ Tcm) was not significantly altered among the groups. Nevertheless, the frequency of CD4 $^{+}$ Tcm was still higher in the rBCG30+PII animals as compared to other control groups (Figure 7C). At 2 weeks PC, the level of CD8 $^{+}$ Tcm cells was negligible and inseparable among various groups (Figure 7D).

DPP Therapy Led to Sustained and Systemic Transition of T Cell Memory in rBCG30 Immunized Mice

The effect of DPP based immunotherapeutic strategy on the maintenance of T cell memory was further evaluated at 4 and 8 weeks PC. The splenic T cells from immunized animals were examined for expression of established T cell memory markers CD44 and CD62L. Interestingly, in contrast to 2 weeks PC time point, both CD4 $^{+}$ and CD8 $^{+}$ short lived Tem cells were found to be significantly down-regulated at 4 weeks PC in rBCG30 immunized animals administered PII ($p < 0.001$). The long lived

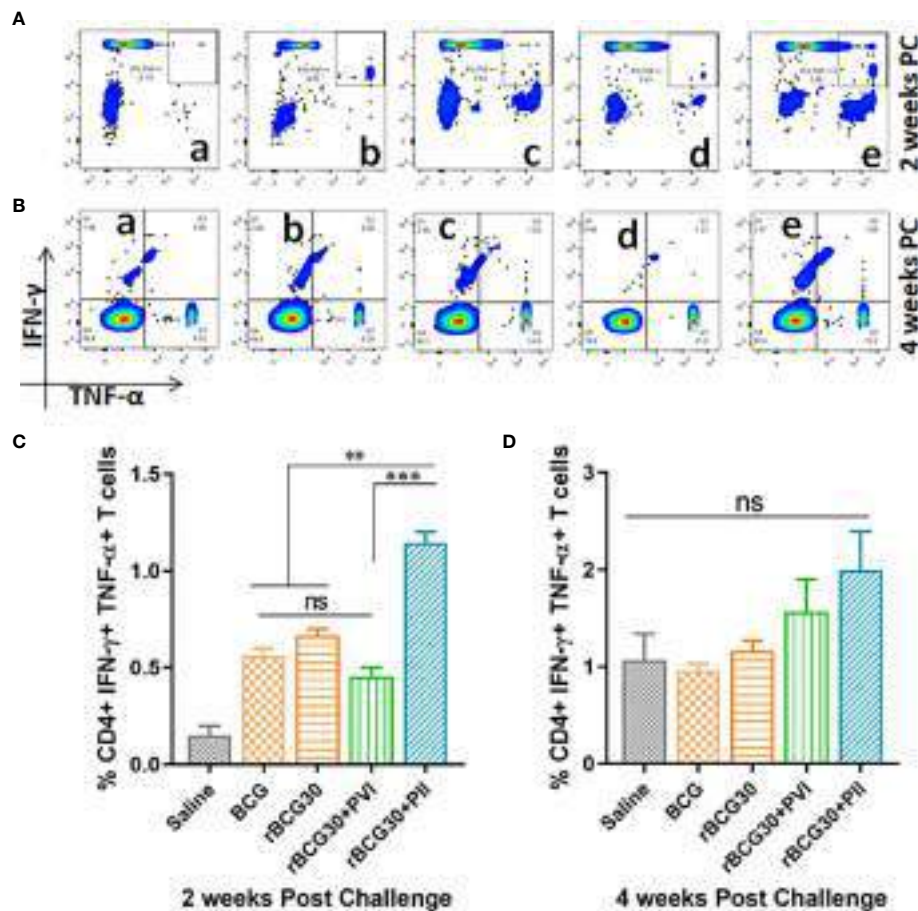


FIGURE 6 | Multifunctional CD4⁺ T cell response post-challenge with *Mtb*. Splenocytes isolated from various immunized and immunotherapy treated animals were profiled employing flow cytometry for simultaneous production of IFN- γ and TNF- α by CD3⁺CD4⁺ T cells at 2 as well as 4 weeks PC. The figure depicts representative FACS plots of CD4⁺ MFTs belonging to (a) Saline, (b) BCG, (c) rBCG30, (d) rBCG30+5,15-DPP (PVI), and (e) rBCG30+5,15-DPP (PII) groups, at (A) 2 and (B) 4 weeks PC, respectively, and corresponding quantitative assessment in the form of bar graphs (C, D). Cells were stimulated with native Ag85B antigen from *Mtb* (5 μ g/ml). The data were analyzed using One-way ANOVA followed by Tukey's multiple comparison test and are shown as the means (\pm SEM) from one of the two independent experiments with similar observations performed in at least three biological replicates, where $p < 0.05$ (*), $p < 0.01$ (**), and $p < 0.001$ (***) were considered significant. ns, non-significant.

CD4⁺ Tcm cells were augmented in the same rBCG30+PII group of animals at 4 weeks PC ($p < 0.05$). The CD8⁺ Tcm cells remained undetectable at this time point (Figures 8A, B). Specifically, at 4 weeks PC, the frequency (cumulative) of CD4⁺ Tem cells was reduced to $\approx 40\%$ (Figure 8A) from $\approx 70\%$ at 2 weeks PC (Figure 7A). The level of CD8⁺ Tem cells at 4 weeks PC (Figure 8B) remained closely similar to its level at 2 weeks PC (Figure 10B). Interestingly, the level of CD4⁺ Tcm cells was increased in the rBCG30+PII group, as compared to either rBCG30 ($p < 0.05$) or rBCG30+PVI ($p < 0.01$) group (Figure 8A).

The decreasing trend of effector memory and augmentation of central memory T cells in the rBCG30+PII group was found to continue until 8 weeks PC with a significant drop in the cumulative level of short lived CD4⁺ Tem cells (from $\approx 44\%$ to $\approx 29\%$) (Figure 8). Conversely, the level of CD4⁺ Tcm cells in the rBCG30+PII group remained high even at week 8 PC, as

compared with either rBCG30 ($p < 0.05$) or BCG ($p < 0.01$) immunized groups (Figure 8C). Notably, the expansion of previously undetected CD8⁺ Tcm cells was spotted at week 8 PC. The CD8⁺ Tcm cells were induced significantly in rBCG30-immunized animals that received DPP therapy (PII) ($p < 0.001$; Figure 8D). To our understanding, the significant induction of CD8⁺ Tcm cells along with CD4⁺ Tcm cells during the late phase of infection embodies the final combined push to resist the pathogen's attempt to acquire dominance during the late phase of infection. Moreover, the failure of BCG is correlated with the predominant expansion of effector memory and weak (or no) central memory T cells. We observed predominance of Tem cells and few central memory cells early after infection. Nevertheless, in contrast to classical BCG or rBCG30 (control groups) based immunization, the level of both CD4⁺ and CD8⁺ Tcm cells at the later time point (week 8 PC) was high in the animals that received immunotherapy following aerosol *Mtb*

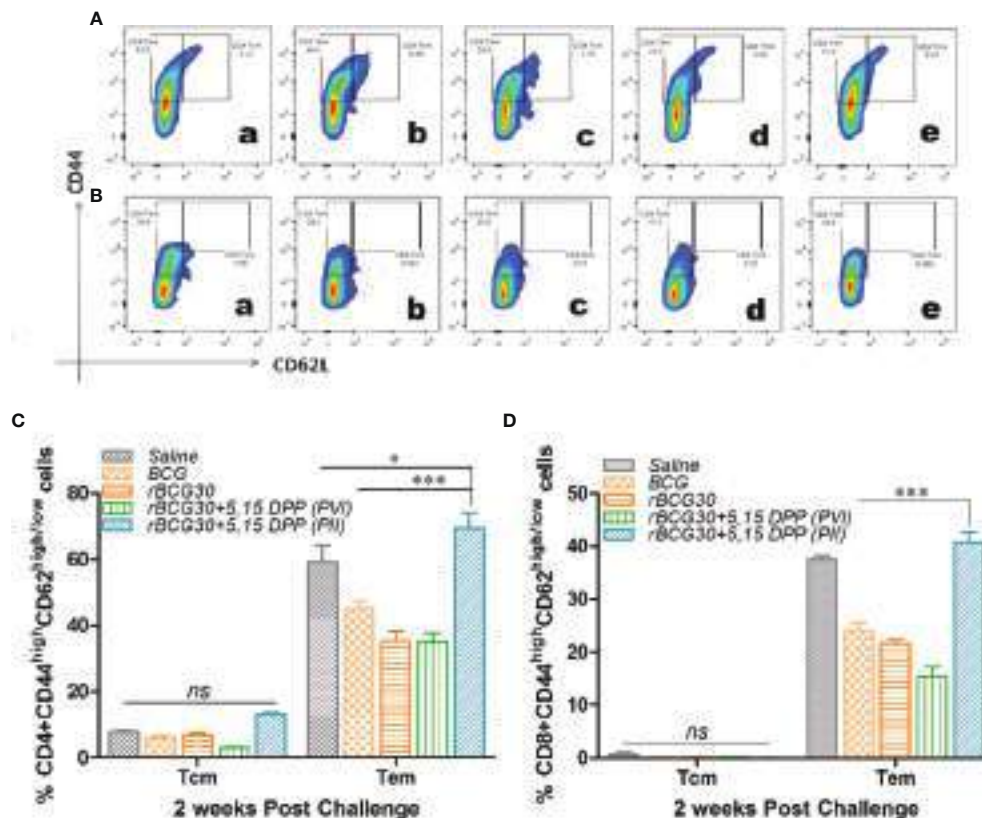


FIGURE 7 | Memory T cell response at week 2 post-challenge. Antigen-specific CD4+ and CD8+ T central and effector memory response was assessed in the splenocytes isolated from various groups at 2 weeks PC. Shown in the figure are representative FACS plots depicting cumulative frequencies of **(A)** CD4+ and **(B)** CD8+ memory T cells from (a) Saline, (b) BCG, (c) rBCG30, (d) rBCG30+5,15-DPP (PVI), and (e) rBCG30+5,15-DPP (PII) groups, respectively. Bar graphs in the figure are depicting comparative magnitude (in percent) of effector memory (CD44^{high}CD62L^{low}) (Tem) and central memory (CD44^{high}CD62L^{high}) (Tcm) among **(C)** CD4+ and **(D)** CD8+ T cells. The data were analyzed by employing Two-way ANOVA followed by Bonferroni's multiple comparison test and are shown as means (\pm SEM) from one of the two independent experiments with similar observations performed in at least three biological replicates, where $p < 0.05$ (*), $p < 0.01$ (**), and $p < 0.001$ (***) were considered significant. ns, non-significant.

infection (PII) that presumably helped prevent the establishment of chronic disease (**Figures 8C, D**).

DPP Therapy Following *Mtb* Challenge Led to the Preferential Proliferation of Th17 Cells Over Immunosuppressive Tregs

To further establish the efficacy of DPP based immunomodulatory strategy targeting the immunosuppressive IL-10/STAT3 signaling axis; the comparative expression of CD4+ Th17 and Treg cells was assessed. The role of Th17 cells in providing protection from TB is much debated as they are considered dispensable for protection against *Mtb* (44). Nevertheless, the Th17 subset plays an adjunctive role in enhancing the diminished Th1 environment, consequent to the activity of anti-inflammatory mediators, including IL-10, during chronic *Mtb* infection (24). Immunosuppressive FoxP3+ T regulatory cells (Tregs) are known to inhibit effector antimycobacterial T cell responses and cause a delay in the onset of adaptive immunity (51–53). Thus, the magnitude of both Th17 and Treg cells was investigated. An attempt was made to establish the

causal relationship between the two subsets by transforming their relative frequencies as a relative ratio (Th17:Treg) (**Figure 9**). While Th17 cells are known to back up deficient Th1 responses (24), Tregs are supposed to brake-off the proliferation of both Th1 and Th17 cells during mycobacterial infection (51, 53). We anticipate that the immunotherapeutic strategy directed towards fine-tuning of Th17/Treg counterbalance, predominantly towards Th17, may prove beneficial to achieve optimal protective immunity against TB.

In the present study, we observed improved Th17 cells proliferation over Tregs in the animals vaccinated with rBCG30 and those that received immunotherapy following *Mtb* challenge (PII) (**Figure 9**). At 4 week PC, animals belonging to the rBCG30+PII group displayed a significantly high Th17 to Treg ratio ($p < 0.05$; **Figure 9E**), and the difference observed was even more at week 8 PC ($p < 0.001$; **Figure 9H**). The observed heightened proliferation of IL-17 producing Th17 cells and relatively low frequencies of FoxP3+ Tregs reflect the ability of employed immunotherapeutic regimen to induce pro-inflammatory Th17 lymphocytes, while simultaneously limiting the differentiation of immunosuppressive Tregs.

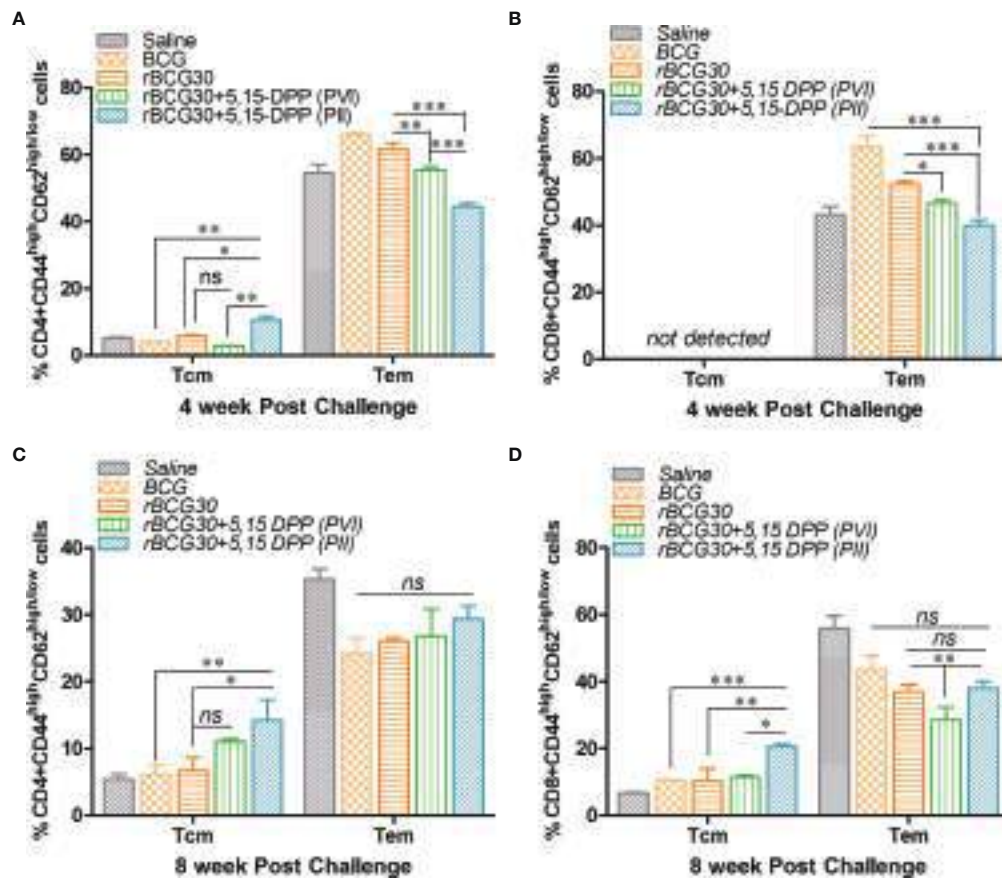


FIGURE 8 | Evaluation of T cells memory response at 4 and 8 weeks post-challenge. Antigen-specific CD4+ and CD8+ T central and effector memory response was assessed in splenocytes isolated from various groups of mice at both 4 and 8 weeks PC. The bar graphs in the figure depict the comparative magnitude (in percent) of T effector (Tem) (CD44^{high}CD62L^{low}) and T central (Tcm) (CD44^{high}CD62L^{high}) cells among (A, C) CD4+, and (B, D) CD8+ memory T cells at 4 (upper panel) as well as 8 (lower panel) weeks PC, respectively. The data were analyzed by employing two-way ANOVA followed by Bonferroni's multiple comparison test and are shown as means (± SEM) from one of the two independent experiments with similar observations performed in at least three biological replicates, where $p < 0.05$ (*), $p < 0.01$ (**), and $p < 0.001$ (***) were considered significant. ns, non-significant.

The Compound DPP Lacks Intrinsic Anti-Mycobacterial Activity Against *Mtb* Strain H37Rv *In Vitro*

In addition to immunomodulatory activity, one can argue that the DPP may possess direct anti-mycobacterial activity as well. To rule out the possibility of intrinsic anti-mycobacterial activity of the immunomodulator DPP, we performed *in vitro* antimycobacterial susceptibility testing employing 96 well microtiter plate based alamar blue assay on avirulent *Mtb* strain H37Ra as well as MGIT assay employing standard virulent *Mtb* strain H37Rv (Figure S3). The antibacterial assay data employing the above specified assays suggested that DPP does not possess intrinsic anti-mycobacterial activity. The DPP exhibited a level of antibacterial activity comparable to that of DMSO in inhibiting *Mtb* H37Ra or Rv outgrowth *in vitro* at the tested concentrations. The *in vitro* data ruled out any intrinsic anti-mycobacterial activity at the tested concentration.

DPP Immunotherapy Following *Mtb* Infection Conferred Superior Protection in rBCG30 Vaccinated Mice

The *in vivo* efficacy of employed host-directed immunotherapy was assessed for its potential to augment the protective capacity of the rBCG30 vaccine against murine TB. The mice were immunized with rBCG30 and administered DPP based immunotherapy, either post vaccination or post-infection (with *Mtb*), were assessed for their ability to combat pulmonary *Mtb* infection. To evaluate the effect of immunotherapy on the control of mycobacterial infection *in vivo*, we examined mycobacterial loads in infected lungs and spleen from the various experimental and control groups of animals at 4 and 8 weeks PC.

Surprisingly, animals treated with DPP following aerosol challenge with *Mtb* (PII) displayed superiorly improved bacillary clearance in the lungs, when compared with either rBCG30 ($p < 0.001$) or rBCG30+PVI groups ($p < 0.01$). In spleen, the bacillary reduction in the rBCG30+PII group was significant in

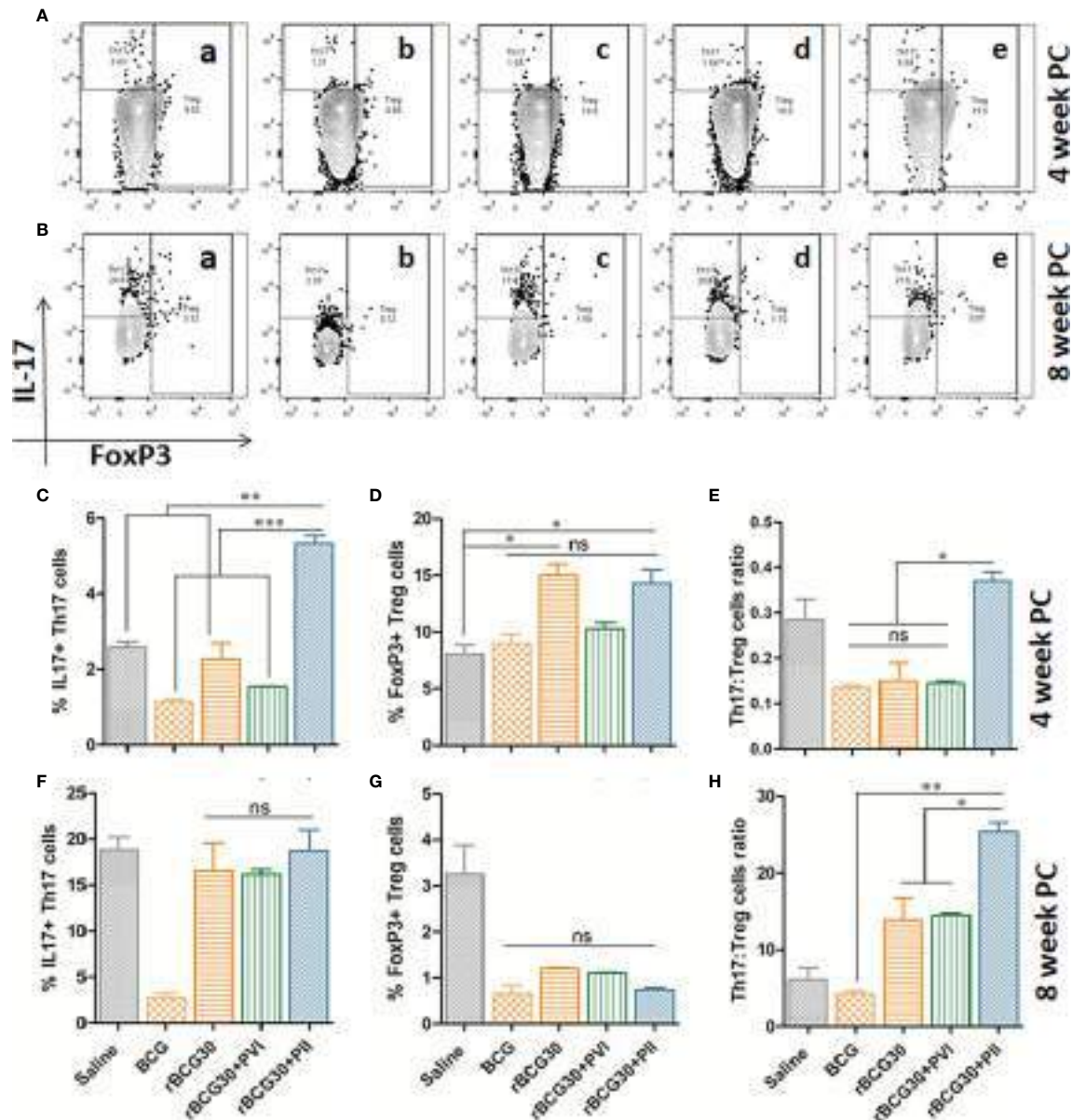


FIGURE 9 | Th17/Treg cells dynamics in response to DPP based immunotherapy. Representative FACS micrographs in upper panel depicting Th17/Treg frequency at (A) 4 and (B) 8 weeks PC with groups labels (a) Saline, (b) BCG, (c) rBCG30, (d) rBCG30+5,15-DPP (PVI), and (e) rBCG30+5,15-DPP (PII), respectively. Bar graphs in the figure are depicting quantitative magnitude (in percent) of Th17 cells at weeks (C) 4 and (F) 8, Treg cells at weeks (D) 4 and (G) 8, and the ratio of Th17 to Tregs at (E) 4 and (H) 8 weeks PC. The level of significance of the data was tested using Two-way ANOVA followed by Tukey's post-test and are shown as means (\pm SEM) from one of the two independent experiments with similar observations performed in at least three biological replicates, where $p < 0.05$ (*), $p < 0.01$ (**), and $p < 0.001$ (***) were considered significant. ns, non-significant.

comparison with the rBCG30 group ($p < 0.05$), but not with the rBCG30+PVI group ($p > 0.05$). Moreover, in comparison with standard BCG control, organ bacillary reductions were prominent in PII treated animals ($p < 0.001$), as well as the PVI treated animals (lungs, $p < 0.001$; spleen, $p < 0.01$), at 4 week PC (Figures 10A, B).

Bacillary burdens in the lungs and spleen of infected animals were further evaluated at week 8 PC. Similar to at 4 weeks PC

time point, the CFU burden at week 8 PC was significantly suppressed in rBCG30-immunized animals that received PII with DPP. The adopted immunotherapeutic scheme was also able to reduce bacterial loads significantly at week 8 PC in rBCG30+PII treated animals, as compared to either classical BCG ($p < 0.001$) or rBCG30 vaccinated controls (lungs, $p < 0.001$; spleen, $p < 0.01$), and/or post-vaccination immunotherapy (PVI) administered animals ($p < 0.01$) (Figure 10C, D).

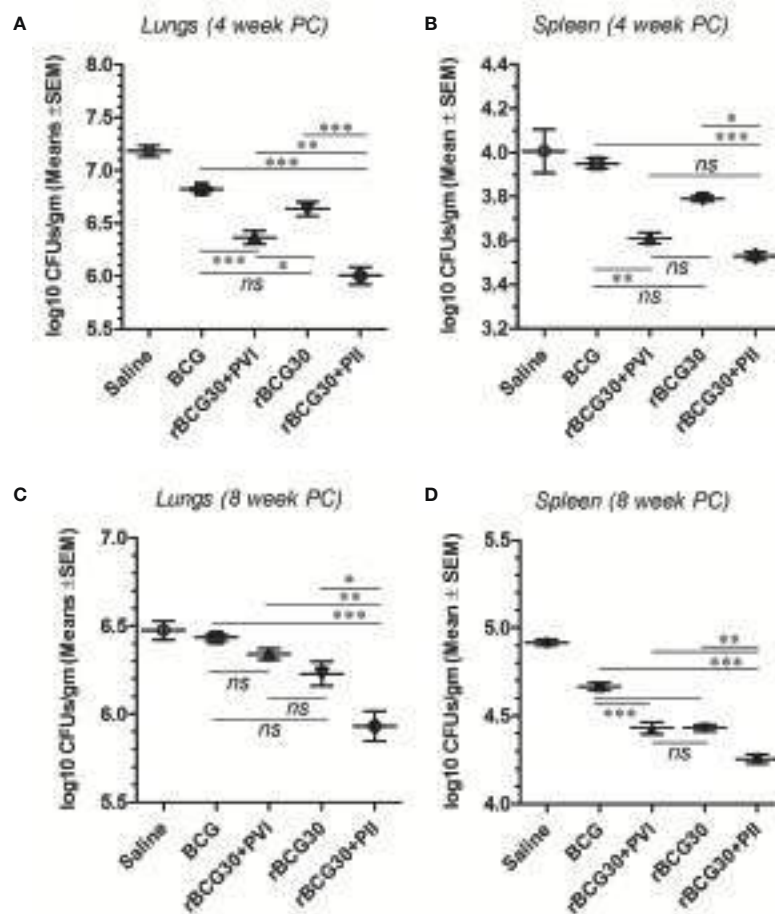


FIGURE 10 | Residual *Mtb* burdens in the lungs and spleen of the infected mice. *Mtb* bacillary load was assessed in rBCG30-immunized and DPP treated (both PVI and PII setups) mice at week 4 and 8 post aerosol *Mtb* challenge. CFU loads in the organ homogenates were enumerated and expressed as log₁₀ CFU/g of tissue. The scatter plots in the figure represent log₁₀ CFU/g ± SD (of at least five biological replicates per group) in lungs and spleen at (A, B) 4; as well as (C, D) 8 weeks post-challenge, respectively. CFU data were analyzed by employing one-way ANOVA followed by Tukey's post-test, where $p < 0.05$ (*), $p < 0.01$ (**), and $p < 0.001$ (***) were considered significant. ns, non-significant.

Comparative mycobacterial loads in the lungs of various immunized and treated groups of animals were also evaluated by AFB staining of the lungs tissue sections. Formalin-fixed lungs tissue sections were subjected to Ziehl–Neelsen staining to assess the comparative tissue bacillary loads in various immunized and treated mice at 4 as well as 8 weeks PC. Mice administered DPP therapy following *Mtb* challenge displayed significantly fewer numbers of AFB+ bacilli in lungs tissue sections stained with Ziehl–Neelsen dye at either 4 or 8 weeks PC, as compared to either saline, BCG, or rBCG30 administered animals (Figure 11). Additionally, rBCG30 immunized and PVI treated animals didn't display improved bacillary clearance at either 4 (Figure 11D) or 8 (Figure 11I) weeks PC time points and the gross tissue mycobacterial loads were equivalent to that present in rBCG30 immunized control animals. Interestingly, while in all other groups bacilli were stained as multibacillary aggregates, in rBCG30+PII administered animals there were usually one or two bacilli at particular foci (paucibacillary), which suggest restrained

Mtb growth in the group. In concordance to CFU enumeration data, lung tissue from PII treated animals displayed the least AFB + burdens, as compared to rBCG30 alone or rBCG30+PVI treated mice at 4 as well as 8 weeks PC (Figure 11).

Overall, there was a maximum reduction in organ CFU burden in the animals vaccinated with rBCG30 and treated PC with DPP (PII). The *in vivo* protective efficacy data of the present study further underscore the protective potential of IL-10/STAT3 targeted DPP therapy (PII) in bolstering host resistance as well as the efficacy of rBCG30 vaccine against *Mtb* challenge in mice.

DISCUSSION

Host directed (immuno) therapeutic (HDT) strategies against *Mtb* have become a research focus in the eradication of TB disease (reviewed elsewhere) (54). Incidentally, most of the tested

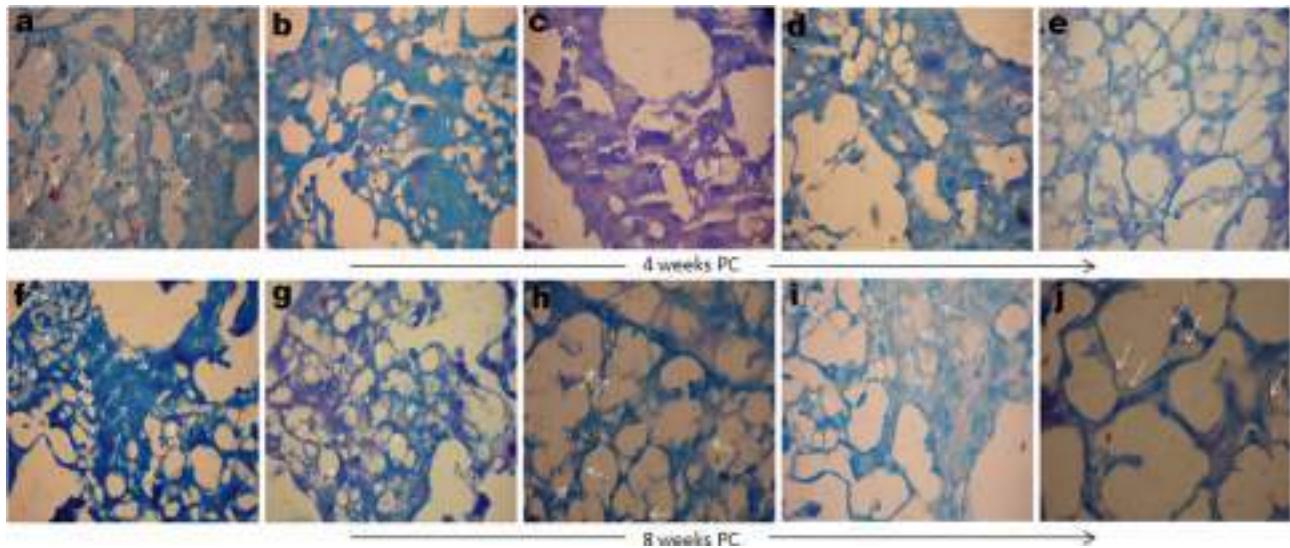


FIGURE 11 | Gross tissue mycobacterial loads in the infected lungs. Representative photomicrographs showing differential *Mtb* bacillary loads in the lungs tissue sections of immunized and DPP immunotherapy administered animals at 4 (upper panel) and 8 (lower panel) weeks PC. Arrows indicating Ziehl–Neelsen dye stained *Mtb* bacilli in various immunized and treated groups (Original magnification—1000x in oil immersion lamp). The various groups were as follows: **(A, F)** Saline **(B, G)** BCG **(C, H)** rBCG30, **(D, I)** rBCG30+PVI, and **(E, J)** rBCG30+PII, respectively.

schemes were proposed either as stand-alone or as an adjunct to standard anti-TB chemotherapy. Despite this, efforts aimed towards using host immune machinery to convalesce the prophylactic immunity conferred by BCG or its engineered recombinant version are relatively limited (23, 53, 55). The IL-10/STAT3 signaling axis has been implicated in generating pro-angiogenic/anti-inflammatory responses in the host (5, 25, 26). Multiple reports have shown that IL-10 persuades STAT3 to skew *Mtb* infected monocytes/macrophages towards pathogen permissive, anti-inflammatory AAM state (3, 6, 31–33). IL-10 has been considered to be a potent pro-mycobacterial cytokine that opts to weaken/disable anti-mycobacterial immune responses (21, 56). Apart from its active role in the direct inhibition of Th1 cell expansion (57), IL-10 delays the migration of DCs from *Mtb* infected lungs to draining lymph nodes (22). Rather, the cytokine IL-10 rejuvenates the chronic/latent *Mtb* infection (20). An optimum vaccination strategy to counter *Mtb* could thrive if it induces a protective pro-inflammatory response in the host while simultaneously restraining pathogen-triggered anti-inflammatory or regulatory pathways. Bearing this in mind, the present study explored DPP based immunotherapy as a host targeted intervention to enhance rBCG30 vaccine mediated immunity against experimental murine TB.

The DPP based therapeutic modulation of host immunity resulted in the significant expansion of M1 monocytes/macrophages (CAMs) along with concomitant reductions in the numbers of M2 monocytes/macrophages (AAMs) in the peritoneum as well as the spleen of the PVI (**Figures S1, S2**) or PII (**Figures 1A–C**) administered animals; except a feeble expansion of classical macrophages in the spleen of the PII

administered group (**Figure 1D**). The differential repertoire of peritoneal and splenic monocytes/macrophages in the PII group can be explained based on two propositions. First, intra-peritoneal administration of DPP therapy might have re-programmed the peritoneal monocytes/macrophages toward a classical state more promptly as compared to their splenic counterparts. Second, because aerogenic *Mtb* takes around two weeks to reach the splenic compartment from the aerosol infected lungs (22), the splenic resident cells in PII administered animals might not have been signaled to alter their steady state phenotype, as nearly 70–80% splenic monocytes/macrophages were found to be in the M2 state until then. By contrast, at 4 weeks PC, both classical monocytes and DCs were significantly expanded in the PVI group, macrophages from the same group of animals did not display any significant difference in numbers. Interestingly, animals belonging to the PII group showed increased numbers of monocytes, macrophages, and DCs with a classical phenotype at this point (**Figure 2**). This suggests that PII with DPP was still better at 4 weeks PC in maintaining a pro-inflammatory environment in macrophages, the primary cells *Mtb* thrives in, as opposed to PVI.

The phenotypic polarization status of the mononuclear phagocytes was further assessed at the week 8 PC time point. As the population of DCs was below the detection level; therefore, we confined our investigation to monocytes and macrophages only. It is noteworthy that the animals from the PVI group failed to maintain a pro-host innate immune response for long and instead displayed predominant differentiation of anti-inflammatory monocytes/macrophages (AAMs) at week 8 PC (**Figure 3**). The weak induction of macrophages bearing classical phenotypes during the late phase of *Mtb* infection can be

correlated with the failure of the PVI strategy to execute bacterial clearance from the host. The maintenance of increased CAMs numbers in the PII group can have a direct correlation with the sustained and controlled expansion of pro-inflammatory milieu that might, in turn, ensued in superior protection of the immunized animals (**Figure 3**). As assessed from the mononuclear phagocytes dynamics, it can be inferred that the post vaccination immunotherapy (PVI), executed before infection with *Mtb*, may be of minimal benefit to the host. It could also be attributed to the fact that avirulent BCG strains are fundamentally different from virulent *Mtb* in terms of pathogenesis (58–60).

For its unhindered intracellular survival, *Mtb* skews invading monocytes/macrophages/DCs toward the M2 state and inhibits the secretion of Th1 cytokines (22, 61). Notably, we found up-regulation of Th1 cytokines (IL-12, IFN- γ) and down-regulation of hallmark Th2 cytokines (IL-10, IL-4) in DPP treated animals following the conclusion of both PVI or PII immunotherapy schedules (**Figure 4**). The level of Th1 cytokine IL-12 was found up-regulated even until 8 weeks PC in the PII group of animals, but not in the PVI group (**Figure 5A**). However, a transient dip in the level of another Th1 cytokine IFN- γ was observed at 4 weeks PC in both PII and PVI group of animals, which was dramatically regained later at week 8 PC (**Figure 5D**). This transient decline in the IFN- γ level was coincident with the significantly augmented level of IL-6 (**Figure 5B**) and IL-17+ Th17 cells expansion (**Figure 9C**) in PII administered animals. The observed cytokine modulation was in concordance with the previous report, where mycobacteria inhibited Th1 response was backed up by IL-23 (and possibly IL-6) mediated Th17 response, followed by restoration of functional Th1 response (24). The levels of innate cytokines IL-1 β and IL-6 were not significantly affected in either PVI or PII treated animals until 2 weeks PC with *Mtb* (**Figure 4**). However, at 4 and 8 week PC, there was a significant increment in the level of IL-6 in PII administered animals (**Figure 5B**). The level of hallmark innate cytokine IL-1 β was not significantly influenced during the course of infection (**Figure 5E**). Interestingly, IL-1 β was least induced in rBCG30+PII administered animals at week 8 PC. The significantly reduced level of IL- β in the rBCG30+PII group may be considered as a correlate of the control of IL- β mediated exuberant inflammation during uncontrolled *Mtb* infection, as also reported previously (18). As expected, the DPP based immunotherapy transiently abrogated the expression of IL-10 until 4 weeks PC (**Figure 5F**), while IL-4 levels were indifferent in either of experimental and control groups at 4 or 8 weeks PC (**Figure 5C**), as opposed to significant inhibition observed at 2 weeks PC (**Figure 4D**). The observed transient reductions in the level of anti-inflammatory cytokines, especially IL-10, are in line with our efforts to fine-tune the anti-inflammatory signaling during the establishment of infection, instead of abrogating it permanently. The transient blockade of IL-10 signaling was desirable as it help avoid the inhibition of efficient immune priming (22). A complete absence of IL-10 increases the likelihood of developing pathological and auto-immune responses in the host. Consistently, these results implicate

IL-10 as a primary culprit that limits vaccine-induced protective anti-mycobacterial immunity by modulating mononuclear phagocytes toward an alternative/anti-inflammatory state of activation. Taken together, the cytokines expression data concord to the previous proposition that the design of host directed therapies against TB must attain an optimal balance between pro- and anti-inflammatory signaling/responses, so as to induce the protective immunity in a manner that inflict minimal collateral tissue pathology (62).

Protection against intracellular pathogens including *Mtb* cannot be achieved without optimum stimulation of the T cell repertoire. In this regard, the multifunctionality of induced T cells upon vaccination or challenge with an infection is an important correlate to assess protective immunity (47). The enhanced proliferation of CD4+ MFTs at 2 weeks PC in the PII group of the animals (**Figure 6**) plausibly accentuated the immune-stimulatory profile and protective potential of the rBCG30 vaccine in immunotherapy (PII) administered animals. The induction of CD4+ MFTs has been considered as an important correlate of a candidate vaccination scheme to impart protective immunity against experimental TB (49, 63).

T cell memory response is an obligatory component of vaccine design to mediate impeccable protection against *Mtb* (64). The DPP immunotherapy mediated strategic manipulation of the IL-10/STAT3 anti-inflammatory axis led to the concerted proliferation of CD4+ and CD8+ effector (CD44^{high}CD62^{low}) and central (CD44^{high}CD62^{high}) memory T cells in the vaccinated host. The memory T cell compartment was initially (2 weeks PC) dominated by both CD4+ and CD8+ effector memory T cells (Tem) in the PII group (**Figure 7**), which later declined and was replaced by CD4+ and CD8+ central memory T cells (Tcm) subsets at week 4 and 8 PC (**Figure 8**). The frequency of Tcm (either CD4 or CD8) was heightened at week 8 PC in PII treated animals, with a significantly high level noted of the CD8+ Tcm population (**Figure 8**). It is well established that antigen exposed 'epigenetically programmed' effector T cells generally result in a subsequent burst of long lived memory T cells (65). Intriguingly, the observed 'systemic transition of Tem population to Tcm', observed in the present study is of particular interest and is in line with current dogma, which argues for differentiation of long lived Tcm cells from the pool of antigen experienced, memory precursor Tem cells, in an ordered, epigenetically regulated 'On-Off-On' process (65–67). The T cell memory response data of the present study concord to this fact, as there was an early preponderance of Tem, and late differentiation of Tcm cells that probably were expanded from among contraction phase survived Tem cells. The greater proportion of effector T cells surviving the contraction phase and entering into a long-lived memory state is indeed an outcome of DPP immunotherapy. This eventually led to unusual induction of T cells with central memory phenotype during the late phase of infection that actually might have restricted the establishment of chronic *Mtb* infection. The observed decline in short lived Tem cell population, specifically at later time points, underscores the relevance of the proposed immunotherapy strategy in restricting surplus effector responses.

Notably, the classical BCG vaccine predominantly induces Tem cells and fails to evoke sufficient protective Tcm cells (68). Thus, the employed immunotherapy may also be explored concomitantly with chemotherapy for its potential to rejuvenate the host immune armory in BCG vaccinated subjects who present with clinical *Mtb* infection.

Fine-tuning between Th17 and Treg cells proliferation is another important aspect in effectively tackling *Mtb* infection (69, 70). In this regard, we measured the relative proliferation of Th17 and Treg cells in various immunized groups and employed the Th17/Treg ratio as an indicator to determine the protective capacity of the proposed immunotherapeutic strategy. We observed increased proliferation of Th17 cells with concomitant downregulation in the frequency of FoxP3+ Treg cells in the immunized animals under the PII scheme (Figure 9). While Th17 cells play an important role in protection against TB (23, 70), Tregs are known to dampen anti-TB immunity and contribute to the progression of the disease (51, 71). The increased Th17:Treg ratio, both at 4 and 8 weeks PC, further affirms the ability of DPP based immunotherapy to selectively inhibit the anti-inflammatory cues following *Mtb* infection in the vaccinated animals (Figure 9).

To assess the protective efficacy of the proposed immunotherapeutic strategy, an *in vivo* protection study was conducted in the mice. The prophylaxis data further affirm that the immunotherapy under the PII scheme resulted in improved protection against aerosol *Mtb* challenge. The immunotherapy (PII) was successful in reducing the bacillary loads in the lungs and spleen of infected mice up to weeks 8 PC, as compared with rBCG30-immunized and untreated control groups (Figure 10). Additionally, the results from histopathological studies (Figure 11) further establish the superior effectiveness of DPP therapy in reducing *Mtb* bacillary loads in the lungs of rBCG30 immunized animals. The mice immunized with rBCG30 and given DPP therapy following aerosol *Mtb* challenge (PII), significantly controlled lungs *Mtb* burdens, as compared to other control and treatment groups (Figure 11). The results corroborate the findings of the CFU counting assay and provide additional evidence of the superior efficacy of DPP mediated post-infection immunotherapy (PII) in rBCG30 immunized and *Mtb* challenged animals. We also evaluated whether DPP possesses any intrinsic anti-mycobacterial activity in an *in vitro* investigation conducted on the H₃₇Ra as well the H₃₇Rv strain of *Mtb* (Figure S3). The results from *in vitro* investigation ruled out any direct anti-mycobacterial activity of DPP and corroborate the central finding of this work that the DPP indeed targets the host and not the bacilli.

The augmented efficacy of the rBCG30 vaccine in the PII administered group of animals establishes the utility of host IL-10/STAT3 depletion (transient) as a viable means to improve TB prophylaxis. It is worth re-mentioning that the successful control of TB relies primarily on the host immune system as the majority of TB infected subjects (~90%) never develop active disease. Emerging evidence suggests that the smart manipulation of the host immune system during vaccination or infection can improve the level of host immunity provided by BCG (53, 55) and BCG based recombinant anti-TB vaccines.

The role of the IL-10/STAT3 signaling axis has been subjected to intense investigations lately and is suggested to have an active role in establishing pro-mycobacterial immune ambiance in the infected host (3, 6, 29, 31–33). SOCS3 and STAT3 are reported as two major regulators during TB infection (5). Mycobacteria possess the ability to impair the SOCS3 feedback loop that limits the IL-6 mediated pro-inflammatory environment. The ensuing IL-10 cytokine induces prolonged activation of STAT3 that in turn promotes an anti-inflammatory environment in the host (5). STAT3 had been associated with numerous mycobacterial survival strategies including blockade of phagolysosome maturation, dampening of reactive oxygen and nitrogen species production, inhibition of autophagy and apoptosis, feeble secretion of Th1 cytokines, reduced presentation of antigens, and eclipsing of co-stimulatory molecules on APCs (5). Few earlier reports have also demonstrated the potential of IL-10 inhibition during vaccination as an effective strategy to enhance anti-mycobacterial immunity (19, 23). Moreover, few recent reports emphasize the role of STAT3 in promoting *Mtb* infection in human subjects (33) and surrogate models (3, 6).

To the best of our knowledge, the present report is the first such attempt to use a small molecule, DPP, that inhibits IL-10 induced STAT3 dimerization and nuclear translocation by binding to either SH2 (Src homology 2) domain (37) or *via* interaction with cytosolic thioredoxin oxidoreductase (TrxR1) (72, 73). Enzyme TrxR1 has recently been described as a direct target of perceived STAT3 inhibitors (including DPP) (72, 73). The majority of available STAT3 inhibitors have been reported to directly bind with cytosolic oxidoreductase TrxR1 *in vitro* in a concentration dependent manner (73). The reduction of oxidized STAT3 by TrxR1 has been proposed to induce dimerization and nuclear translocation of STAT3 (72). It has been speculated that the majority of STAT3 inhibitors work indirectly rather than direct binding to STAT3 (72, 73). In the present study, we made use of the DPP as an immunomodulator/adjuvant, which also targets enzyme TrxR1 to down-modulate STAT3 exerted anti-inflammatory effects. Findings by Busker et al. (72, 73) and Mtwebana et al. (74) indicate that DPP may not directly bind to STAT3 and the observed effects might be STAT3 activation/phosphorylation independent, as also reported by Uehara and colleagues (37) and O'Farrell et al. (25). However, it is unlikely that they operate independently of the transcriptional activity of STAT3, which is extensively established to have a key role in generating an anti-inflammatory environment conducive for infection or cancer outgrowth.

Though this study does not provide direct evidence regarding STAT3 activation/inhibition, the presented evidence from cellular/immunological and protection experiments could be considered a direct correlate of DPP's ability to tame anti-inflammatory effectors, most likely *via* its action on STAT3. We aim to discern the precise role and mechanism of DPP in providing protection against TB in further studies, which will seek to address the critical mechanistic gaps of the present study.

The present study establishes the potential of intercepting host IL-10/STAT3 (and possibly TrxR1) signaling as a crucial

means to bolster innate immune defenses and subsequent adaptive immunity during *Mtb* infection. The proposed strategy is a proof-of-concept that highlights the exploration of IL-10/STAT3/TrxR1 directed immunotherapy as a promising approach to enhance vaccine immunity against TB. Moreover, the chemical nature of the immunomodulator DPP has great advantages in terms of cost-effectiveness, ease of production, stability, and delivery issues, as compared to antibodies or other bio-therapeutics based approaches employed in the earlier studies. The proposed immunotherapeutic approach can be exploited as a viable strategy in improving the protective profile of existing and forthcoming TB vaccines. In addition, it would also be equally interesting to evaluate if the DPP in conjunction with standard anti-TB chemotherapy may serve to enhance the chemotherapeutic index of standard anti-TB drug regimens.

MATERIALS AND METHODS

Reagents

All standard reagents used in the study were purchased from Sigma-Aldrich (St. Louis, MO, USA) unless otherwise noted. The bacterial culture reagents, Middlebrook 7H9 broth; Middlebrook 7H11 agar, and Oleic Acid Albumin Dextrose and Catalase (OADC) supplement were procured from Difco Laboratories (Sparks, MD, USA). Plasticware was purchased from BD Biosciences (San Jose, CA, USA).

Animals

6–8 weeks old, BALB/c mice (n=111) of male sex were used in the study. Animals were acclimatized for a week before commencing the experiments. All animals were kept in a resting state with free access to food and water for 2 months from the day of vaccination, except the post vaccination immunotherapy (PVI) group that was administered DPP daily for one week after vaccination with rBCG30.

Immunization and Immunotherapy Schedule

Mice were immunized subcutaneously with either commercial BCG vaccine manufactured by Serum Institute of India or in-house propagated rBCG30-ARMF-II[®] Tice. Vaccines were equilibrated to deliver $1\text{--}1.5 \times 10^5$ CFUs in 100 μ l of normal saline and administered subcutaneously. As a placebo, normal saline was administered in one group of animals (saline control group). Animals immunized with rBCG30 were divided into two sub-groups. The first group received post vaccination immunotherapy (PVI) with DPP (Sigma-Aldrich) daily for one week commencing at day 1 post vaccination. The second group received post-infection immunotherapy (PII) on alternate days for two weeks starting at day 1 post aerosol *Mtb* challenge. To negate the effect of DMSO used as a solvent and vehicle to deliver DPP, DMSO sham control groups, rBCG30+sham (PVI) and rBCG30+sham (PII), were also included in the study. No specific effect was observed on the DMSO carrier that was used as a solvent to deliver DPP. All the treatment with DPP or vehicle (DMSO) was given intra-peritoneum. The dose used of DPP was

15 mg/kg of body weight as described previously (26), in injection volume of 200 μ l/mice/day.

Mycobacterium Bovis BCG, rBCG30, and *Mycobacterium Tuberculosis* H₃₇Rv Strains

rBCG30-ARMF-II[®] Tice was provided by Professor Marcus A. Horwitz (UCLA) and obtained under the limited, non-commercial use agreement between UCLA (USA) and AMU (India). The Bacille Calmette–Guerin (Russian strain) was obtained commercially (marketed as Tubervac[®] by Serum Institute of India) *Mtb* H₃₇Rv strain was kindly provided by The Director, National JALMA Institute for Leprosy and Other Mycobacterial Diseases (NJIL and OMD), Agra, India. *Mtb* was cultured in Middlebrook 7H9 broth containing 0.2% glycerol and 0.05% Tween-80 supplemented with 10% OADC at 37°C as a shaking culture. rBCG30 was cultured in Middlebrook 7H9 broth containing 0.02% Tween-80 supplemented with 10% OADC at 37°C with continuous shaking. The *Mtb* H₃₇Rv used in the study was passaged in mice on regular basis to ascertain its virulence. The viability was determined by culturing the bacteria on Middlebrook 7H11 medium supplemented with OADC and counting the number of colony forming units (CFUs).

Antigens for Ex Vivo Stimulation of Immune Cells

Purified native Ag85B (5 μ g/ml) was used to stimulate the cell cultures derived from various experimental and controls groups. Purified native Ag85B (NR-14857) was procured through BEI Resources (Manassas, VA, USA) under a TB research material procurement contract between NIAID (USA) and AMU (India). As per the manufacturer, the protein was purified from the culture filtrate proteins of *Mycobacterium tuberculosis* (strain H₃₇Rv).

Antibody Based Reagents and Assay Kits

The following fluorochrome-labeled anti-mouse antibodies were procured from e-Biosciences and BD Biosciences: anti CD3 (145-2C11), anti CD4 (GK 1.5), anti CD8 (53-6.7), anti CD44 (IM7), anti CD62L (MEL-14), anti CD11b (M1/70), anti F4/80 (T45-2342), anti Ly6C (AL-21), anti TNF- α (MP6-XT22), and anti IFN- γ (XMG1.2). Mouse Th17/Treg phenotyping kit (Cat. No. 560767) and IL-1 β , IL-4, IL-6, IFN- γ , IL-12, IL-10 BD OptEIA cytokine ELISA kits were procured from BD Biosciences (USA).

Ethics Statement

All animal experiments were approved by the Institutional Animal Ethics Committees (IAEC) of the ICMR-National JALMA Institute for Leprosy and Other Mycobacterial Diseases, Agra, India. All animal experiments were performed according to the National Regulatory Guidelines issued by CPCSEA.

Establishment of Infection and Determination of Tissue Mycobacterial Loads

Two months post vaccination; all animals were challenged with virulent *Mtb* (H₃₇Rv) through aerosol route. A bacterial suspension corresponding to 5×10^7 bacteria/ml in 10 ml

normal saline was added to the nebulizer unit of the Aerosol Inhalation Exposure System (Glas-Col, USA). To determine the number of viable bacilli delivered to and surviving in mice lungs, 3 animals were euthanized within 16 h post-challenge (Day 1), and the entire lung homogenates were plated onto 7H11 agar plates to approximate the average implanted CFUs in the lungs of infected animals. On average, ≈ 110 viable bacilli were deposited into the lungs of each mouse. All animal challenge/infection studies were performed in the BSL-3 level containment facility at ICMR-National JALMA Institute for Leprosy and Other Mycobacterial Diseases, Agra, India. Standard biosecurity and institutional safety procedures have been adhered to as per institutional SOPs and guidelines.

To evaluate the protective efficacy of the employed immunotherapeutic strategy, we determined the bacterial load in the lungs and spleen of experimental animals at 4 and 8 weeks post *Mtb* aerosol challenge. At stipulated time intervals, a minimum of 4 animals from each group were euthanized; their spleen and lungs were removed aseptically and homogenized in 7H9 media. Four different dilutions of prepared homogenate were plated onto 7H11 agar plates supplemented with OADC. Thiophene carboxylic acid hydrazide (TCH) at a concentration of 2 mg/ml was added to inhibit the growth of BCG or rBCG30 in immunized groups. All the plates were incubated for 3–4 weeks at 37°C in a CO₂ incubator with a constant supply of 5% CO₂. After incubation, colonies were counted to calculate the bacterial load. Bacterial loads were interpreted and expressed as mean log₁₀ CFU/g in the lungs and spleen of infected animals.

Isolation of Lymphocytes, Mononuclear Phagocytes, and Peritoneal Exudates Cells

Mice from various experimental groups ($n = 3-5$) were euthanized at specific time points, i.e. 2 weeks (next day after the conclusion of post-infection immunotherapy (PII), 4 weeks, and 8 weeks post-challenge (PC) to assess immunological parameters in the immunized animals. Single cell suspensions of the spleens were prepared according to previously reported procedures (75). Briefly, spleens from animals representing various groups were macerated using frosted glass slides and passed through a 70 μ m cell strainer to obtain single cell suspensions. The cell suspension was treated with ACK lysis buffer to lyse erythrocytes. Next, the cells were washed with Hanks Balanced Salt Solution (HBSS) three times and re-suspended in a complete RPMI 1640 medium. Peritoneal macrophages or Peritoneal Exudates Cells (PECs) were also isolated from PVI or PII treated animals the day after the completion of DPP therapy to assess their activation state specific phenotype. Isolated lymphocytes and mononuclear phagocytes from the spleen or peritoneum were characterized by assessing the presence of specific cell surface markers employing flow cytometry.

Cytokine Assay: Assessment of Antigen Induced Cytokine Profile

Both pro (IFN- γ , IL-12, IL-1 β , IL-6) and anti (IL-4, IL-10) inflammatory cytokines induced in *ex vivo* re-stimulated

splenocyte culture supernatants (from various experimental and control groups) were estimated using OptEIA sandwich ELISA kits (BD Biosciences). Briefly, 100 μ l of the purified capture antibodies were adsorbed overnight on polystyrene micro-titer plates (Maxisorp, Thermo Scientific) at 4°C in the kit recommended coating buffer. Plates were washed five times with PBST and blocked with 1% BSA. After washing, 100 μ l of the supernatant (isolated from cultured splenocytes after 24 h) was dispensed in each well. After incubation for the time stipulated, the plates were thoroughly washed and incubated with respective biotinylated anti-mouse detection antibody. Afterward, the plates were washed three times with PBST. Subsequently, 100 μ l of streptavidin-HRP conjugate was added to each well, and the plate was incubated for 30 min at room temperature (RT). The plates were again washed three times with PBST and finally a colored complex was developed with tetra methyl benzidine (TMB). The absorbance was read at 450 nm with a micro-titer ELISA plate reader (Bio-Rad).

Flow Cytometric Phenotyping of T Lymphocytes and Mononuclear Phagocytes

Ex vivo re-stimulated splenic lymphocytes/phagocytes or PECs (unstimulated) were harvested and stained for flow cytometric analysis following a protocol provided by BD Biosciences. Briefly, 1×10^6 splenocytes were washed twice with FACS staining buffer (PBS with 1% BSA and 0.1% sodium azide). Cells were incubated with Fc block (2.4G2) or with appropriate fluorochrome tagged monoclonal antibodies against CD3, CD4, CD8, CD44, CD62L, CD11b, F4/80, and Ly6C for 30 minutes at 4°C. After washing, cells were fixed with 4.0% paraformaldehyde (PFA). The flow cytometry data were acquired using FACS Aria-II platform with FACS Diva software (BD Biosciences) and a minimum of 10 000 events were recorded for each sample. Data were further analyzed with FlowJo software (Treestar Inc., USA). The cells of a definite phenotype [CD4⁺CD44^{high}CD62L^{low/high} (CD4 Tmem), CD8⁺CD44^{high}CD62L^{low/high} (CD8 Tmem), CD11b⁺F4/80⁺SSC^{low}Ly6C^{low/high} (Macrophages), CD11b⁺F4/80⁺SSS^{low}Ly6C^{low/high} (Monocytes), CD11b⁺F4/80⁺SSS^{low}Ly6C^{low/high} (DCs)] were deduced as percentage of the gated cell population, as determined by flow cytometry.

Intracellular Cytokine Staining for Multifunctional CD4+ and Th17/Treg Cells Detection

Splenocytes isolated and stimulated *ex vivo* for 24 h from various immunized mice were collected, washed with PBS, and stained for surface markers *viz.* CD3, CD4, and CD8 followed by fixation using Cytofix buffer (BD Biosciences). Thereafter, cells were permeabilized with Perm/Wash buffer (BD Biosciences), followed by intracellular staining to probe IFN- γ and TNF- α in the examined cells. GolgiStop solution (BD Biosciences) was added for the last 4 h of incubation before collecting the cells for staining and was removed subsequently through washing. Stained cells were subsequently acquired. The relative proportions of CD4⁺ Th17 and Treg cells populations were

determined with a Th17/Treg phenotyping kit following the manufacturer-supplied protocol (BD). The stained cells were subsequently acquired on the FACS Aria-II platform with FACS Diva software (BD) and later analyzed by FlowJo software. For intracellular staining, a minimum of 50,000 events were recorded.

Acid Fast Staining of Lungs Tissues

The experimental animals were sacrificed and their lungs were perfused fixed in 10% buffered formalin. Later, tissue blocks (of 3 mm × 5 mm dimensions) were processed for paraffin embedding, and subsequently, 10-mm thick sections were cut with a rotary microtome. Sections were subjected to Ziehl-Neelsen staining to identify and estimate the relative load of the acid-fast bacilli (AFB) in the stained tissue sections. Stained representative tissue sections were observed under a light microscope (Nikon). Observations were recorded and interpreted independently by an experienced histopathologist. Photomicrographs were taken from granulomatous regions of samples showing AFB+ staining.

Microplate Alamar Blue Assay to Evaluate the Anti-Mycobacterial Activity of DPP

The direct anti-mycobacterial activity of DPP was evaluated following a previously published protocol with slight modifications (76). The avirulent H37Ra strain of *Mtb* (as a surrogate to check anti-*Mtb* activity in alamar blue assay) was grown in 100 ml of Middlebrook 7H9 broth (Difco) supplemented with 0.2% glycerol (Sigma), 10% OADC (Difco), and 0.05% Tween 80 (Sigma) on continuous shaking (180 rpm) at 37°C until the culture reached an optical density of 0.5 to 0.6 at 600 nm. The obtained bacterial suspension was washed with normal saline and suspended in 7H9 medium with OD adjusted to 0.01. The culture was then used for inoculation in 96 well microplate alamar blue assay in 100 µl 7H9 media (in duplicate). The compound DPP (dissolved in DMSO) was dispensed in each well at a two-fold diluting concentration (250 µg/ml to 1.95 µg/ml). The concentration of DMSO was maintained in all the wells and DMSO alone control was also included. Outer perimeter wells of the plate were filled with sterile water to prevent dehydration in experimental wells and the plate was sealed with parafilm. Medium alone was taken as a negative control and bacteria only as a positive control. Plates were incubated at 37°C for 5 days. On the fifth day post incubation in dark at 37°C, 50 µl of 0.3% alamar blue solution was added to all the wells, and the plate was further incubated for another 6 hrs. Post incubation, the absorbance of the colored complex was recorded at 570 nm (in absorbance mode) using a microplate spectrophotometric reader with wavelength correction at 600 nm (Eon, BioTek Instruments).

Evaluation of the Direct Anti-Mtb Activity of DPP Using BACTEC MGIT960 System

We also determined the direct anti-*Mtb* activity of DPP *in vitro* using BACTEC mycobacterial growth indicator tubes (MGIT)

960 system (Cat. No. 445870-BD Biosciences). The MGIT960 system utilizes fluorescence readout as an indicator of mycobacterial growth. The MGIT tubes contained a fluorescent compound embedded in silicone on the bottom of the tubes. The fluorescent compound was sensitive to the presence of oxygen dissolved in the broth. Initially, the large amount of dissolved oxygen quenches emissions from the compound and little fluorescence can be detected. As the mycobacterial cells grow, they utilize dissolved oxygen and thus allow the dequenching of the fluorescent probe. The machine had a provision to automatically indicate when there is sufficient *Mtb* growth or at 42 days (cut-off if no growth). Upon unloading the tube from the machine, a trail gets generated for each unloaded tube that contains arbitrary fluorescent units. This enabled us to better understand the approximate growth of the culture.

The MGIT960 grown culture of *Mtb* H37Rv (approx. 10^5 - 10^6 CFU/ml) was used to perform the experiment. The freshly grown culture was diluted 100 times (GC100) and 100 µl of the diluted culture was added to 7 ml BBL MGIT tubes (Cat. No. 245122-BD Biosciences) supplemented with OADC, but no antibiotics were added. The DPP was added (in duplicate) at 50 µM concentration (100 µl volume) in tubes inoculated with GC100 and allow to grow in the system. In a negative control tube, 100 µl DMSO alone was added. Positive control (only bacteria) tubes were also included. The graph of fluorescence readout (arbitrary units) was plotted for experimental and control tubes.

Statistical Analysis of Data

The data of various immunological studies (pertaining to various immunized and immunotherapy treated groups) was compared by employing either two-way or one-way ANOVA (as appropriate) followed by Bonferroni's or Tukey's multiple comparison post-test (as appropriate) using Graph Pad Prism software version 5.03. Data presented in various immunological assays are representative of at least 3 animals from each group and 2 similar experiments. The *p* values, <0.05(*), <0.01(**), <0.001(***) were considered as significant for analysis and interpretation of experimental data.

DATA AVAILABILITY STATEMENT

The original contributions presented in the study are included in the article/**Supplementary Material**. Further inquiries can be directed to the corresponding author.

ETHICS STATEMENT

The animal study was reviewed and approved by Institutional Animal Ethics Committees (IAEC) of ICMR-National JALMA Institute for Leprosy and Other Mycobacterial Diseases, Agra, India. All animal experiments were performed according to the National Regulatory Guidelines issued by CPCSEA.

AUTHOR CONTRIBUTIONS

FA conceived the idea of the manuscript, carried out all major experiments, analyse and interpret most of the data and wrote the first draft of the manuscript. MO provided overall supervision of the study, analyzed the data, edited the manuscript critically, and acquired/provided funding for the completion of the study. PG and UG helped executed animal challenge studies and contributed reagents and resources. MSU, NK, and FJ helped carry out experimental investigations. SZ provided software resources and data analysis services. All authors contributed to the article and approved the submitted version.

FUNDING

FA acknowledges University Grants Commission (UGC), India for granting him a Basic Science Research (BSR) fellowship for doctoral studies. No specific funding was acquired or used for conducting the study except fellowship/salary support to FA. F. No.25-1/2014-15(BSR)/7-6/2007(BSR), dated: 13 March & 24 June, 2015, against fellowship support to FA from UGC, India.

REFERENCES

- O'Garra A, Redford PS, McNab FW, Bloom CI, Wilkinson RJ, Berry MPR. The Immune Response in Tuberculosis. *Annu Rev Immunol* (2013) 31 (1):475–527. doi: 10.1146/annurev-immunol-032712-095939
- Orme IM, Robinson RT, Cooper AM. The Balance Between Protective and Pathogenic Immune Responses in the TB-Infected Lung. *Nat Immunol* (2015) 16(1):57–63. doi: 10.1038/ni.3048
- Queval CJ, Song O, Deboosère N, Delorme V, Debie A, Iantomasi R, et al. STAT3 Represses Nitric Oxide Synthesis in Human Macrophages Upon Mycobacterium Tuberculosis Infection. *Sci Rep* (2016) 6(1):29297. doi: 10.1038/srep29297
- Oehlers SH, Cronan MR, Scott NR, Thomas MI, Okuda KS, Walton EM, et al. Interception of Host Angiogenic Signalling Limits Mycobacterial Growth. *Nature* (2015) 517(7536):612–5. doi: 10.1038/nature13967
- Rottenberg ME, Carow B. SOCS3 and STAT3, Major Controllers of the Outcome of Infection With Mycobacterium Tuberculosis. *Semin Immunol* (2014) 26(6):518–32. doi: 10.1016/j.smim.2014.10.004
- Lastrucci C, Bénard A, Balboa L, Pingris K, Souriant S, Poincloux R, et al. Tuberculosis Is Associated With Expansion of a Motile, Permissive and Immunomodulatory CD16+ Monocyte Population via the IL-10/STAT3 Axis. *Cell Res* (2015) 25(12):1333–51. doi: 10.1038/cr.2015.123
- Pahari S, Kaur G, Negi S, Aqdas M, Das DK, Bashir H, et al. Reinforcing the Functionality of Mononuclear Phagocyte System to Control Tuberculosis. *Front Immunol* (2018) 9:193/full(FEB). doi: 10.3389/fimmu.2018.00193/full
- Khan N, Downey J, Sanz J, Kaufmann E, Blankenhau B, Pacis A, et al. M. Tuberculosis Reprograms Hematopoietic Stem Cells to Limit Myelopoiesis and Impair Trained Immunity. *Cell* (2020) 183(3):752–70.e22. doi: 10.1016/j.cell.2020.09.062
- Kaufmann E, Sanz J, Dunn JL, Khan N, Mendonça LE, Pacis A, et al. BCG Educates Hematopoietic Stem Cells to Generate Protective Innate Immunity Against Tuberculosis. *Cell* (2018) 172(1–2):176–90.e19. doi: 10.1016/j.cell.2017.12.031
- Verrall AJ, Schneider M, Alisjahbana B, Apriani L, van Laarhoven A, Koeken VACM, et al. Early Clearance of Mycobacterium Tuberculosis Is Associated With Increased Innate Immune Responses. *J Infect Dis* (2020) 221(8):1342–50. doi: 10.1093/infdis/jiz147
- Joosten SA, Van Meijgaarden KE, Arend SM, Prins C, Oftung F, Korsvold GE, et al. Mycobacterial Growth Inhibition Is Associated With Trained Innate Immunity. *J Clin Invest* (2018) 128(5):1837–51. doi: 10.1172/JCI97508
- Lerm M, Netea MG. Trained Immunity: A New Avenue for Tuberculosis Vaccine Development. *J Intern Med* (2016) 279(4):337–46. doi: 10.1111/joim.12449
- Chackerian AA, Alt JM, Perera TV, Dascher CC, Behar SM. Dissemination of Mycobacterium Tuberculosis is Influenced by Host Factors and Precedes the Initiation of T-Cell Immunity. *Infect Immun* (2002) 70(8):4501–9. doi: 10.1128/IAI.70.8.4501-4509.2002
- Lugo-Villarino G, Neyrolles O. Manipulation of the Mononuclear Phagocyte System by Mycobacterium Tuberculosis. *Cold Spring Harb Perspect Med* (2014) 4(11):a018549–a018549. doi: 10.1101/cshperspect.a018549
- Singh V, Jamwal S, Jain R, Verma P, Gokhale R, Rao KVS. Mycobacterium Tuberculosis-Driven Targeted Recalibration of Macrophage Lipid Homeostasis Promotes the Foamy Phenotype. *Cell Host Microbe* (2012) 12 (5):669–81. doi: 10.1016/j.chom.2012.09.012
- Mahajan S, Dkhar HK, Chandra V, Dave S, Nanduri R, Janmeja AK, et al. Mycobacterium Tuberculosis Modulates Macrophage Lipid-Sensing Nuclear Receptors Pparγ and TR4 for Survival. *J Immunol* (2012) 188(11):5593–603. doi: 10.4049/jimmunol.1103038
- Girgis NM, Gundra UM, Ward LN, Cabrera M, Frevert U, Loke P. Ly6Chigh Monocytes Become Alternatively Activated Macrophages in Schistosomes Granulomas With Help From CD4+ Cells. Mountford AP, Editor. *PLoS Pathog* (2014) 10(6):e1004080. doi: 10.1371/journal.ppat.1004080
- Mishra BB, Rathinam VAK, Martens GW, Martinot AJ, Kornfeld H, Fitzgerald KA, et al. Nitric Oxide Controls the Immunopathology of Tuberculosis by Inhibiting NLRP3 Inflammasome-Dependent Processing of IL-1β. *Nat Immunol* (2012) 14(1):52–60. doi: 10.1038/ni.2474
- Silva RA, Pais TF, Appelberg R. Blocking the Receptor for IL-10 Improves Antimycobacterial Chemotherapy and Vaccination. *J Immunol* (2001) 167 (3):1535–41. doi: 10.4049/jimmunol.167.3.1535
- Turner J, Gonzalez-Juarrero M, Ellis DL, Basaraba RJ, Kipnis A, Orme IM, et al. In Vivo IL-10 Production Reactivates Chronic Pulmonary Tuberculosis in C57BL/6 Mice. *J Immunol* (2002) 169(11):6343–51. doi: 10.4049/jimmunol.169.11.6343
- Beamer GL, Flaherty DK, Assogba BD, Stromberg P, Gonzalez-Juarrero M, de Waal Malefyt R, et al. Interleukin-10 Promotes Mycobacterium Tuberculosis Disease Progression in CBA/J Mice. *J Immunol* (2008) 181(8):5545–50. doi: 10.4049/jimmunol.181.8.5545
- Redford PS, Murray PJ, O'Garra A. The Role of IL-10 in Immune Regulation During M. Tuberculosis Infection. *Mucosal Immunol* (2011) 4(3):261–70. doi: 10.1038/mi.2011.7

ACKNOWLEDGMENTS

Authors are thankful to the Coordinator, Interdisciplinary Biotechnology Unit, AMU (India) for providing facilities to complete this study and the Director, ICMR-National JALMA Institute for Leprosy and OMD, Agra, India; for allowing the use of the institute's Animal BSL-3 facility and also for providing mycobacterial strains. The authors are thankful to the histopathology core of the ICMR-National Institute of Pathology, New Delhi, India for their help to conduct histopathological analysis. The authors are grateful to Professor Marcus A. Horwitz (UCLA) for providing the rBCG30-ARMF-II[®] Tice vaccine, and pre-publication commentary on the manuscript. The following reagent was obtained through BEI Resources, NIAID, NIH: Ag85B (Gene Rv1886c), Purified Native Protein from *Mycobacterium tuberculosis*, Strain H37Rv, NR-14857.

SUPPLEMENTARY MATERIAL

The Supplementary Material for this article can be found online at: <https://www.frontiersin.org/articles/10.3389/fimmu.2021.706727/full#supplementary-material>

23. Pitt JM, Stavropoulos E, Redford PS, Beebe AM, Bancroft GJ, Young DB, et al. Blockade of IL-10 Signaling During Bacillus Calmette-Guerin Vaccination Enhances and Sustains Th1, Th17, and Innate Lymphoid IFN- and IL-17 Responses and Increases Protection to Mycobacterium Tuberculosis Infection. *J Immunol* (2012) 189(8):4079–87. doi: 10.4049/jimmunol.1201061
24. Gopal R, Lin Y, Obermajer N, Slight S, Nuthalapati N, Ahmed M, et al. IL-23-Dependent IL-17 Drives Th1-Cell Responses Following Mycobacterium Bovis BCG Vaccination. *Eur J Immunol* (2012) 42(2):364–73. doi: 10.1002/eji.201141569
25. O'Farrell A-M, Liu Y, Moore KW, Mui AL-F. IL-10 Inhibits Macrophage Activation and Proliferation by Distinct Signaling Mechanisms: Evidence for Stat3-Dependent and -Independent Pathways. *EMBO J* (1998) 17(4):1006–18. doi: 10.1093/emboj/17.4.1006
26. Nakamura R, Sene A, Santeford A, Gdoura A, Kubota S, Zapata N, et al. IL10-Driven STAT3 Signalling in Senescent Macrophages Promotes Pathological Eye Angiogenesis. *Nat Commun* (2015) 6(1):7847. doi: 10.1038/ncomms8847
27. Siersbaek R, Scabia V, Nagarajan S, Chernukhin I, Papachristou EK, Broome R, et al. IL6/STAT3 Signaling Hijacks Estrogen Receptor α Enhancers to Drive Breast Cancer Metastasis. *Cancer Cell* (2020) 38(3):412–23.e9. doi: 10.1016/j.ccell.2020.06.007
28. Gharibi T, Babaloo Z, Hosseini A, Abdollahpour-alitappeh M, Hashemi V, Marofi F, et al. Targeting STAT3 in Cancer and Autoimmune Diseases. *Eur J Pharmacol* (2020) 878:173107. doi: 10.1016/j.ejphar.2020.173107
29. Genoula M, Marin Franco JL, Dupont M, Kviatkovsky D, Milillo A, Schierloh P, et al. Formation of Foamy Macrophages by Tuberculous Pleural Effusions Is Triggered by the Interleukin-10/Signal Transducer and Activator of Transcription 3 Axis Through ACAT Upregulation. *Front Immunol* (2018) 9:459/full(MAR). doi: 10.3389/fimmu.2018.00459/full
30. Balboa L, Romero MM, Basile JJ, Sabio y Garcia CA, Schierloh P, Yokobori N, et al. Paradoxical Role of CD16+CCR2+CCR5+ Monocytes in Tuberculosis: Efficient APC in Pleural Effusion But Also Mark Disease Severity in Blood. *J Leukoc Biol* (2011) 90(1):69–75. doi: 10.1189/jlb.1010577
31. Upadhyay R, Sanchez-Hidalgo A, Wilusz CJ, Lenaerts AJ, Arab J, Yeh J, et al. Host Directed Therapy for Chronic Tuberculosis via Intrapulmonary Delivery of Aerosolized Peptide Inhibitors Targeting the IL-10-STAT3 Pathway. *Sci Rep* (2018) 8(1):16610. doi: 10.1038/s41598-018-35023-0
32. Sogi KM, Lien KA, Johnson JR, Krogan NJ, Stanley SA. The Tyrosine Kinase Inhibitor Gefitinib Restricts Mycobacterium Tuberculosis Growth Through Increased Lysosomal Biogenesis and Modulation of Cytokine Signaling. *ACS Infect Dis* (2017) 3(8):564–74. doi: 10.1021/acsinfecdis.7b00046
33. Harling K, Adankwah E, Güler A, Afum-Adjei Awuah A, Adu-Amoah L, Mayatepek E, et al. Constitutive STAT3 Phosphorylation and IL-6/IL-10 Co-Expression are Associated With Impaired T-Cell Function in Tuberculosis Patients. *Cell Mol Immunol* (2018) 16(3):275–87. doi: 10.1038/cmi.2018.5
34. Horwitz MA, TM V. *United States Patent Horwitz et al.* US: US Patent Office; US 8,932,846 B2 (2015). Available at: <https://patentimages.storage.googleapis.com/64/dc/f4/6095bb2eb4d99a/US8932846.pdf>.
35. Hoft DF, Blazevic A, Abate G, Hanekom WA, Kaplan G, Soler JH, et al. A New Recombinant Bacille Calmette-Guérin Vaccine Safely Induces Significantly Enhanced Tuberculosis-Specific Immunity in Human Volunteers. *J Infect Dis* (2008) 198:1–11. doi: 10.1086/592450
36. Gillis TP, Tullius MV, Horwitz MA. Rbcg30-Induced Immunity and Cross-Protection Against Mycobacterium Lepae Challenge Are Enhanced by Boosting With the Mycobacterium Tuberculosis 30-Kilodalton Antigen 85b. *Infect Immun* (2014) 82(9):3900–9. doi: 10.1128/IAI.01499-13
37. Uehara Y, Mochizuki M, Matsuno K, Haino T, Asai A. Novel High-Throughput Screening System for Identifying STAT3-SH2 Antagonists. *Biochem Biophys Res Commun* (2009) 380(3):627–31. doi: 10.1016/j.bbrc.2009.01.137
38. Rose S, Misharin A, Perlman H. A Novel Ly6C/Ly6G-Based Strategy to Analyze the Mouse Splenic Myeloid Compartment. *Cytom Part A* (2012) 81A(4):343–50. doi: 10.1002/cyto.a.22012
39. Geissmann F, Jung S, Littman DR. Blood Monocytes Consist of Two Principal Subsets With Distinct Migratory Properties. *Immunity* (2003) 19(1):71–82. doi: 10.1016/S1074-7613(03)00174-2
40. Xavier MN, Winter MG, Spees AM, Den Hartigh AB, Nguyen K, Roux CM, et al. Ppar γ -Mediated Increase in Glucose Availability Sustains Chronic Brucella Abortus Infection in Alternatively Activated Macrophages. *Cell Host Microbe* (2013) 14(2):159–70. doi: 10.1016/j.chom.2013.07.009
41. Swirski FK, Nahrendorf M, Etzrodt M, Wildgruber M, Cortez-Retamozo V, Panizzi P, et al. Identification of Splenic Reservoir Monocytes and Their Deployment to Inflammatory Sites. *Sci* (80-) (2009) 325(5940):612–6. doi: 10.1126/science.1175202
42. Cambier CJ, Takaki KK, Larson RP, Hernandez RE, Tobin DM, Urdahl KB, et al. Mycobacteria Manipulate Macrophage Recruitment Through Coordinated Use of Membrane Lipids. *Nature* (2014) 505(7482):218–22. doi: 10.1038/nature12799
43. Huang L, Nazarova EV, Tan S, Liu Y, Russell DG. Growth of Mycobacterium Tuberculosis In Vivo Segregates With Host Macrophage Metabolism and Ontogeny. *J Exp Med* (2018) 215(4):1135–52. doi: 10.1084/jem.20172020
44. Khader SA, Gopal R. IL-17 in Protective Immunity to Intracellular Pathogens. *Virulence* (2010) 1(5):423–7. doi: 10.4161/viru.1.5.12862
45. Mayer-Barber KD, Andrade BB, Oland SD, Amaral EP, Barber DL, Gonzales J, et al. Host-Directed Therapy of Tuberculosis Based on Interleukin-1 and Type I Interferon Crosstalk. *Nature* (2014) 511(7507):99–103. doi: 10.1038/nature13489
46. Darrah PA, Patel DT, De Luca PM, Lindsay RWB, Davey DF, Flynn BJ, et al. Multifunctional TH1 Cells Define a Correlate of Vaccine-Mediated Protection Against Leishmania Major. *Nat Med* (2007) 13(7):843–50. doi: 10.1038/nm1592
47. Seder RA, Darrah PA, Roederer M. T-Cell Quality in Memory and Protection: Implications for Vaccine Design. *Nat Rev Immunol* (2008) 8(4):247–58. doi: 10.1038/nri2274
48. Lindenström T, Agger EM, Korsholm KS, Darrah PA, Aagaard C, Seder RA, et al. Interleukin Subunit Vaccination Provides Long-Term Protective Immunity Characterized by Multifunctional CD4 Memory T Cells. *J Immunol* (2009) 182(12):8047–55. doi: 10.4049/jimmunol.0801592
49. Derrick SC, Yabe IM, Yang A, Morris SL. Vaccine-Induced Anti-Tuberculosis Protective Immunity in Mice Correlates With the Magnitude and Quality of Multifunctional CD4 T Cells. *Vaccine* (2011) 29(16):2902–9. doi: 10.1016/j.vaccine.2011.02.010
50. Hammarlund E, Lewis MW, Hansen SG, Strelow LI, Nelson JA, Sexton GJ, et al. Duration of Antiviral Immunity After Smallpox Vaccination. *Nat Med* (2003) 9(9):1131–7. doi: 10.1038/nm917
51. Shafiani S, Tucker-Heard G, Kariyone A, Takatsu K, Urdahl KB. Pathogen-Specific Regulatory T Cells Delay the Arrival of Effector T Cells in the Lung During Early Tuberculosis. *J Exp Med* (2010) 207(7):1409–20. doi: 10.1084/jem.20091885
52. Gupta S, Cheung L, Pokkali S, Winglee K. Suppressor Cell – Depleting Immunotherapy With Denileukin Diftitox is an Effective Host-Directed Therapy for Tuberculosis. *J Infect Dis* (2017) 3:1883–7. doi: 10.1093/infdis/jix208
53. Bhattacharya D, Dwivedi VP, Kumar S, Reddy MC, Van Kaer L, Moodley P, et al. Simultaneous Inhibition of T Helper 2 and T Regulatory Cell Differentiation by Small Molecules Enhances Bacillus Calmette-Guerin Vaccine Efficacy Against Tuberculosis. *J Biol Chem* (2014) 289(48):33404–11. doi: 10.1074/jbc.M114.600452
54. Kaufmann SHE, Dorhoi A, Hotchkiss RS, Bartenschlager R. Host-Directed Therapies for Bacterial and Viral Infections. *Nat Rev Drug Discovery* (2017) 17(1):35–56. doi: 10.1038/nrd.2017.162
55. Singh DK, Dwivedi VP, Ranganathan A, Bishai WR, Van Kaer L, Das G. Blockade of the Kv1.3 K⁺ Channel Enhances BCG Vaccine Efficacy by Expanding Central Memory T Lymphocytes. *J Infect Dis* (2016) 214(9):1456–64. doi: 10.1093/infdis/jiw395
56. Couper KN, Blount DG, Riley EM. IL-10: The Master Regulator of Immunity to Infection. *J Immunol* (2008) 180(9):5771–7. doi: 10.4049/jimmunol.180.9.5771
57. Redford PS, Boonstra A, Read S, Pitt J, Graham C, Stavropoulos E, et al. Enhanced Protection to Mycobacterium Tuberculosis Infection in IL-10-Deficient Mice is Accompanied by Early and Enhanced Th1 Responses in the Lung. *Eur J Immunol* (2010) 40(8):2200–10. doi: 10.1002/eji.201040433
58. Keane J, Remold HG, Kornfeld H. Virulent Mycobacterium Tuberculosis Strains Evade Apoptosis of Infected Alveolar Macrophages. *J Immunol* (2000) 164(4):2016–20. doi: 10.4049/jimmunol.164.4.2016
59. Chen M, Divangahi M, Gan H, Shin DSJ, Hong S, Lee DM, et al. Lipid Mediators in Innate Immunity Against Tuberculosis: Opposing Roles of PGE2 and LXA4 in the Induction of Macrophage Death. *J Exp Med* (2008) 205(12):2791–801. doi: 10.1084/jem.20080767
60. Divangahi M, Chen M, Gan H, Desjardins D, Hickman TT, Lee DM, et al. Mycobacterium Tuberculosis Evades Macrophage Defenses by Inhibiting Plasma Membrane Repair. *Nat Immunol* (2009) 10(8):899–906. doi: 10.1038/ni.1758

61. McClean CM, Tobin DM. Macrophage Form, Function, and Phenotype in Mycobacterial Infection: Lessons From Tuberculosis and Other Diseases. Napier B, Editor. *Pathog Dis* (2016) 74(7):ftw068. doi: 10.1093/femspd/ftw068
62. Marakalala MJ, Raju RM, Sharma K, Zhang YJ, Eugenin EA, Prideaux B, et al. Inflammatory Signaling in Human Tuberculosis Granulomas Is Spatially Organized. *Nat Med* (2016) 22(5):531–8. doi: 10.1038/nm.4073
63. Counoupas C, Pinto R, Nagalingam G, Hill-Cawthorne GA, Feng CG, Britton WJ, et al. Mycobacterium Tuberculosis Components Expressed During Chronic Infection of the Lung Contribute to Long-Term Control of Pulmonary Tuberculosis in Mice. *NPJ Vaccines* (2016) 16012:1–11. doi: 10.1038/npjvaccines.2016.12
64. Henaio-Tamayo M, Ordway DJ, Orme IM. Memory T Cell Subsets in Tuberculosis: What Should We be Targeting? *Tuberculosis* (2014) 94(5):455–61. doi: 10.1016/j.tube.2014.05.001
65. Youngblood B, Hale JS, Ahmed R. T-Cell Memory Differentiation: Insights From Transcriptional Signatures and Epigenetics. *Immunology* (2013) 139(3):277–84. doi: 10.1111/imm.12074
66. Akondy RS, Fitch M, Edupuganti S, Yang S, Kissick HT, Li KW, et al. Origin and Differentiation of Human Memory CD8 T Cells After Vaccination. *Nature* (2017) 552(7685):362–7. doi: 10.1038/nature24633
67. Youngblood B, Hale JS, Kissick HT, Ahn E, Xu X, Wieland A, et al. Effector CD8 T Cells Dedifferentiate Into Long-Lived Memory Cells. *Nature* (2017) 552(7685):404–9. doi: 10.1038/nature25144
68. Orme IM. The Achilles Heel of BCG. *Tuberculosis* (2010) 90(6):329–32. doi: 10.1016/j.tube.2010.06.002
69. Bhattacharya D, Dwivedi VP, Maiga M, Maiga M, Van Kaer L, Bishai WR, et al. Small Molecule-Directed Immunotherapy Against Recurrent Infection by Mycobacterium Tuberculosis. *J Biol Chem* (2014) 289(23):16508–15. doi: 10.1074/jbc.M114.558098
70. Bali P, Tousif S, Das G, Van Kaer L. Strategies to Improve BCG Vaccine Efficacy. *Immunotherapy* (2015) 7(9):945–8. doi: 10.2217/imt.15.60
71. Scott-Browne JP, Shafiani S, Tucker-Heard G, Ishida-Tsubota K, Fontenot JD, Rudensky AY, et al. Expansion and Function of Foxp3-Expressing T Regulatory Cells During Tuberculosis. *J Exp Med* (2007) 204(9):2159–69. doi: 10.1084/jem.20062105
72. Busker S, Qian W, Haraldsson M, Espinosa B, Johansson L, Attarha S, et al. Irreversible TrxR1 Inhibitors Block STAT3 Activity and Induce Cancer Cell Death. *Sci Adv* (2020) 6(12):eaax7945. doi: 10.1126/sciadv.aax7945
73. Busker S, Page B, Arnér ESJ. To Inhibit TrxR1 is to Inactivate STAT3–Inhibition of TrxR1 Enzymatic Function by STAT3 Small Molecule Inhibitors. *Redox Biol* (2020) 101646:1–9. doi: 10.1016/j.redox.2020.101646
74. Mtwebana SS, Prinsloo E. The Commercially Available STAT3 Inhibitor 5,15-Diphenylporphyrin (5,15-DPP) Does Not Directly Interact With STAT3 Core Residues 127–722. *BMC Res Notes* (2020) 13(1):1–4. doi: 10.1186/s13104-020-05189-w
75. Ansari MA, Zubair S, Mahmood A, Gupta P, Khan AA, Gupta UD, et al. RD Antigen Based Nanovaccine Imparts Long Term Protection by Inducing Memory Response Against Experimental Murine Tuberculosis. *PloS One* (2011) 6(8):e22889. doi: 10.1371/journal.pone.0022889
76. Collins LA, Franzblau SG. Microplate Alamar Blue Assay Versus BACTEC 460 System for High- Throughput Screening of Compounds Against Mycobacterium Tuberculosis and Mycobacterium Avium. *Antimicrob Agents Chemother* (1997) 41(5):1004–9. doi: 10.1128/AAC.41.5.1004

Conflict of Interest: The authors declare that the research was conducted in the absence of any commercial or financial relationships that could be construed as a potential conflict of interest.

Publisher's Note: All claims expressed in this article are solely those of the authors and do not necessarily represent those of their affiliated organizations, or those of the publisher, the editors and the reviewers. Any product that may be evaluated in this article, or claim that may be made by its manufacturer, is not guaranteed or endorsed by the publisher.

Copyright © 2021 Ahmad, Umar, Khan, Jamal, Gupta, Zubair, Gupta and Owais. This is an open-access article distributed under the terms of the Creative Commons Attribution License (CC BY). The use, distribution or reproduction in other forums is permitted, provided the original author(s) and the copyright owner(s) are credited and that the original publication in this journal is cited, in accordance with accepted academic practice. No use, distribution or reproduction is permitted which does not comply with these terms.

Amyloid Form of Ovalbumin Evokes Native Antigen-specific Immune Response in the Host

PROSPECTIVE IMMUNO-PROPHYLACTIC POTENTIAL

Received for publication, July, 6, 2014, and in revised form, December 3, 2014. Published, JBC Papers in Press, December 15, 2014, DOI 10.1074/jbc.M113.540989

Saba Tufail^{†1}, Mohammad Owais^{‡2}, Shadab Kazmi[‡], Renu Balyan[§], Jasneet Kaur Khalsa[§], Syed Mohd. Faisal[‡], Mohd. Asif Sherwani[‡], Manzoor Ahmad Gattoo[†], Mohd. Saad Umar[‡], and Swaleha Zubair^{||3}

From the [†]Interdisciplinary Biotechnology Unit, Aligarh Muslim University, Aligarh, U.P.-202002, the [§]National Institute of Immunology, New Delhi, the ^{||}Department of Biochemistry, JNMC, Aligarh Muslim University, Aligarh, U.P.-202002, and the [‡]Women's College, Aligarh Muslim University, Aligarh, U.P.-202002, India

Background: Amyloids have recently been found to be reversible and dynamic. They release the precursor peptide/protein in a slow and sustained manner.

Results: Antibodies produced in response to amyloid immunization could recognize native antigen.

Conclusion: OVA amyloids release proteins harboring native antigen epitopes.

Significance: The slow and sustained release of native antigen from amyloids makes them potential candidates for inducing a protective antibody response.

Amyloids are highly organized protein aggregates that arise from inappropriately folded versions of proteins or polypeptides under both physiological as well as simulated ambiances. Once thought to be irreversible assemblies, amyloids have begun to expose their more dynamic and reversible attributes depending upon the intrinsic properties of the precursor protein/peptide and experimental conditions such as temperature, pressure, structural modifications in proteins, or presence of chemicals in the reaction mixture. It has been repeatedly proposed that amyloids undergo transformation to the bioactive peptide/protein forms under specific conditions. In the present study, amyloids assembled from the model protein ovalbumin (OVA) were found to release the precursor protein in a slow and steady manner over an extended time period. Interestingly, the released OVA from amyloid depot was found to exhibit biophysical characteristics of native protein and reacted with native-OVA specific monoclonal as well as polyclonal antibodies. Moreover, antibodies generated upon immunization of OVA amyloid aggregates or fibrils were found to recognize the native form of OVA. The study suggests that amyloids may act as depots for the native form of the protein and therefore can be exploited as vaccine candidates, where slow antigen release over extended time periods is a pre-requisite for the development of desired immune response.

There is a general consensus that under destabilizing conditions, abnormally folded intermediates of several proteins have a strong tendency to self-aggregate into a polymeric amyloid

fibril (1, 2). Various proteins and peptides have been found to form amyloids in diverse conditions implying that amyloid formation is a generic feature of peptide and proteins (3–5). The amyloid fibrils harbor a core formed by cross- β -structures where β -strands are oriented perpendicularly to the main fibril axis (1, 6). The β -cores can bind to the amyloid binding dyes thioflavin T (ThT)⁴ and Congo Red (7, 8). Amyloid bodies have been associated with the pathogenesis of several neurodegenerative diseases such as Alzheimer, Parkinson, or Creutzfeldt-Jakob disease etc. (9–11). In downright contrast, a few naturally existing amyloids have been found to perform non-pathogenic rather beneficial functions that are crucial for the survival of the host, such as curli fibrils expressed by *Escherichia coli* assist in cell-cell contact (12), amyloid protein of chorion protects oocyte, and developing embryo of silkworm (13). Likewise, fungal prions including yeast and HETs prions in certain cases enhance survival of the host (14–16), whereas Pmel17 amyloid promotes skin pigmentation in humans (17). Also, peptides and protein hormones present in the pituitary secretory granules have been found to carry amyloid-like cross- β -sheet rich conformation (18). Amyloids have also been associated with transfer of genetic information or synaptic changes linked to memory (19–22). Moreover, some recent findings enumerate that artificially or *in vitro* synthesized amyloids can also perform beneficial biological activities *in vivo* (23, 24).

Amyloid fibrils classically viewed to be highly stable structures capable of withstanding perturbing environmental conditions have begun to be realized as more of dynamic entities that may revert back to their native form. Variations in temperature (25) and pressure (26, 27), contamination by chemical denaturants (28), and structural modifications in proteins (29, 30) have been found to destabilize amyloid fibrils. Employing hydrogen/deuterium exchange experiments, Carulla *et al.* (31) have inge-

¹ Supported by the Council of Scientific and Industrial Research (CSIR), India, Senior Research Fellowship (SRF).

² To whom correspondence may be addressed: Interdisciplinary Biotechnology Unit, Aligarh Muslim University, Aligarh, U.P.-202002, India. E-mail: owais_lakhnawi@yahoo.com.

³ To whom correspondence may be addressed: Women's College, Aligarh Muslim University, Aligarh, U.P.-202002, India. E-mail: swalehazubair@yahoo.com.

⁴ The abbreviations used are: ThT, thioflavin T; DTH, delayed type hypersensitivity; PB, phosphate buffer; CD, circular dichroism; ELISA, enzyme linked immunosorbent assay; Th1, type 1 T helper; Th2, type 2 T helper.

niously demonstrated that monomeric Src homology domain 3 molecules incorporated into Src homology domain 3 amyloid fibrils continuously recycle between the fibril and the monomer state by a dissociation/re-association mechanism at the fibril ends. The recent findings by Kardos *et al.* (25) enumerated dissociation of β_2 -microglobulin fibrils to be a reversible and dynamic process reaching equilibrium between fibrils and monomers following time kinetics of the order of a few minutes. In an earlier study, β_2 -microglobulin fibrils were found to completely dissociate to monomeric β_2 -microglobulin upon treatment with dimethyl sulfoxide (28). Binger *et al.* (30) have shown that hydrogen peroxide-mediated oxidation of methionine residues in the preformed apoCII fibrils reverses their assembly and dissociates the monomer in a time-dependant manner. Also, approximately 2–4% of the monomers have been found to remain unpolymerized at the culmination of A β 1–40 fibril formation (32). The presence of the “unpolymerized free monomeric pool” provides further indication for the existence of an equilibrium between the monomers present in solution and those incorporated into fibrils. Moreover, in a few recent reports non-fibrillar as well as fibrillar aggregates generated from the same protein have been found to exhibit varied release kinetics depending upon the compactness and ordered nature of the aggregates (23, 24). Aggregates obtained at earlier incubation time periods have been found to attain rapid saturation in the release profile in comparison to fibril species formed at later stages. Release of monomers from some of the aggregates could reach saturation only after a period of over 15 or 30 days, which indicates that in such cases equilibrium between the fibril or other amyloid aggregates and the released monomers are attained after long time periods and therefore the aggregates could subsequently release the monomeric protein in a sustained manner over an extended time course. Although overwhelming information is available regarding conformation of amyloid fibrils and release of proteins from them, there remains a paucity of reports on the conformation of the released proteins and peptides.

In the present study, OVA (a non-inhibitory member of serpin protein family) was taken as a model protein for the synthesis of amyloid bodies. OVA was continuously agitated at varying pH conditions (pH 2.5, 7.0, and 10) and the aggregates obtained after various incubation periods were characterized by turbidity measurements, Rayleigh scattering studies, ThT, and Congo Red binding, CD spectral measurements etc. Finally, the formation of fibrils was confirmed by transmission electron microscopy. Furthermore, release of OVA from various aggregates was monitored over an extended time period followed by assessing the state of released product and its conformational integrity. The amyloid aggregates formed at either pH 2.5 or 7.0 were then studied for their immunological properties. The antibodies generated in response to the immunizations were investigated for their affinity with the native state of the antigen employing ELISA and dot blot analysis. We further evaluated Th1/Th2 cytokine bias, lymphocyte proliferation, delayed type hypersensitivity, and nitric oxide (NO) production induced by OVA aggregates in immunized animals to investigate their potential to evoke desired immune responses in the host.

EXPERIMENTAL PROCEDURES

Chemicals and Reagents—All the reagents used were of the highest purity available. OVA (A2512), thioflavin T, Congo Red, and fetal calf serum were purchased from Sigma. IgG2a (R35–95) isotype control was procured from eBiosciences (San Diego, CA). IgG1 and IgG2a isotypes (550487), and cytokines *viz.* IL-4, interferon- γ , and IL-12 cytokine estimation kits were procured from BD Biosciences, OptEIA (Franklin Lakes, NJ). RPMI 1640, antimycotic solution, and plasticwares were purchased from BD Biosciences (San Diego, CA). Anti-OVA monoclonal antibodies 2D11 and 3G2E1D9 were purchased from Santa Cruz Biotechnology, Inc.

Fibril Formation—OVA was dissolved in PBS (pH 7.0) (24) or glycine-HCl (pH 2.5) or glycine-NaOH (pH 10) buffers (carrying 0.01% azide) at a concentration of 1 mg/ml and incubated at room temperature under continuous agitation (at 90 rpm). Aliquots collected at various time points were pelleted down at $15,000 \times g$ for 15 min using Sigma 3K30 (Germany) microcentrifuge. Under these conditions, monomeric OVA does not sediment and thus remained in solution only. Fibril formation was established by ThT and Congo Red binding assays and transmission electron microscopy. There was no aggregate formation upon incubation of OVA at pH 10 (data not shown).

Rayleigh Scattering Measurements—Rayleigh scattering measurements were performed on a Hitachi F-4500 fluorescence spectrophotometer at room temperature using a cell with a 1-cm light path. The excitation and emission wavelengths were both set at 350 nm, and the slit length was 5 nm.

Turbidity Measurements—For turbidity measurements, the incubated samples collected at various time points were monitored by UV absorbance at 350 nm using a PerkinElmer UV-visible spectrometer model λ 25 in a 1-cm path length cuvette at room temperature.

Congo Red Binding Studies—Congo Red solution (20 μ M) prepared in phosphate buffer (PB) (pH 7.4) (using a stock solution (1 mM) of Congo Red prepared in ethanol) was incubated with 100 μ g of aggregates for 30 min at room temperature. UV absorbance was measured in the spectral range at 300–700 nm using a PerkinElmer UV-visible spectrometer model λ 25. Congo Red solution (20 μ M) in phosphate buffer served as a control (Congo Red-only spectrum), and absorbance of 100 μ g of native OVA mixed with 20 μ M Congo Red solution was also measured.

ThT Binding Studies—OVA aggregates (100 μ g) obtained at various time points were incubated with 30 μ M ThT solution (30 μ l of 1 mM ThT stock solution) at room temperature and fluorescence was measured on Hitachi F-4500 fluorescence spectrophotometer after 30 min. The bound ThT amyloid was excited at 450 nm and spectra were recorded from 460 to 560 nm. The excitation and emission slit widths were fixed at 5 and 10 nm, respectively.

Interaction of various amyloid species obtained at various time points with ThT was also assessed by fluorescence microscopy. Incubated OVA aggregates obtained at various time points, *viz.* days 2, 4, 7, 10, and 15 were pelleted down at $15,000 \times g$ for 15 min. The pellets obtained were incubated with 20 μ M ThT for 30 min at room temperature and then trans-

ferred onto a glass slide to be analyzed under fluorescence microscope (Axio, HBU 50/AC; Zeiss, Gottingen, Germany).

CD Measurements—A JASCO spectropolarimeter (J-815) was used for circular dichroic measurements using quartz cell with 0.1-cm path length. The temperature was controlled at room temperature using a Peltier Thermostat with Multitech water circulator and the instrument was calibrated using D10-camphor sulfonic acid. A scan speed of 100 nm/min and response time of 2 s were used for spectra collection. Scans were performed for each sample in the range of 200–250 nm with final protein concentrations being 200 μ g/ml.

Transmission Electron Microscopy—For electron microscopy, 6 μ l of protein sample (100 μ g) was spread on a carbon-coated copper grid that was further negatively stained with 2% (w/v) uranyl acetate. The grid was examined under a JEOL transmission electron microscope operating at an accelerating voltage of 200 kV.

In Vitro Release Kinetics—OVA (1 mg/ml of PBS, pH 7.0, and glycine-HCl, pH 2.5) samples incubated for fibrillation were withdrawn at various time points. The amyloids formed were isolated by pelleting at $15,000 \times g$ for 15 min. The pellets obtained were washed three times with PB (pH 7.4) and re-suspended in PB (pH 7.4). The kinetics of OVA release into PB (pH 7.4) was monitored spectrophotometrically at 280 nm (24) as well as by determining intrinsic fluorescence measurements (32). The supernatant obtained after centrifugation was analyzed at various time points for approximately 15 days using PerkinElmer UV-visible spectrometer model λ 25 and Hitachi F-4500 fluorescence spectrophotometer, respectively.

Size Exclusion Chromatography—Five milliliters of the sample containing OVA released from various aggregates after 12 days (approximately 10 mg) was applied to a 83-cm long column with an internal diameter of 2.3 cm, filled with about 340 ml of preswollen Bio-Gel P10 (Bio-Rad), and equilibrated with 20 mM phosphate-HCl buffer (pH 3.0) containing 18 mM NaCl. The flow rate was adjusted to 35 ml/h and 1.0-ml fractions were collected. Absorbance of the collected fractions was measured at 280 nm using PerkinElmer UV-visible spectrometer model λ 25 and plotted against the elution volume.

Western Blot Analysis of the OVA Released from Various Aggregates—Released OVA from various aggregates after various incubation periods was resolved by electrophoresis on a 12% sodium dodecyl sulfate-polyacrylamide gel and transferred onto PVDF membrane. After blocking in 5% nonfat dry milk prepared in phosphate-buffered saline (PBS) with Tween (PBST), the membrane was washed three times with PBST and incubated for 2 h at 37 °C with either anti-OVA polyclonal or 3G2E1D9 monoclonal antibody. After incubation and stipulated washing steps, the membrane was incubated with horseradish peroxidase-conjugated goat anti-mouse antibody (1:5000) for 1 h at 37 °C. Finally, post washing, the bands onto the membrane were developed by enhanced chemiluminescence (ECL) using ECL kit (Bio-Rad).

Animals—Inbred female BALB/c mice (6–8 weeks old, 20 ± 2 g) were obtained from the Animal House Facility of the Institute. The BALB/c mice were housed in commercially available polypropylene cages and maintained under controlled temperature conditions on a 12-h light/dark cycle and had free access

to food and water *ad libitum*. OT-I and OT-II mice originally obtained from The Jackson Laboratory were a gift from Dr. Satyajit Rath (National Institute of Immunology, New Delhi, India). OT-I and OT-II mice were bred and maintained in the Animal House Facility of the National Institute of Immunology (New Delhi, India). All the animal experiments were performed according to the National Regulatory Guidelines issued by the Committee for the Purpose of Control and Supervision of Experiments on Animals (CPCSEA).

Mode and Schedule of Immunization—Animals were immunized subcutaneously in the lower abdominal region aseptically with 50 μ g of OVA amyloid bodies (obtained from fibrillation reaction at various time points). A booster was given 3 weeks after the first immunization with 25 μ g of the corresponding form of protein fibril.

Collection of Sera—The blood was collected from mice after 5 days of last booster. Sera were separated from the clotted blood by centrifugation at $1500 \times g$ for 10 min at 4 °C. Finally, the supernatant was collected for ELISA analysis and purification of polyclonal antibodies.

Determination of Antigen-specific Total IgGs by ELISA—Antigen-specific total IgGs against the native as well as OVA aggregates were determined in the sera of mice immunized with various aggregates of OVA formed at various time points following the protocol as described elsewhere (33). Briefly, 100 μ l (2 μ g) of native OVA as well as OVA aggregates obtained at various time points were dissolved in carbonate/bicarbonate buffer (0.05 M, pH 9.6) and poured into 96-well microtiter plates that were further incubated overnight at 4 °C. The plates were then incubated with serially diluted sera at 37 °C for 2 h, after the usual washing and blocking steps. Furthermore, the plates were washed again and 100 μ l of (1:5000 dilution of stock) horseradish peroxidase-conjugated goat anti-mouse antibodies were added to each well and the plates were incubated at 37 °C for 1 h. After the usual plate washing, 100 μ l of substrate solution (6 mg *o*-phenylenediamine) in 12 ml of substrate buffer with 5 μ l of 30% H₂O₂ was added to the wells and the plates were finally incubated at 37 °C for 40 min. The reaction was terminated by the addition of 50 μ l of 7% H₂SO₄. The absorbance was read at 490 nm with a microtiter plate reader (Bio-Rad).

ELISA of OVA Released from Various Aggregates—Briefly, 96-well microtiter plates were incubated overnight with 100 μ l (2 μ g) of OVA released from various aggregates in carbonate/bicarbonate buffer (0.05 M, pH 9.6) at 4 °C. After the usual washing and blocking steps, the plates were finally incubated with serially diluted anti-native OVA-specific polyclonal and 2D11 monoclonal antibodies at 37 °C for 2 h. After washing the plates, 100 μ l of (1:5000 dilution of stock) horseradish peroxidase-conjugated goat anti-mouse antibodies were added to each well and the plates were incubated at 37 °C for 1 h. Substrate solution (100 μ l) was added to the wells after the usual plate washing, which were finally incubated at 37 °C for 40 min. For terminating the reaction, 50 μ l of 7% H₂SO₄ was added to the wells. The absorbance was read at 490 nm with a microtiter plate reader (Bio-Rad).

Determination of Antibody Isotype in Sera of Immunized Mice—Sera from mice immunized with day 4 and 7 aggregates formed at both pH 2.5 and 7.0 were analyzed for antibody isotypes using the protocol described elsewhere (34). Briefly, 2 μ g (100 μ l) of antigen in carbonate/bicarbonate buffer (0.05 M, pH 9.6) was added to 96-well microtiter plates that were incubated overnight at 4 °C. After washing and blocking steps, the plates were incubated with serially diluted sera at 37 °C for 2 h. After excessive washing of the plates, 100 μ l of (1:5000 dilution of stock) goat anti-mouse anti-IgG1, and IgG2a antibodies were added in each well and incubated for 1 h at 37 °C. Plates were again washed and 100 μ l of (1:5000 dilution of stock) horseradish peroxidase-conjugated rabbit anti-goat antibodies were added to each well and each plate was incubated at 37 °C for 1 h. After further washing of the plates, 100 μ l of substrate solution was added to the wells and the plates were finally incubated at 37 °C for 40 min. The reaction was stopped by the addition of 50 μ l of 1 M H₂SO₄. The absorbance was read at 490 nm with a microtiter ELISA plate reader (Bio-Rad).

Measurement of DTH Response—The animals were immunized with day 4 and 7 OVA aggregates generated at both pH 2.5 and 7.0 in their inguinal region and the delayed type hypersensitivity (DTH) response was assessed at various time points. The mice were footpad tested to determine their DTH reactions to native as well as various OVA aggregate forms. DTH reactions were elicited by the injection of various OVA aggregates (50 μ g) as well as native OVA in the right footpad of each mouse and PBS into the left footpad. The thickness of each footpad was measured just before and after 36 h post-injection of OVA aggregates and PBS using a digital gauge caliper (Aerospace and Engineering Tools Ltd., Bolton, UK). DTH reactions were evaluated by the increase in footpad thickness as determined by the following formula (right footpad at testing time – right footpad at 0 h): (left footpad at testing time – left footpad at 0 h).

Determination of NO Production—Mice were sacrificed 1 week post booster, and peritoneal macrophages were isolated. The peritoneal macrophages were grown in culture plates and pulsed with OVA (final concentration 10 μ g/well). After 24 h, 100 μ l of culture supernatant was collected from each well, mixed with an equal volume of Griess reagent (1% sulfanilamide and 0.1% *N*-(1-naphthyl)ethylenediamine dihydrochloride in 2.5% H₃PO₄), and further incubated for 10 min at 25 °C and absorbance was determined at 550 nm in an ELISA reader (Bio-Rad).

T Lymphocyte Isolation from Spleens of Immunized Mice—Mice immunized with native as well as various aggregated forms of OVA were sacrificed on post day 5 after the last booster. T lymphocytes were isolated from the spleens of sacrificed mice as described elsewhere (34). Briefly, spleens isolated from animals belonging to various immunized groups were macerated and suspension was treated with ACK lysis buffer (0.15 mol/liter of ammonium chloride, 10 mmol/liter of potassium/bicarbonate, and 88 mmol/liter of edetic acid) for lysis of the red blood cells. The cell suspension was centrifuged at 1500 \times g for 5 min, and the cell pellet was washed with Hanks' balanced salt solution 3 times and resuspended in RPMI 1640

medium containing 10% fetal calf serum and 0.1% antimycotic mixture.

T-cell Proliferation Assay for Lymphocytes Isolated from Immunized BALB/c Mice—Lymphocyte proliferation assay was performed as described elsewhere (34). Briefly, lymphocytes isolated from the spleens of mice belonging to various immunized groups were incubated in round bottomed 96-well plates (2 \times 10⁵ cells/well) in 200 μ l of RPMI 1640 medium with 10% fetal calf serum. Splenic cells isolated from groups of mice immunized with native or appropriate OVA aggregates were incubated with 20 μ g of the corresponding matching forms of OVA. After 72 h, the cultures were pulsed with 0.5 μ Ci of [³H]thymidine. After 16 h, the plates were harvested onto glass-fiber filter mats by the use of a Tomtec-Harvester-96 (Tomtec). The incorporated radioactivity was measured with liquid scintillation spectroscopy (Wallac-1450 Microbeta Trilux; PerkinElmer Life Sciences).

Lymphocyte Proliferation Assay for TCR-transgenic OT-I and OT-II Cells—OVA-specific T cell proliferation assay for TCR-transgenic OT-I and OT-II cells was performed by measuring [³H]thymidine incorporation, for determining antigen-specific response to different OVA aggregates. The assays were performed in Immunobiology Laboratory-2 at the National Institute of Immunology, New Delhi. Briefly, OT-I and OT-II splenocytes were isolated and cultured in 96-well culture plates at 1 \times 10⁵ splenocytes/well in 200 μ l of complete RPMI medium. The splenocytes were stimulated with titrating concentrations of OVA aggregates. The plates were incubated in a humid atmosphere of 5% CO₂ at 37 °C and pulsed after 60 h with 0.5 μ Ci/well for measurement of [³H]thymidine incorporation at the end of 72 h. Cells were harvested using a Filler-Mate cell harvester (PerkinElmer Life Sciences) and incorporation of [³H]thymidine was determined by a Top Count scintillation counter (PerkinElmer Life Sciences).

Cytokine Assay: Determination of IFN- γ , IL-4, and IL-12 by Sandwich ELISA—Th1 as well as Th2 cytokines induced by lymphocytes upon their culture in the co-presence of various aggregates of OVA were estimated using appropriate and specific biotinylated antibody pairs according to the manufacturer's protocols. Briefly, 96-well microtiter plates were coated with 50 μ l of the purified capture antibodies in carbonate/bicarbonate buffer (pH 9.5) at 4 °C. After the usual washing and blocking steps, 50 μ l of the supernatant (isolated from cultured splenocytes after 48 h) was poured in each well for determining the level of cytokine induced. Plates were washed and incubated with biotinylated polyclonal goat anti-mouse cytokine detection antibody. Furthermore, after washing the plates, 100 μ l of streptavidin-horseradish peroxidase conjugate was added to each well and plates were incubated for 30 min at room temperature. The plates were then washed and the colored complex was developed with tetramethylbenzidine. The absorbance was read at 450 nm with a microtiter plate reader (Bio-Rad). A known specific recombinant cytokine was used as standard for calculating the level of the given cytokine in the samples tested, and the concentration was expressed as pg/ml.

Dot Blot Assay—The native form of OVA (10 μ g), various aggregate forms, and OVA released from various aggregates were spotted onto PVDF strips (with dimension of \sim 10 by 4

mm), which were further allowed to dry at room temperature. The strips were rinsed briefly in PBS (pH 7.4) containing Tween 20 (PBST) and incubated overnight at 4 °C in 5% nonfat dry milk in PBST to block the residual binding sites on the paper. The strips were rinsed three times in PBST. The strips coated with various aggregates were incubated with antibodies obtained from the animals immunized with corresponding aggregates. The native OVA-coated strips were then incubated with various anti-amyloid OVA antibodies produced in mice. The strips spotted with released OVA from various aggregates were allowed to react with native OVA-specific polyclonal and 2D11 monoclonal antibodies. After the stipulated incubation, the strips were washed three times in PBST and further incubated for 1 h at 37 °C with horseradish peroxidase-conjugated goat anti-mouse antibody (1:5000). The strips were washed with PBST three times and finally the immunoreactive dots were developed on x-ray film using a ECL kit (Bio-Rad). A clearly defined greyish to black spot at the site where the antigen was spotted was considered a positive result. A nonspecific protein (Human Serum Albumin) was spotted onto membranes as control in all the dot blot assays performed.

Interaction of Macrophages with Amyloid Aggregates—Macrophages (1×10^6 cells) were isolated from the intraperitoneal cavity of thioglycollate-primed BALB/c mice following the protocol as described elsewhere (35). The recovered cells consisted of >99% macrophages as demonstrated by histochemistry and FACS analysis using labeled anti-F4/80 antibodies (data not shown). The macrophages were incubated with 100 μ g of FITC-tagged aggregates for 1–2 h at 37 °C in a humidified atmosphere of 5% CO₂. The cells were fixed on a slide for observation using a fluorescent microscope (Axio, HBU 50/AC; Zeiss, Gottingen, Germany).

Ovalbumin Molecular Modeling—A three-dimensional ribbon model of OVA was drawn with PyMOL by importing the crystal structure of OVA from the Protein Data Bank with code 1OVA. The selected sequences were highlighted with different colors.

Statistical Analysis—Data were analyzed and two groups were compared using Student's *t* test and one-way analysis of variance (Holm-Sidak method) was used to compare all groups to each other. *p* values < 0.05 were considered significant. SigmaPlot (versions 10 and 11; SigmaPlot software, San Jose, CA) software was used for data presentation.

RESULTS

Continuous Shaking over an Extended Time Period Induces Aggregation of Soluble OVA—Fluorescence intensity at 350 nm is a useful tool to detect aggregation in proteins (36). Taking this fact into consideration, the extent of light scattering was measured in OVA samples obtained after various incubation times (day 0 to 15) when OVA solution in PBS (pH 7.0) or glycine-HCl (pH 2.5) was shaken at 90 rpm. With an increase in incubation time, an enhancement in fluorescence intensity was observed in samples at both pH 2.5 as well as pH 7.0. The increase in fluorescence intensity for pH 2.5 samples was more prominent and significant when compared with samples incubated at pH 7.0. When compared with native OVA, fluorescence intensity was found to increase consistently with incuba-

tion times from 1 to 36 h suggesting aggregate formation. However, the magnitude of increment was less than 5-fold (data not shown). As shown in Fig. 1A, *a*, all the samples collected (at both pH 2.5 and 7.0) after various time periods exhibited a more than 7-fold increase in fluorescence intensity in comparison to native OVA in a time-dependent manner (up to day 15). The turbidity measurements determined at 350 nm for different forms of OVA obtained at various time periods also revealed a pattern in concordance with fluorescence intensity measurements thus offering further evidence in support of aggregate formation (Fig. 1A, *b*).

Extended Incubation with Shaking Leads to the Formation of β -Sheet-rich OVA Aggregates—The OVA samples obtained after various incubation periods were assessed for the presence of β -sheets employing Congo Red and ThT binding assays as well as CD spectroscopy. Congo Red, an amyloid binding dye, is used as a tool to monitor the formation of protein aggregates. The β -sheet conformation of amyloids is crucial for Congo Red binding. Congo Red exhibits a red shift in the absorbance spectrum upon binding to the amyloids (7). In the present study, Congo Red was incubated with aggregates obtained at various time points. The aggregates formed at longer incubation periods showed an increase in absorbance along with a slight red shift. Interestingly, a prominent red shift was observed in aggregates obtained upon incubation of protein for 15 days at pH 2.5 indicating conversion of all the secondary structures to β -sheet conformation. Protein aggregates formed at pH 7.0 did exhibit augmentation of absorbance at increasing incubations but the red shift in wavelength was lower compared with samples incubated at pH 2.5 (Fig. 1B).

ThT, another dye, exhibits enhanced fluorescence emissions upon binding to β -sheet-rich structures like amyloid aggregates of both fibrillar or non-fibrillar nature (8). The aggregates obtained at various time points were characterized employing the ThT binding assay. In general, the aggregates obtained at increasing incubation periods were found to bind ThT more explicitly (Fig. 1C). The aggregates obtained for pH 2.5 samples exhibited significantly enhanced bound fluorescence as compared with the corresponding aggregates obtained at pH 7.0. Interestingly, aggregate generated at pH 7.0 at the same incubation time period showed only 50% fluorescence of that observed for the pH 2.5 sample. The data suggest the formation of β -sheet-rich aggregates for both pH 2.5 and 7.0. However, the greater ThT binding exhibited by aggregated protein generated at pH 2.5 compared with pH 7.0 samples reflects that the fibrillar form for pH 2.5 aggregates to possibly appear earlier than the corresponding pH 7.0 aggregates (Fig. 1C). ThT binding with OVA aggregates was also observed using fluorescence microscopy. In concordance with ThT fluorescence spectral studies, fluorescence microscopy also revealed a similar pattern, *i.e.* aggregates obtained at longer incubations (both at acidic as well as neutral pH) exhibited increased fluorescence (Fig. 2A). ThT and Congo Red binding assays suggest that samples agitated for longer periods (either at pH 2.5 or at 7.0) harbor more β -rich structures than aggregates obtained at shorter incubations.

The far-UV CD spectrum of a protein is highly sensitive to its conformation. In fact, it is especially useful for offering

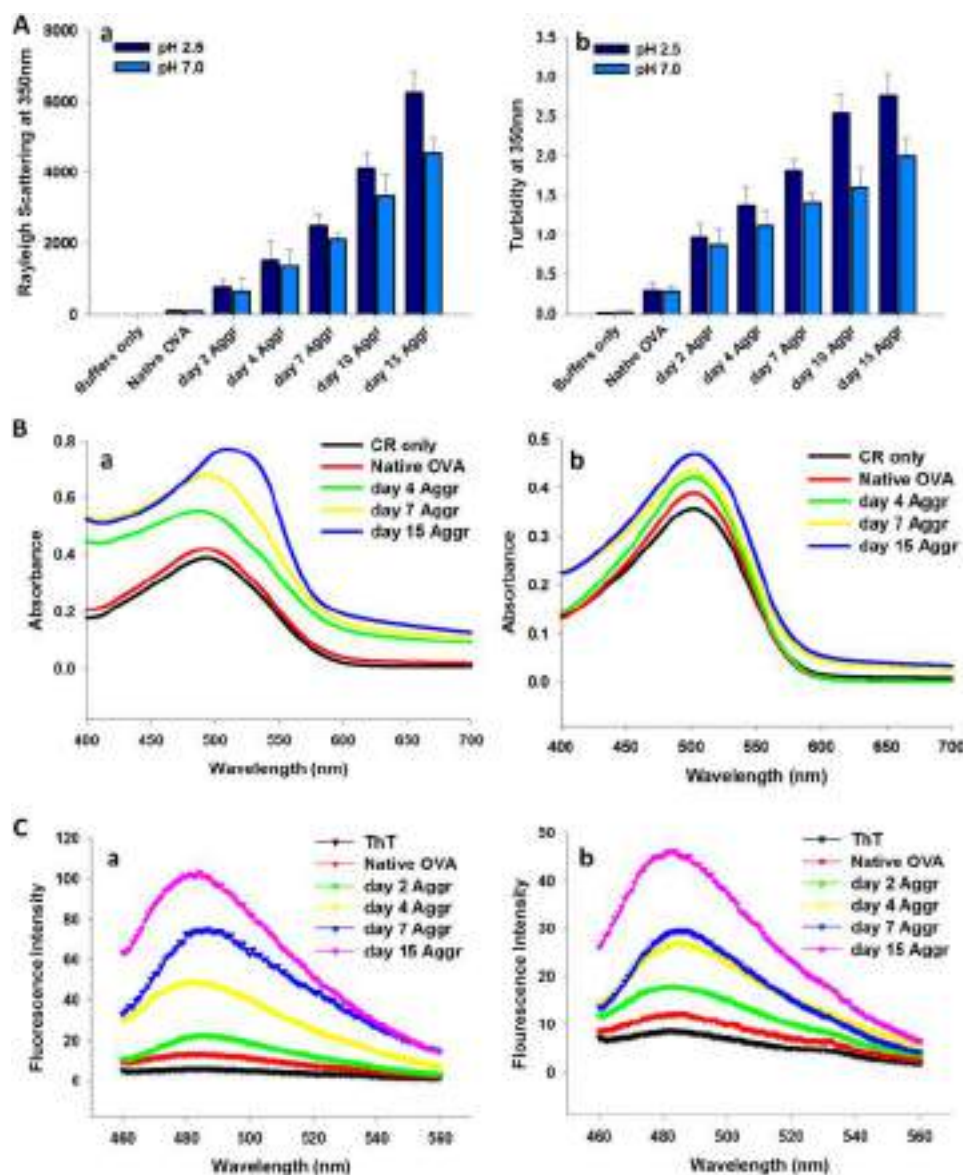


FIGURE 1. Continuous agitation for extended time periods induces aggregation of soluble OVA. A, Rayleigh scattering measurements at 350 nm for aggregates formed at various time points in both acidic and neutral ambiances (a). Turbidity measurements for OVA aggregates formed at various time points at pH 2.5 and 7.0 (b). Error bars exhibit standard error of three independent experiments. B, steady state absorption spectra of Congo Red bound to various aggregates obtained at pH 2.5 (a) and 7.0 (b). The aggregates were scanned in the 400–700 nm range. C, ThT binding assay of various OVA aggregates formed at pH 2.5 (a) and 7.0 (b). ThT emission spectra were obtained by excitation at 450 nm and emission in the range of 460–560 nm. Data are representative of at least three independent experiments with similar observations.

insight regarding the secondary structure of a protein. Fig. 2B highlights shaking induced conformational changes in the structure of OVA. Native OVA exhibited two minima, one at 208 nm and another at 222 nm, which is indicative of a α -helical structure. With an increase in shaking time, the negative peak at 208 nm began to disappear, whereas the peak at 222 nm started shifting toward the left to lie between 215 and 222 nm, which indicates loss of the α -helical structure with the appearance of β -sheets. The aggregates formed at both acidic as well as neutral pH conditions exhibited two negative peaks although the negative ellipticity was decreased in comparison to native OVA. A marked difference for pH 2.5 and 7.0 samples was observed upon further incubations. The aggregate obtained on day 4 (pH 2.5) exhibited a significant loss in negative ellipticity at 208 nm and the

minimum at 222 nm shifted so as to lie between 222 and 215 nm. On the other hand, the protein aggregate generated at the same time period upon incubation at pH 7.0 did not exhibit a significant change when compared with the pH 2.5 sample (Fig. 2B). Day 7 sample, formed upon incubation at pH 7.0, exhibited CD spectrum very similar to that obtained for the day 4 aggregate (pH 2.5) showing almost the same degree of loss in ellipticity at 208 and 222 nm peaks. Interestingly, day 7 aggregate obtained at pH 2.5 exhibited a CD spectrum with a different pattern than its pH 7.0 counterpart, which matched with the spectrum obtained for the day 10 aggregate formed at pH 7.0. These aggregates exhibited a much higher loss in negative ellipticity at 208 nm than the aggregates formed earlier and also showed a shift in the 222 nm peak toward 215 nm. Similar results were obtained for

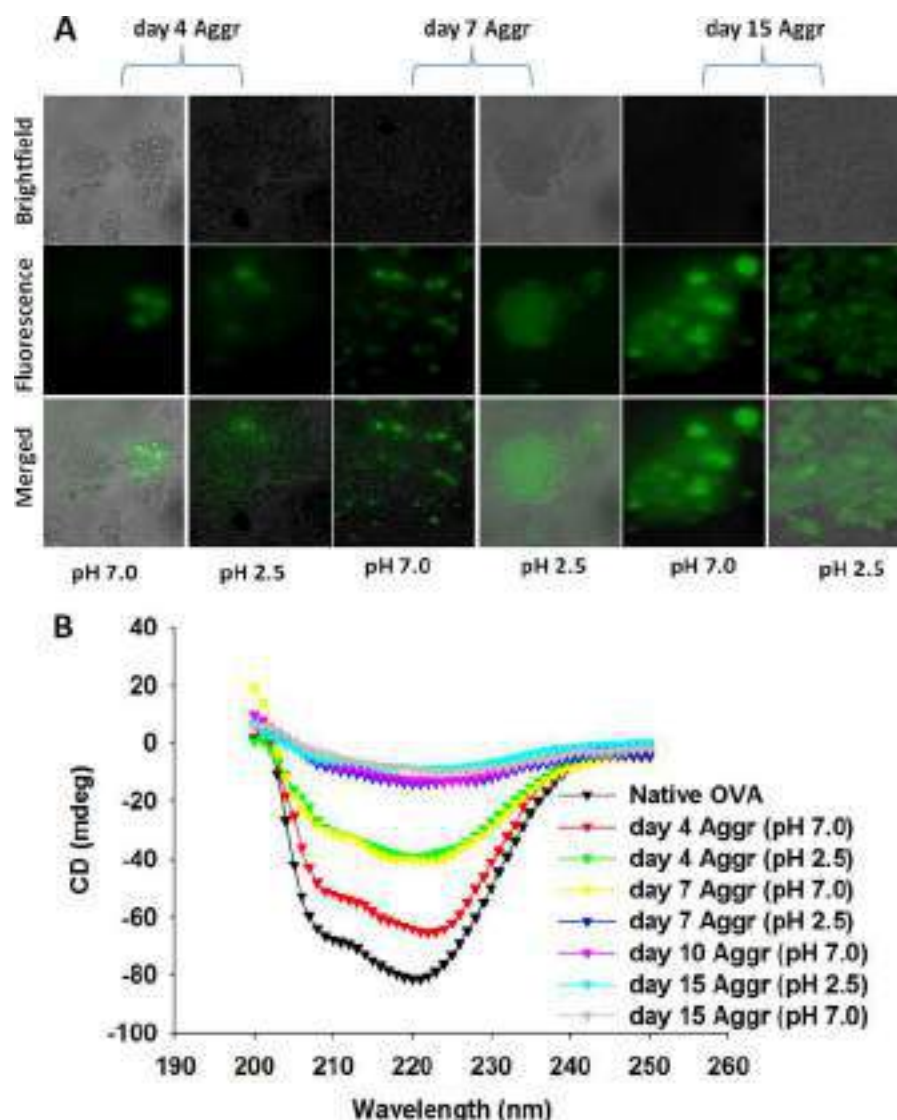


FIGURE 2. Extended shaking of soluble OVA leads to formation of β -sheet-rich aggregates. *A*, ThT binding to various OVA aggregates (100 μ g) as revealed by fluorescence microscopy. ThT (30 μ M) was incubated with OVA aggregates for 30 min; 5 μ l of the suspension was placed onto the glass slide and observed under fluorescence microscope. *B*, secondary structure determination of various OVA aggregates by far UV-CD. Native OVA and various aggregates (200 μ g/ml) were scanned in the range of 200–250 nm. Data are representative of at least three independent experiments with similar observations.

day 15 aggregates formed at both pH 2.5 and 7.0 with almost complete loss in 208 nm minima and a major shift toward 215 nm indicating the presence of only β -sheets, a structural feature of fibrillar amyloids (Fig. 2B).

Aggregates Formed at pH 7.0 Have Fibrillar whereas Aggregate Species Generated at pH 2.5 Have Suprafibrillar Morphology— The morphology of aggregates formed after various incubation periods at various pH conditions was elucidated employing electron microscopy. As shown in Fig. 3, aggregates obtained upon shaking at different pH conditions acquired varied morphologies after the same incubation periods. Fibrillar structures resembling typical amyloid fibrils appeared on day 10 postincubation for OVA incubated at pH 2.5 (Fig. 3A), whereas incubation at pH 7.0 ensued in amyloid fibril formation only after 15 days of incubation. In contrast, incubation of OVA at pH 2.5 revealed a branched suprafibrillar structure on day 15 postincubation (Fig. 3A).

The Sturdy Fibrillar Amyloids Release OVA in a Sustained Manner— The release of precursor OVA from its aggregates (formed at pH 2.5 and 7.0) was monitored over an extended time period (Fig. 3B). The protein aggregates (formed at pH 2.5 or 7.0) are found to release OVA in a time-dependent manner. The protein aggregates generated at pH 7.0 exhibited better release than the corresponding pH 2.5 aggregates. Release kinetics of various aggregates was monitored for a total of 15 days (Fig. 3B). Aggregates generated on day 2 of incubation (at pH 2.5 and 7.0) showed a burst release for the initial 3 to 4 days that leveled off subsequently. The aggregates formed at day 4 (for both pH 2.5 and 7.0) were found to release the precursor OVA in a steady manner that peaked at day 12 (for pH 2.5) and 10 (for pH 7.0) and plateaued at day 15. Aggregates generated upon 7 days of incubation exhibited varied release kinetics, the one formed at pH 2.5 could only feebly release OVA in contrast to the day 7 aggregate generated at pH 7.0, which exhibited a

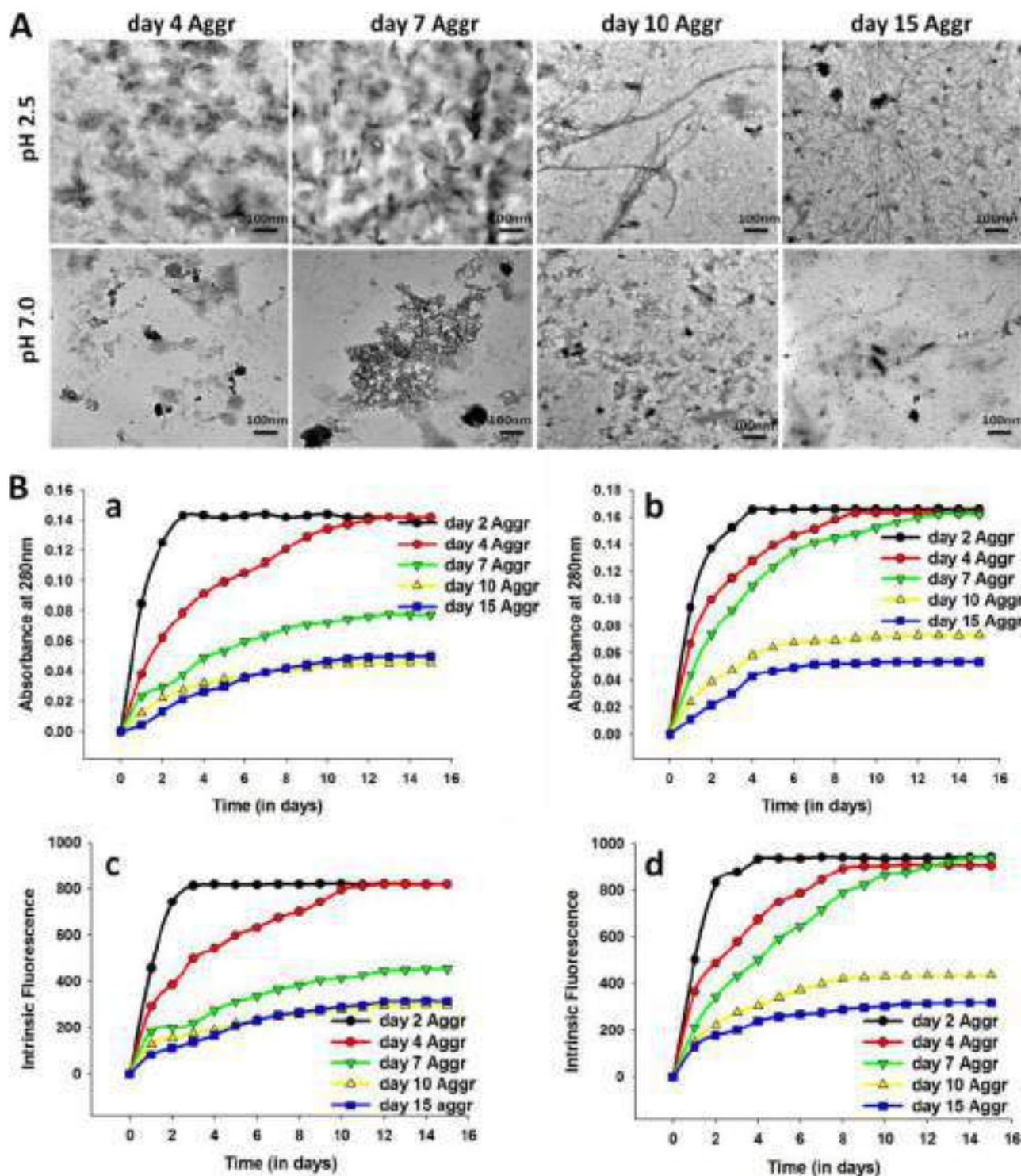


FIGURE 3. *A*, fibril maturation as revealed by transmission electron microscopy. Various aggregates (100 μ g) were coated onto the grid. Images shown are those selected after similar observation of at least two independent experiments performed for each sample. *B*, kinetics of OVA release from various OVA aggregates. *In vitro* release kinetics of OVA from various OVA aggregates obtained at pH 2.5 (*a*) and 7.0 (*b*) for a period of 15 days as measured by determining absorbance at 280 nm. Kinetics of OVA release from various OVA aggregates generated at acidic (*c*) and neutral (*d*) pH as monitored by measuring intrinsic fluorescence with excitation at 280 nm and emission in the range of 300–400 nm. Data are representative of three independent experiments with similar observations.

slow and sustained release that reached plateau after 13 days. The aggregates obtained upon 10 and 15 days of incubation at pH 2.5 or 7.0 were also observed to release OVA. Hence, both fibrillar as well as suprafibrillar forms of OVA were found to release the protein.

With an increase in the protein concentration in a given sample, its intrinsic fluorescence increases because of the increased number of Trp and Tyr residues. Therefore, we also monitored the intrinsic fluorescence of the protein released in the surrounding milieu (PB, pH 7.4). The intrinsic fluorescence profile

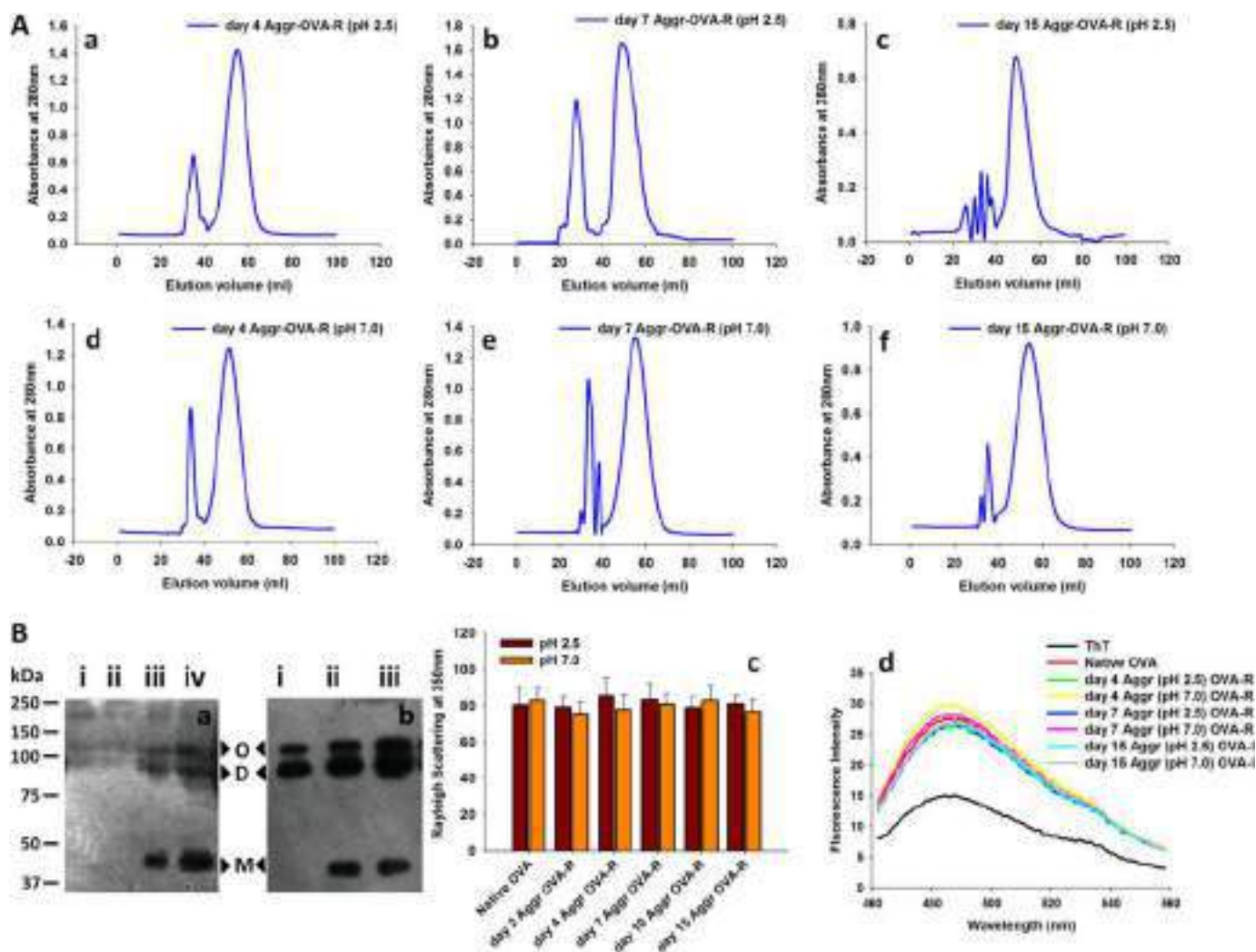


FIGURE 4. Besides oligomeric forms, aggregates release monomeric OVA that exhibit biophysical characteristics similar to that of native OVA. A, size exclusion chromatography of released OVA. Size exclusion profile of OVA released after 12 days of incubation from various aggregates exhibiting release of oligomers, dimers in addition to monomers. a–f, show SEC profile of OVA released after 12 days of incubation from day 4 aggregate formed at pH 2.5, day 7 aggregate formed at pH 2.5, day 15 aggregate formed at pH 2.5, day 4 aggregate formed at pH 7.0, day 7 aggregate formed at pH 7.0, and day 15 aggregate formed at pH 7.0, respectively. B, Western blot analysis and biophysical characteristics of released OVA. Probing with OVA specific polyclonal and 3G2E1D9 monoclonal antibodies reveals the presence of monomeric, dimeric, as well as oligomeric OVA released from OVA aggregates in surrounding milieu. a, immunoblot of OVA released from day 7 aggregate formed at pH 7, developed using anti-OVA polyclonal antibody; lanes i–iv exhibit OVA released after 4, 8, 12, and 15 days, respectively, from the day 7 aggregate. b, OVA released from day 7 aggregate formed at pH 7 probed using anti-OVA 3G2E1D9 monoclonal antibody; lanes i–iii show OVA released post 8, 12, and 15 days of incubation, respectively. M, D, and O denote monomers, dimers, and oligomers respectively. Rayleigh scattering studies (c) and ThT binding assay (d) of the OVA released from various aggregates. OVA-R represents released OVA from various aggregates. Error bars represent S.E. of three independent experiments. At least three independent experiments were carried out for each sample and data obtained with similar results are presented.

of the released OVA for various aggregates was in agreement with those observed for spectrophotometric results. Intrinsic fluorescence of the materials released from day 15 aggregates formed either at pH 2.5 or 7.0 attained a substantial value suggesting release of OVA (Fig. 3B, c and d).

Besides Monomer, the Aggregates Possibly Release Dimeric as Well as Oligomeric Forms of OVA—The elution profile of OVA released after 12 days of incubation from various aggregates is shown in Fig. 4A. In almost all the fractions, peaks are observed in the void volume apart from another fully resolved and distinct peak corresponding to the released monomeric form of protein. The peaks corresponding to the void volume may be dimeric or multimeric forms of released OVA. This indicates that the released fraction of OVA from various aggregates is a mixture of monomeric, dimeric, as well as multimeric OVA

(Fig. 4A). Western blot analysis employing OVA-specific polyclonal and 3G2E1D9 monoclonal antibodies further supported the possible presence of various forms (monomeric/dimeric/oligomeric) of OVA released from aggregates (Fig. 4B, a and b). Immunoblots stained with polyclonal anti-OVA antibody showed OVA release from day 7 aggregate formed at pH 7.0 after 4, 8, 12, and 15 days corresponding to lanes i, ii, iii, and iv, respectively (Fig. 4B, a). Surprisingly, post 4 and 8 days of release, no monomeric band was observed, although bands of higher molecular weight that might be corresponding to dimer or higher oligomeric forms can be seen in Fig. 4B, lanes i and ii. After 12 and 15 days of release, a distinct monomeric band in addition to higher molecular weight proteins can be observed in Fig. 4B, lanes iii and iv. Similarly, Western blot performed using anti-OVA 3G2E1D9 monoclonal antibody shows concordant

result with that obtained for polyclonal antibody (Fig. 4B, *b*). Lanes *i*, *ii*, and *iii* correspond to OVA released after 8, 12, and 15 days, respectively, from day 7 aggregate formed at pH 7. Monomeric as well as higher oligomeric forms of OVA are seen to be present in the released materials after 12 days of release.

The Released OVA Seems to Acquire a Native Configuration and Does Not Exhibit General Characteristics of Amyloid Aggregates—A fixed amount of released OVA from various aggregates (generated at pH 2.5 and 7.0) was analyzed for light scattering at 350 nm. As shown in Fig. 4B, *c*, the protein materials released from various aggregates exhibited light scattering very similar to that of native OVA. Moreover, the released OVA from various aggregates also showed binding to ThT more or less very similar to native OVA (Fig. 4B, *d*).

Antibodies Developed Upon Administration of Aggregated Forms of OVA Can Recognize Native Antigen—The immune response evoked in the host upon immunization with various aggregate forms of OVA was assessed on the basis of ELISA and dot blot assay. First, wells of ELISA plates were coated with various forms of OVA aggregates and were allowed to react with antibodies generated upon immunization with the corresponding aggregate forms. OVA fibrils formed either at pH 2.5 or 7.0 were found to react explicitly with the generated antibodies. Antibodies developed against aggregates formed either at pH 2.5 or 7.0 exhibited very similar reactivities. Dot blot assay results supported the ELISA findings that antibodies reactive to various OVA aggregate forms are formed upon their immunization (Fig. 5A).

Subsequently, the potential of the antibodies to recognize the native form of OVA was assessed. For ELISA, wells of microtiter plates were coated with native OVA and evaluated for its reactivity with antibodies developed against both native as well as various other forms of OVA aggregates. ELISA analysis revealed that antibodies generated against various forms of aggregates (formed both at pH 2.5 or 7.0) could recognize the native form of OVA (Fig. 5B, *a* and *b*). Aggregates generated on day 10 as well as day 15 (at both pH 2.5 and 7.0) were also successful in generation of anti-native OVA antibodies. Interestingly, day 4 aggregate for pH 2.5 as well as days 4 and 7 aggregates for pH 7.0 exhibited better antibody production than the native OVA itself. The specificity of the generated antibodies was further ascertained by dot blot assay. To perform dot blot, native OVA was coated on PVDF strips and its reactivity was checked for antibodies generated against various forms of OVA aggregates (both for pH 2.5 and 7.0 samples) formed at various time points. The antibodies developed upon immunization with both non-fibrillar as well as fibrillar OVA aggregates were found to recognize native OVA (Fig. 5B, *c*).

OVA Released by Various Forms of OVA Aggregates Interacts with Anti-native OVA Antibodies of Monoclonal as Well as Polyclonal Origin—The incubation of fibrils as well as other forms of OVA resulted in the release of precursor OVA into the surrounding milieu. We wondered whether various *in vitro* released species of OVA are reactive to native OVA-specific antibodies (of polyclonal as well as monoclonal origin); to ensure this we performed indirect ELISA and a dot blot assay. For ELISA, we coated the wells with OVA (2 μ g/well) released *in vitro* from each aggregate (both non-fibrillar or fibrillar) and

allowed it to interact with polyclonal anti-native OVA antibodies (which may recognize mature aggregates/fibrils as well). Proteins released from various aggregates generated either at pH 2.5 or 7.0 were found to react with anti-native OVA antibodies (Fig. 5C, *a* and *b*). Next, we performed a dot blot assay by coating the released OVA onto PVDF strips and checked their reactivity with antibodies raised against native OVA as done for ELISA. In concordance with ELISA data, the anti-native OVA antibodies recognized the OVA released from various aggregates (Fig. 5C, *c*).

To work on our hypothesis that the released OVA might be attaining a native conformation, we exploited the 2D11 antibody, which is an anti-OVA mouse monoclonal antibody showing high affinity for OVA in its native form, but is not able to recognize denatured OVA. ELISA as well as dot blot results enumerate the recognition of released OVA from various aggregates with 2D11 antibody (Fig. 5D, *a* and *b*). Native OVA as well as OVA released from various aggregates exhibit practically similar reactivities with 2D11 antibody. Similarly, dot blot data also reveals that 2D11 antibodies recognize both mono as well as oligomeric forms of released OVA. However, 2D11 antibodies fail to recognize the mature aggregates/fibril form of proteins (Fig. 5D, *c*).

Macrophages Phagocytose OVA Aggregates—The sustained release kinetics observed for various OVA aggregates persuaded us to analyze if they can be exploited as vaccine candidates. Because aggregates obtained at day 4 and 7 for pH 2.5 and 7.0, respectively, were found to release OVA in a slow and sustained manner. Therefore, we investigated their uptake by macrophages, which are professional antigen presenting cells. As shown in Fig. 6*a*, a punctuate fluorescence (co-localization with endo-lysosomal compartment) along with a diffuse pattern localized throughout the intracellular compartment of the macrophages is observed.

The OVA Aggregate-based Immunization Evokes Th1 Cytokines in the Host—Th1/Th2 bias was assessed in animals immunized with day 4 and 7 aggregates (formed at pH 7.0 and 2.5). The levels of Th1 cytokines, IL-12 and IFN- γ , were found to be significantly elevated in animals immunized with day 4 (formed at pH 7.0 and pH 2.5) and day 7 (formed at pH 7.0) aggregates in comparison to native OVA ($p < 0.01$) (Fig. 6, *b* and *c*). Although day 7 aggregates formed at pH 2.5 led to the generation of higher levels of Th1 cytokines, the increase was only moderate as compared with native OVA ($p < 0.05$). On the other hand, insignificant levels of Th2 cytokine (IL-4) were induced in the groups immunized with day 4 (generated at pH 7.0 and 2.5) and day 7 aggregates (formed at pH 7.0) (Fig. 6*d*). The day 7 aggregate (generated at pH 2.5) also exhibited generation of moderately lower levels of IL-4 as compared with native OVA, which showed elevated levels of IL-4 in comparison to control (Fig. 6*d*).

We also determined antibody isotype switching by evaluating the OVA aggregate-specific IgG1 and IgG2a response in the serum of immunized animals. Animals immunized with day 4 (formed at pH 2.5 and 7.0) and day 7 (generated at pH 7.0) aggregates showed a significantly higher IgG2a/IgG1 ratio as compared with native OVA ($p < 0.01$). On the other hand, day 7 aggregates formed at pH 2.5 showed only a moderate increase

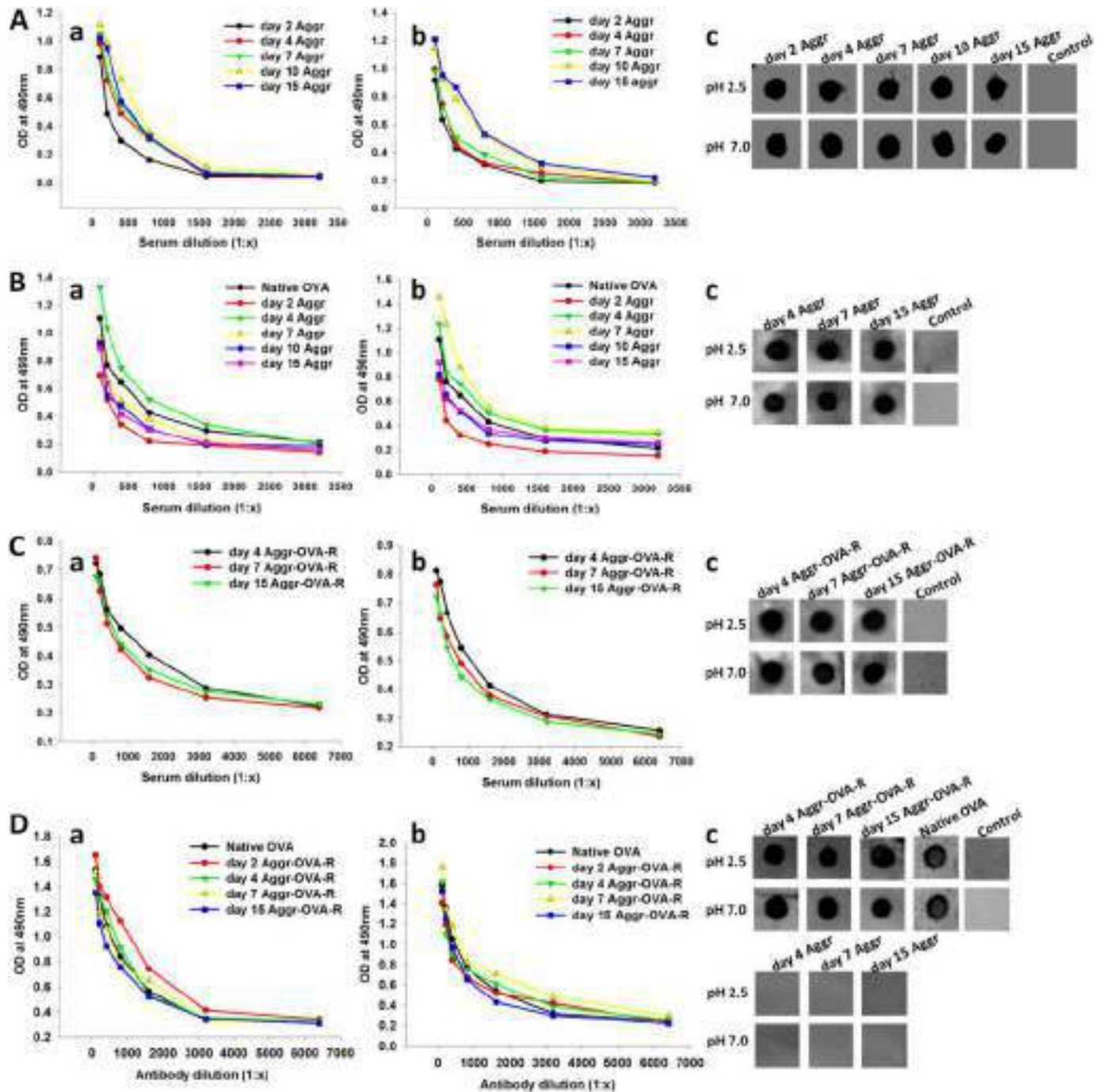


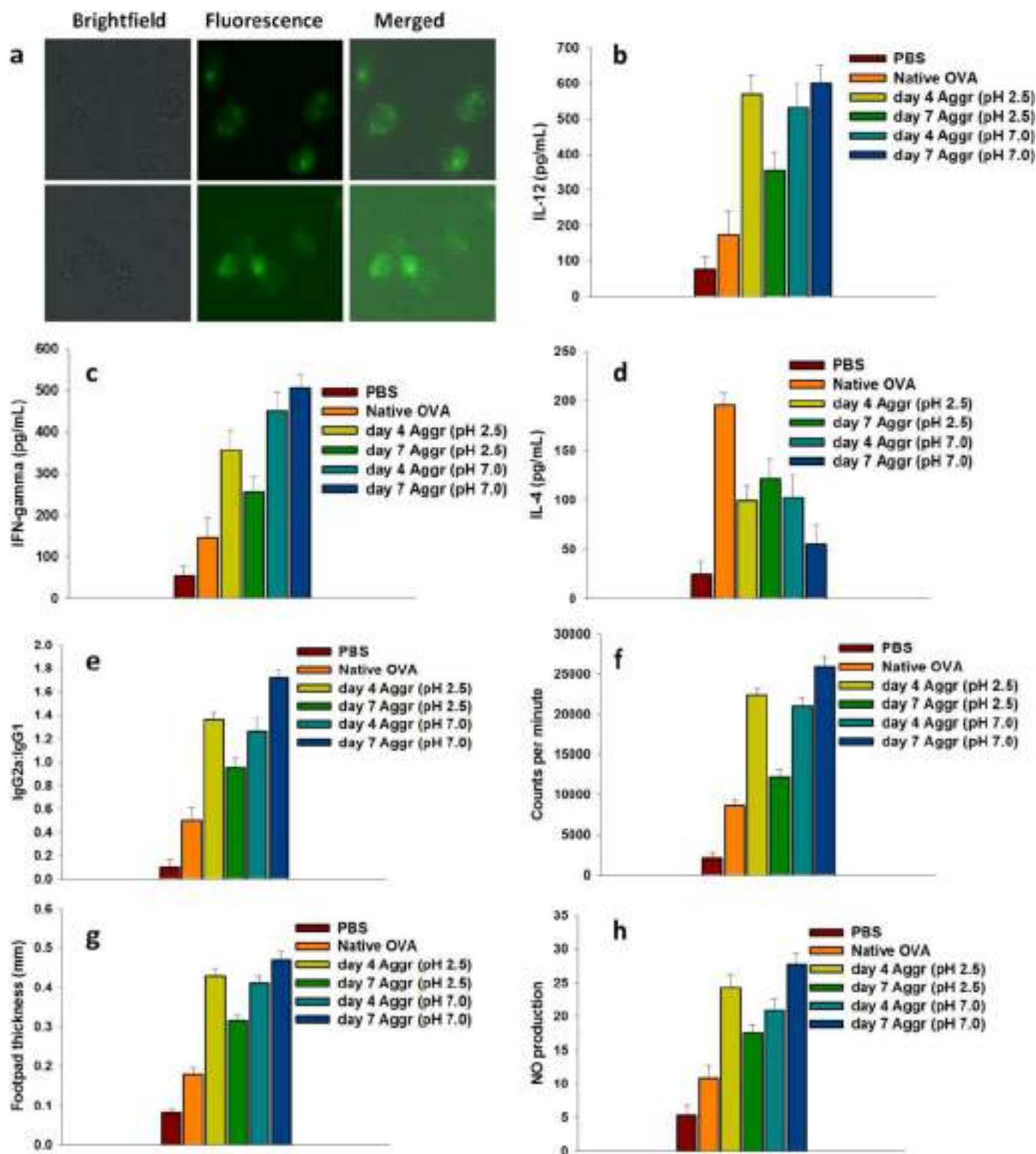
FIGURE 5. A, induction of aggregate-specific antibodies upon immunization with OVA aggregates. OVA aggregates formed at pH 2.5 (a) and 7.0 (b) were allowed to interact with aggregate-specific antibodies employing ELISA. In the next set of experiments, various amyloid aggregates were coated onto PVDF strips and investigated for binding with antibodies generated upon immunization with corresponding aggregates (c). B, OVA aggregate immunization also induces native OVA-specific antibodies. The ELISA plate was coated with native OVA antigen as described under "Experimental Procedures" and reacted with sera obtained from the animals immunized with various aggregates as revealed by dot blot assay (c). C, OVA released from various aggregates interacts with native OVA-specific antibodies. ELISA plate was coated with OVA released from aggregates formed at pH 2.5 (a) and 7.0 (b) and allowed to react with polyclonal antibodies produced in response to immunization with native OVA. For the dot blot assay, OVA released from various amyloid aggregates were coated onto PVDF strips and evaluated for reactivity with anti-native OVA polyclonal antibodies (c). D, OVA released from various amyloid aggregates reacts with 2D11 anti-OVA monoclonal antibody that recognizes only native but not denatured OVA. ELISA plate was coated with OVA released from aggregates formed at pH 2.5 (a) and 7.0 (b) and allowed to react with 2D11 anti-native OVA monoclonal antibodies. OVA released from various amyloid aggregates and amyloid aggregates themselves were coated onto PVDF strips and evaluated for reactivity with anti-native OVA 2D11 monoclonal antibody by dot blot assay (c). 2D11 antibody recognized OVA released from various aggregates as well as native OVA but failed to react with aggregates themselves. For control, a nonspecific protein (human serum albumin) was coated onto the membrane and allowed to react with the respective antibody. OVA-R denotes OVA released from various aggregates. Data are representative of at least three independent experiments carried out for each sample.

Amyloid Immunization Induces Native Antigen-specific Antibodies

in the IgG2a/IgG1 ratio in comparison to native OVA ($p < 0.05$) (Fig. 6e).

T-cell Proliferative Response in Lymphocytes Isolated from Immunized BALB Mice—Lymphocyte proliferation in response to immunization with a prospective candidate vaccine is used as a parameter to assess its vaccine potential. Lymphocytes isolated after 1 week post-booster from the spleens of mice immu-

nized with native OVA as well as day 4 and 7 aggregates formed at both pH 2.5 and 7.0 exhibited proliferation upon their exposure to native OVA (Fig. 6f). The proliferative response of lymphocytes obtained from animals immunized with day 4 (formed at pH 2.5 and 7.0) and day 7 (formed at pH 7.0) aggregates was significantly higher when compared with native OVA ($p < 0.01$), however, day 7 aggregate formed at pH 2.5 showed a



moderately higher T cell proliferation in comparison to native OVA ($p < 0.05$). Graph plots (Fig. 6f) reveal the lymphocyte proliferative response at a fixed dose of OVA (20 μg) at the 1 week post booster time point.

OVA Aggregates Evoke Delayed Type Hypersensitivity in Immunized Animals—To evaluate the ability of various OVA aggregates to induce a cell-mediated immune response, we immunized mice subcutaneously in the lower abdominal region. Native OVA was used as immunogen to determine whether they need an adjuvant for evoking a desirable immune response. Seven days after immunization, mice were exposed to native OVA or PBS via the footpad and footpad swelling was measured at various time intervals. Immunization with day 4 (generated at pH 2.5 and 7.0) and day 7 aggregates formed at pH 7.0 resulted in the generation of a strong DTH response ($p < 0.01$), whereas the day 7 aggregate formed at pH 2.5 resulted in generation of a moderate DTH response ($p < 0.05$) as compared with native OVA (Fig. 6g).

Nitric Oxide Production—Formation of NO is used as an index of the activated macrophage population. One week post booster, generation of NO was evaluated in macrophages isolated from mice immunized with native OVA and day 4 as well as day 7 OVA aggregates. Maximum NO production was observed in macrophages isolated from mice given day 7 aggregate formed at pH 7.0 after 24 h of pulsation ($p < 0.01$), followed by day 4 aggregate generated at pH 2.5 and day 4 aggregate formed at pH 7.0. An augmented NO production in comparison to native OVA was also observed in day 7 aggregate formed at pH 2.5 ($p < 0.05$) but was not as significant as observed for other aggregates (Fig. 6h).

Lymphocyte Proliferative Response in Splenocytes Isolated from TCR-transgenic OT-I and OT-II Mice—To obtain a clear picture about the humoral and cellular immune responses evoked, we also analyzed lymphocyte proliferative response in splenocytes isolated from TCR-transgenic OT-I and OT-II mice that exhibited T cells with TCR specific for OVA Class I and OVA Class II peptides, respectively. Splenocytes isolated from TCR-transgenic OT-I and OT-II mice were treated with native OVA as well as day 4 and 7 OVA aggregates formed at pH 2.5 and 7.0, respectively. As shown in Fig. 7, the proliferative response of OT-I and OT-II splenocytes with day 4 (formed at pH 2.5) and day 7 (formed at pH 7.0) aggregates was significantly higher when compared with native OVA ($p < 0.05$). Day 7 OVA aggregate formed at pH 7.0 also showed a slightly higher

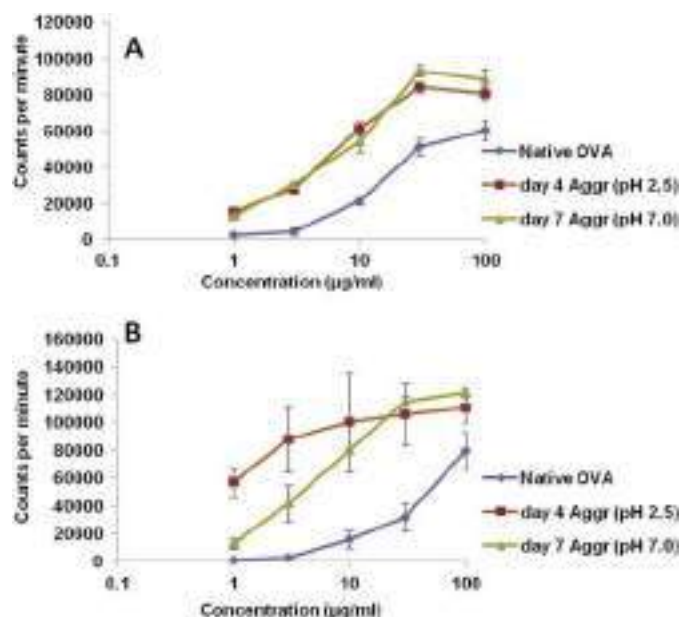


FIGURE 7. Lymphocyte proliferation response in TCR-transgenic OT-I and OT-II lymphocytes upon stimulation with titrating concentrations of various OVA aggregates. T cell proliferation response in TCR-transgenic OT-I (A) and TCR-transgenic OT-II (B) cells when co-cultured in the presence of increasing concentrations (1 to 100 $\mu\text{g/ml}$) of day 4 aggregate formed at pH 2.5 and day 7 aggregate formed at pH 7.0 in 96-well plates. After 60 h of culture, the plates were pulsed with 0.5 $\mu\text{Ci/well}$ of [^3H]thymidine. The radioactivity incorporation was determined at the end of the 72-h incubation in proliferating cells and represented in terms of counts/min values to denote the level of stimulation. Data are expressed as mean \pm S.E. of triplicate cultures. Statistical significance of the data was determined using Student's t test analysis with $p < 0.05$ level of significance. For OT-I as well as OT-II lymphocytes, day 4 aggregate (formed at pH 2.5) versus native OVA, $p < 0.05$; day 7 aggregate (formed at pH 7.0) versus native OVA, $p < 0.05$.

T cell proliferation in comparison to day 4 OVA aggregate formed at pH 2.5.

DISCUSSION

Amyloid fibrils belong to the group of self-assembled ordered nanostructures generated upon improper folding of polypeptides/proteins (2). Although pathogenesis of several human diseases is linked to amyloids, growing evidence indicates that amyloids might be actively participating in several biological events. A few recent reports have elaborated that *in vitro* synthesized amyloids when administered into animals elicit biological functions of native protein (23, 24). Maji *et al.* (23) found that long-acting gonadotrophin releasing hormone analogs are

FIGURE 6. OVA aggregates are taken up by professional antigen presenting cells and also evoke Th1 biased immune response in the immunized animals. a, green fluorescence shows the uptake of day 4 aggregate obtained at pH 2.5 (upper panel) and day 7 aggregate obtained at pH 7.0 (lower panel) by macrophages isolated from thioglycollate-primed BALB/c mice. Data are representative of at least three independent experiments carried out for each sample. OVA aggregates (day 4 and 7 aggregates formed both at pH 2.5 and 7.0) mediated Th1/Th2 bias was ascertained by determining the cytokine response in splenocyte culture supernatant belonging to various immunized groups following the protocol described under "Experimental Procedures," IL-12 (b), IFN- γ (c), and IL-4 (d). To further confirm the Th1/Th2 polarization upon immunization with day 4 and 7 aggregates (generated at pH 2.5 and 7.0), the sera of immunized animals were analyzed for the presence of IgG2a and IgG1 isotype (e). Moreover, OVA aggregates induce strong DTH response, lymphocyte proliferation, and enhanced NO production as revealed by f–h, respectively in BALB/c mice. The DTH response was evaluated by measuring footpad swelling in mice immunized with day 4 aggregate, day 7 aggregate, native OVA, and PBS. The lymphocyte proliferation assay was performed to measure lymphocyte proliferation of OVA-specific T lymphocytes. Lymphocytes isolated from various immunized groups were stimulated with a corresponding set of matching formulations of OVA. The cells were allowed to grow in the presence of [^3H]thymidine as described under "Experimental Procedures." The incorporation of labeled nucleotide during DNA synthesis of proliferating cells was measured and denoted as cpm. NO was determined in macrophages isolated from mice immunized with various aggregates. The data represent mean of three determinants \pm S.D. and are representative of at least three independent experiments with similar observations. Various immunized groups were compared to determine the statistical significance of the data using Student's t test analysis with $p < 0.05$ level of significance. Day 7 aggregate formed at pH 7.0 versus native OVA, $p < 0.01$; day 4 aggregate formed at pH 7.0 versus native OVA, $p < 0.01$; day 7 aggregate formed at pH 2.5 versus native OVA, $p < 0.05$; day 4 aggregate formed at pH 2.5 versus native OVA, $p < 0.01$.

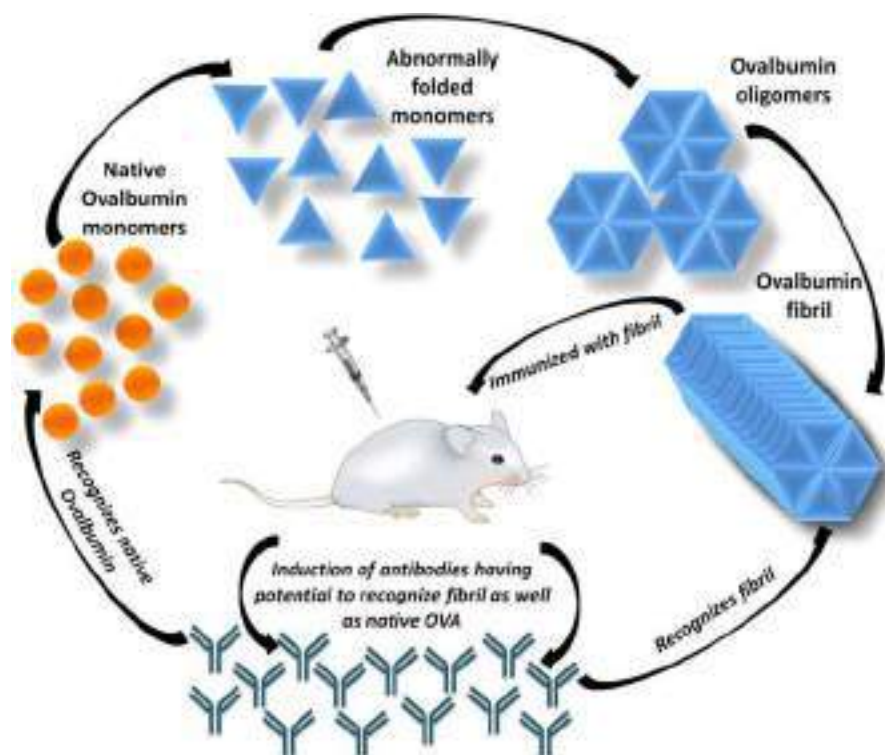


FIGURE 8. Schematic illustration depicting kinetics of fibril formation and potential of OVA aggregates to induce generation of antibodies that have ability to recognize both native as well as fibrillar OVA. The model depicts that formation of fibril from monomeric native OVA encompasses various intermediates such as abnormally folded monomers and oligomers. More specifically, it highlights that fibril immunization leads to generation of antibodies reactive to native as well as fibril OVA.

able to form amyloids *in vitro*, which can sustain the release of monomeric drug, the therapeutic molecule, both *in vitro* and *in vivo*. Similarly, a controlled release of insulin monomers from *in vitro* synthesized pre-fibrillar oligomers made from insulin has also been reported (24), demonstrating them to be a potential therapeutic agent of long-acting peptide drugs. The investigators propose that amyloid fibril or pre-fibril forms can act as depots and possibly release the bioactive form of the peptide/protein in a sustained manner. The bioactivity of the released peptide is realized from the fact that it binds to the specific receptors (*c.f.* gonadotrophin releasing hormone receptor and insulin receptor) for which obviously a perfectly fitting conformation is required to activate the downstream signaling cascade. In these reports, it has been proposed that the amyloid form of protein may release the bioactive peptide retaining the conformational properties of the native state of the peptide. In the present study, in-house synthesized amyloid fibrillar and non-fibrillar aggregates of OVA were injected into mice and the antibodies raised against them were evaluated for their specificity with native form of OVA.

Morphological alterations in amyloids formed from the same protein under differing incubation ambiances are among the most intriguing aspects of amyloid attributes (37). The pH of the surrounding medium has been observed to be one of the most influencing factors on the characteristic morphology and properties of the resulting amyloid fibrils. It has been found that by manipulating pH conditions, whereas keeping other extrinsic factors constant, fibrils of various shapes and sizes of the same protein can be generated (24). In the present study, buffers with three different pH, glycine-HCl (pH 2.5), glycine-

NaOH (pH 10), and PBS (pH 7.0), were used to induce OVA amyloid formation. Although pH 2.5 and 7.0 buffers could induce aggregation upon shaking, pH 10 buffer failed to induce aggregation (data not shown). Acidic ambience was found to induce better protein aggregation than neutral pH conditions (Fig. 1). Interestingly, the amyloid aggregates for OVA obtained at two different buffering conditions exhibited altered properties with respect to content of β -sheet-rich structures and also to the morphological characteristics of formed aggregates (Figs. 1–3).

Moreover, the data presented in Figs. 1–3, in general, clearly reveal that pH 2.5 induces early fibril formation as compared with pH 7.0. This is particularly well demonstrated in Fig. 3A where the day 15 aggregate formed at pH 2.5 shows hugely branched supra-fibrillar assembly in contrast to the pH 7.0 sample revealing two fibrillar threads separately lying over the surface. This might be explained on the premise that at pH 2.5, earlier formed fibrils would further adhered laterally upon longer incubation conditions that eventually led to the formation of suprastructures. The data also suggest that amyloid formation involves a hierarchical process where precursors formed at the initial stages act as a template for the growth of mature fibers that subsequently interact laterally to generate supra-fibrillar structures. A schematic representation of the hierarchical process of fibril formation is outlined in Fig. 8. The two pH conditions, *i.e.* neutral *versus* acidic, seem to induce $\alpha \rightarrow \beta$ transitions in the protein following the same sojourn, however, this transition is more prompt at acidic conditions when compared with neutral pH conditions. It seems that the variations in the electrostatic repulsions or attractions in response to differing

pH conditions may lead to formation of aggregates of varied morphologies. This implicitly suggests that the amyloid fibrils may have the potential to exhibit distinct forms depending on the incubation conditions.

Once it was ascertained that both acidic and neutral pH conditions induce the formation of amyloid aggregates and fibrils of OVA with differing compactness and morphologies, we set about to study their tendency to release OVA, the precursor protein. The day 4 and 7 aggregates formed either at pH 2.5 or 7.0 were found to release OVA over a period of 10–15 days in a sustained manner. Beyond this period, OVA release from the aggregates attained equilibrium. Interestingly, the fibrillar aggregates formed at days 10 and 15 could also release OVA although the release was not much pronounced when compared with aggregates obtained at the day 4 and 7 incubation periods (Fig. 3B). To analyze the state of OVA released from various aggregates, size exclusion chromatography and Western blot analyses of released OVA from various aggregates were performed. As seen in the size exclusion chromatography analysis (Fig. 4A), the released OVA from various aggregates seems to be in the monomeric, dimeric, as well as multimeric states although the monomeric OVA seems to be a dominant species in the mixture for all the samples. As can be seen in Western blot analysis performed using 3G2E1D9 monoclonal as well as polyclonal anti-OVA antibodies, the appearance of monomeric as well as oligomeric forms of the OVA can be detected by day 12 postincubation (Fig. 4B, *a* and *b*). Until day 8, bands corresponding to higher oligomeric forms of OVA can be seen but no monomeric band is observed. Immunoblot studies appear to indicate that release of OVA from various aggregated forms seem to follow a multistep kinetics. It is to be noted that the OVA dimers/oligomers that are released from the aggregates are SDS-insoluble, hence, did not run as a monomer in a reducing SDS gel, which is in concordance with several reports enumerating the formation of SDS-insoluble amyloid fibrils (38–41). This supports the view that the respective species are actually released from amyloid fibrils.

Furthermore, antigen antibody interactions revealed that antibodies generated upon immunization with various aggregates obtained at pH 2.5 or 7.0 could recognize native OVA in addition to aggregate forms (Fig. 5, *A* and *B*). A schematic illustration of the production of antibodies capable of recognizing fibrillar as well as native OVA upon fibril immunization is shown in Fig. 8. Induction of antibodies reactive to native OVA upon immunization with various aggregates suggests that either the fibrils themselves carry native antigen epitopes or the released OVA might be retaining the native epitopes, also both possibilities may happen simultaneously. Interestingly, day 4 aggregate formed at pH 2.5 and both day 4 as well as day 7 aggregates obtained at pH 7.0 exhibited elevated antibody production against native OVA than the sera obtained upon immunization with native antigen (Fig. 5B, *a* and *b*). The observed interaction of OVA with specific polyclonal antibody could be explained on the premise that aggregates may have acted as depots for the slow and sustained release of the antigen, which boosted immune cells over the time to generate antigen-specific antibodies. Moreover, OVA released under simulated conditions *in vitro* (from each aggregate obtained at pH 2.5 and

7.0) was tested for its reactivity with antibodies generated against the native form of OVA. The anti-native OVA polyclonal antibodies recognized the released OVA substantially, indicating possible retention of native epitopes in the released proteins (Fig. 5C). The observation was validated by employing 2D11 monoclonal anti-OVA antibody that specifically recognizes the native form of OVA but not the denatured form. Interestingly, anti-native OVA monoclonal 2D11 antibody recognizes native OVA as well as OVA released from various aggregates but not aggregates themselves (Fig. 5D). It indicates that the 2D11 antibody is specific to an epitope (conformational epitope) exposed in native OVA but inaccessible in aggregated forms. The reactivity of 2D11 antibody with native and released OVA but not to its aggregated form gives an indication that protein when released from aggregates may undergo a conformational change. The released precursor protein seemingly attains the conformation similar to that of native protein leading to the exposure of the epitopes accessible in native form, which, however, may be buried in the aggregated protein. The reactivity of two different OVA-specific monoclonal antibodies (3G2E1D9; capable of recognizing denatured OVA and 2D11; reactive to native OVA only not denatured form) used in the present study clearly demonstrates that OVA aggregates have the potential to release precursor proteins with intact linear as well as conformational epitopes. Biophysical characteristics such as light scattering and ThT binding of released OVA from various aggregates was also found to be very similar to that observed for native OVA (Fig. 4B, *c* and *d*). Moreover, the far UV CD spectra of the proteins released from various aggregates were also found to be similar to the spectrum obtained for native OVA (data not shown). Although these findings suggest that the released OVA possibly refolds to native protein and hence may harbor the conformational properties of the native form of the protein. However, it would be too premature to conclude that the proteins released from amyloids completely refold to the native protein conformation, as from one intact conformational epitope, we cannot declare conformational integrity of the overall structure.

The immune response data of the present study categorizes aggregate form of protein to act as a potential vaccine, whereby, slow release of antigen over extended time periods can elicit desirable immune responses without repeated booster requirements. Because the day 4 and 7 aggregates generated both at pH 2.5 and 7.0 exhibited slow and sustained release of OVA, we analyzed Th1/Th2 bias, lymphocyte proliferation, DTH response, and NO production in animals immunized with these aggregates. Day 4 and 7 aggregates (formed at pH 2.5 and 7.0) were found to induce significantly higher levels of Th1 cytokines as compared with native OVA (Fig. 6). Strong T cell proliferation and heightened DTH response also indicate a polarized bias for the cell-mediated response in animals immunized with OVA aggregates formed at pH 2.5 and 7.0, but not in those immunized with its native form. Moreover, a significantly higher amount of NO was produced by macrophages isolated from mice immunized with OVA aggregates (Fig. 6). Lymphocyte proliferative responses in OT-I and OT-II lymphocytes in response to stimulation with day 4 and 7 OVA aggregates obtained at pH 2.5 and 7.0, respectively (Fig. 7), are found in

concordance with the T cell proliferative responses obtained for lymphocytes isolated from immunized BALB/c mice. This indicates that OVA aggregate forms are successful in evoking both humoral as well as cell-mediated immune responses in the host. As shown in Fig. 6, *b-h*, the most desirable response among various aggregates was observed for day 7 aggregate (formed at pH 7.0) followed by day 4 aggregate (formed at pH 2.5), which was further trailed by day 4 (formed at pH 7.0) and day 7 (formed at pH 2.5) aggregates. The pattern observed appears to be correlated to the release kinetics of OVA from various aggregates because the day 7 aggregate (formed at pH 7.0) exhibited the best release kinetics when compared with other aggregates. It was followed by day 4 aggregate (formed at pH 2.5), which was found to exhibit better release kinetics than day 4 (formed at pH 7.0) and day 7 (formed at pH 2.5) aggregates. The results are consistent with a previous report where it has been demonstrated that the generation of desirable humoral and cellular immune responses is a function of kinetics of antigen delivery (42). Demento *et al.* (42) have shown that OVA despite being a weak immunogen in free form could elicit a strong humoral and cellular immune response when delivered in poly(lactic-co-glycolic acid) nanoparticles. They ruled out the adjuvant properties of encapsulating material, specifically poly(lactic-co-glycolic acid) (a biodegradable and biocompatible polymer). Rather, their findings enumerate that the slow and sustained release of OVA from poly(lactic-co-glycolic acid) nanoparticles led to better humoral and cellular immune responses in contrast to liposomes, which exhibited a burst release of OVA. Interestingly, they also found that sustained antigen release plays a crucial role in shaping a long-lasting effector T cell memory response, which led to effective clearance of *Listeria monocytogenes*, an intracellular pathogen (42).

Besides specific affinity between the TCR-peptide-MHC interface, the phenotype of T lymphocytes generated against a given antigen is generally regulated by its dose, chemical composition, and also by factors such as differential expression of co-stimulatory molecules, presence of adjuvants, cytokine milieu *etc.*, which play important roles in differential Th1/Th2 bias (43–45). Although the potential of OVA aggregates to induce a strong humoral response can have a direct correlation with a sustained release potential, however, a Th1 bias of various observed immunological responses remained intriguing. It seems that preferential uptake of OVA amyloids by macrophages (Fig. 6*a*) because of their particulate nature has some co-relationship with the Th1-biased response as in an earlier study, it has been reported that OVA linked to beads is presented via MHC class I molecules by macrophages approximately 10^4 times more efficiently than soluble OVA (46).

Fig. 9*A* highlights various sequential and conformational B-cell epitopes present in OVA. The various sequential epitopes have been predicted by COBEpro (47), an algorithm dedicated to predicting continuous B-cell epitopes. The conformational B-cell epitopes have been predicted using CBTOPE prediction algorithm (48).

The cell-mediated immunity exhibited by OVA amyloid aggregates can also be in part due to some of the primary sequence stretches that have a strong propensity to form amyloids and simultaneously bear T cell antigenic determinants.

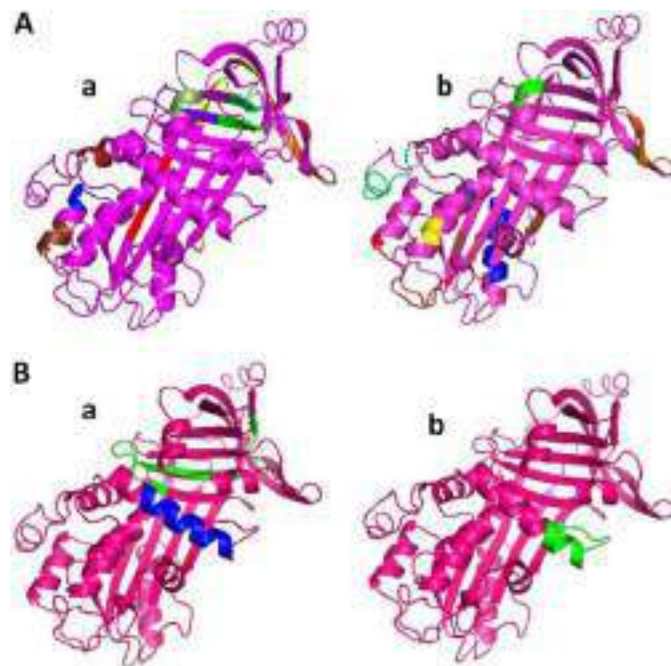


FIGURE 9. *A*, putative B-cell epitopes present in OVA. *a*, various sequential B-cell epitopes present in OVA as retrieved using COBEpro, an algorithm used for predicting continuous B-cell epitopes. Sequences with scores between 0.75 and 0.85 have been presented: ¹¹²PILPEY¹¹⁷ (red), ¹³⁵QTAAQ¹⁴⁰ (blue), ²⁴⁹VSGLEQ²⁵⁴ (green), ²¹⁴GLFRV²¹⁹ (orange), ¹⁹³TQAMPF¹⁹⁸ (yellow), ²³⁴FASGTM²³⁹ (lime green), ¹⁶⁶VDSQTA¹⁷² (brown), ⁹²KPNVDVYS⁹⁸ (firebrick), ²⁷²VMEERK²⁷⁷ (forest), ²⁴⁵LPDEVSG²⁵¹ (purple blue), ²²²MASEKM²²⁷ (olive), and ¹²⁶RGGLEPI¹³². *b*, conformational B-cell epitopes present in OVA as predicted by CBTOPE prediction algorithm: ⁷²QCG⁷⁴ (yellow), ⁸⁰HS⁸¹ (deep blue), ⁸⁶ILN⁸⁸ (lime green), ¹¹⁸LQ¹¹⁹ (raspberry), ¹²¹VKELYRGG¹²⁸ (red), ¹⁵⁴NGIIRNVLPQS¹⁶⁴ (blue), ²⁰³QESKPVMYQ²¹³ (orange), ²¹⁶LF²¹⁷ (forest), ²⁷³MEER²⁷⁶ (green), ²⁹⁶VL²⁹⁷ (chocolate), ³⁰⁸SS³⁰⁹ (olive), and ³²²KISQAVH³²⁸ (firebrick). *B*, three-dimensional ribbon model of OVA illustrating regions of β -aggregation propensity and T-cell antigenic determinants. *a*, β -aggregation propensity regions recognized for OVA: ³²IAIMSALAMVYL⁴³ (blue), ¹⁷²MVLVNAIVFK¹⁸¹ (red), and Phe³⁶⁴-Val³⁸³ (green). *b*, sequence found to be a T-cell epitope (green), ³⁹AMVYLGAkdSTR⁵⁰. The whole OVA sequence was taken into consideration during numbering.

Tanaka *et al.* (49) identified three high β -aggregation propensity regions in OVA using algorithms like TANGO, PASTA, and AGGRESAN: ³²IAIMSALAMVYL⁴³, ¹⁷²MVLVNAIVFK¹⁸¹, and Phe³⁶⁴-Val³⁸³. They further proved by *in vitro* studies that ³⁸LAMVYL⁴³ (a stretch of ³²IAIMSALAMVYL⁴³ sequence) has a very strong tendency to form amyloid fibrils. Interestingly, a sequence, ³⁹AMVYLGAkdSTR⁵⁰, has been attributed to be a T-cell epitope of OVA, which harbors ³⁹AMVYL⁵⁰. The high β -aggregation propensity regions and T-cell epitope of OVA are shown in Fig. 9*B*.

Our results support the hypothesis that amyloid immunization induces native protein-specific immune responses because of the release of precursor proteins from the amyloid depot, which may bear conformational properties of native protein. However, it cannot be ignored that native protein-specific antibodies may also be generated in response to various linear epitopes that remained intact in the fibrils during their formation from precursor proteins. In other words, antibodies specific for linear epitopes of the native protein may cross-react with the fibril form. Nevertheless, our purpose of exploiting amyloid as a vaccine candidate is fulfilled even if the host immune system favors the latter option. It has been reported for

several amyloidogenic proteins to induce the formation of antibodies capable of recognizing both the fibrils as well as the native protein. Antibody HMB50 against the amyloid-forming protein Pmel17 is an example, in that this antibody recognizes fibrils (51) and also efficiently immunoprecipitates newly synthesized native, not yet aggregated protein (52). Many fibril-reactive antibodies additionally recognize SDS-denatured protein. An example would be the Pmel17-specific antibody HMB45 (51). Moreover, aggregation of recombinant epotetin (EPO) has been shown to induce antibodies that bind to native EPO, leading to pure red cell aplasia in subjects (53, 54). It is to be noted that in all the above discussed reports, release of native protein from amyloids has not been studied; nevertheless, the generation of native protein-specific immune responses is well elucidated. Reckoning with these findings, even if we do not take into consideration the release of soluble native protein from the amyloid depot, the presence of intact fibril itself in the system may boost the immune system to elicit a desirable immune response. In fact, amyloids significantly withstand biological proteolytic degradation when compared with the native form of the protein (2, 23, 24), which ensues in extending the residence time of the antigen much longer in circulation. This "stability effect" could strongly enhance its potency as a vaccine even if we ignore release of any precursor protein from amyloid as it may still facilitate the generation of antibodies that may cross-recognize native protein.

CONCLUSIONS

Although the immunoprophylactic responses can always be manipulated by including desirable immunomodulators, the categorical immune response induced in the host upon administration of OVA aggregates suggests that the system can be used as vaccine without inclusion of external excipients. Taking immune activation features into consideration, the self-assembled amyloid bodies can be exploited as potential vaccine candidates against both extra as well as intracellular pathogens.

Acknowledgments—We are thankful to former and present coordinators, IBU, for allowing us to avail the facilities of Institute's Central Instrumentation Facility and also acknowledge the University Sophisticated Instrumentation Facility (USIF) for the transmission electron microscopy micrographs. We are grateful to Dr. Satyajit Rath (National Institute of Immunology, New Delhi, India) for the generous gift of TCR-transgenic OT-I and OT-II mice and also allowing us to use his laboratory facilities for conducting the experiments on the same.

REFERENCES

- Taboada, P., Barbosa, S., Castro, E., and Mosquera, V. (2006) Amyloid fibril formation and other aggregate species formed by human serum albumin association. *J. Phys. Chem. B* **110**, 20733–20736
- Mankar, S., Anoop, A., Sen, S., and Maji, S. K. (2011) Nanomaterials: amyloids reflect their brighter side. *Nano Rev.* **2**, pii:10.3402/nano.v2i0.6032
- Chiti, F., Webster, P., Taddei, N., Clark, A., Stefani, M., Ramponi, G., and Dobson, C. M. (1999) Designing conditions for *in vitro* formation of amyloid protofilaments and fibrils. *Proc. Natl. Acad. Sci. U.S.A.* **96**, 3590–3594
- Dobson, C. M. (2003) Protein folding and misfolding. *Nature* **426**,

- 884–890
- Fändrich, M., and Dobson, C. M. (2002) The behaviour of polyamino acids reveals an inverse side chain effect in amyloid structure formation. *EMBO J.* **21**, 5682–5690
- Sunde, M., and Blake, C. (1997) The structure of amyloid fibrils by electron microscopy and x-ray diffraction. *Adv. Protein Chem.* **50**, 123–159
- Klunk, W. E., Jacob, R. F., and Mason, R. P. (1999) Quantifying amyloid by Congo Red spectral shift assay. *Methods Enzymol.* **309**, 285–305
- LeVine, H. (1999) Quantification of β -sheet amyloid fibril structures with thioflavin T. *Methods Enzymol.* **309**, 274–284
- Rochet, J. C., and Lansbury, P. T., Jr. (2000) Amyloid fibrillogenesis: themes and variations. *Curr. Opin. Struct. Biol.* **10**, 60–68
- Stefani, M., and Dobson, C. M. (2003) Protein aggregation and aggregate toxicity: new insights into protein folding, misfolding diseases and biological evolution. *J. Mol. Med.* **81**, 678–699
- Chiti, F., and Dobson, C. M. (2006) Protein misfolding, functional amyloid, and human disease. *Annu. Rev. Biochem.* **75**, 333–366
- Barnhart, M. M., and Chapman, M. R. (2006) Curli biogenesis and function. *Annu. Rev. Microbiol.* **60**, 131–147
- Iconomidou, V. A., Vriend, G., and Hamodrakas, S. J. (2000) Amyloids protect the silkworm oocyte and embryo. *FEBS Lett.* **479**, 141–145
- Osherovich, L. Z., and Weissman, J. S. (2002) The utility of prions. *Dev. Cell* **2**, 143–151
- True, H. L., and Lindquist, S. L. (2000) A yeast prion provides a mechanism for genetic variation and phenotypic diversity. *Nature* **407**, 477–483
- Maddelein, M. L., Dos Reis, S., Duvezin-Caubet, S., Couly-Salin, B., and Saupe, S. J. (2002) Amyloid aggregates of the HET-s prion protein are infectious. *Proc. Natl. Acad. Sci. U.S.A.* **99**, 7402–7407
- Fowler, D. M., Koulov, A. V., Alory-Jost, C., Marks, M. S., Balch, W. E., and Kelly, J. W. (2006) Functional amyloid formation within mammalian tissue. *PLoS Biol.* **4**, e6.10.1371/journal.pbio.0040006
- Maji, S. K., Perrin, M. H., Sawaya, M. R., Jessberger, S., Vadodaria, K., Rissman, R. A., Singru, P. S., Nilsson, K. P., Simon, R., Schubert, D., Eisenberg, D., Rivier, J., Sawchenko, P., Vale, W., and Riek, R. (2009) Functional amyloids as natural storage of peptide hormones in pituitary secretory granules. *Science* **325**, 328–332
- Wickner, R. B., Edsles, H. K., Roberts, B. T., Baxa, U., Pierce, M. M., Ross, E. D., and Brachmann, A. (2004) Prions: proteins as genes and infectious entities. *Genes Dev.* **18**, 470–485
- Chapman, M. R., Robinson, L. S., Pinkner, J. S., Roth, R., Heuser, J., Hammar, M., Normark, S., and Hultgren, S. J. (2002) Role of *Escherichia coli* curli operons in directing amyloid fiber formation. *Science* **295**, 851–855
- Kelly, J. W., and Balch, W. E. (2003) Amyloid as a natural product. *J. Cell Biol.* **161**, 461–462
- Si, K., Lindquist, S., and Kandel, E. R. (2003) A neuronal isoform of the Aplysia CPEB has prion-like properties. *Cell* **115**, 879–891
- Maji, S. K., Schubert, D., Rivier, C., Lee, S., Rivier, J. E., and Riek, R. (2008) Amyloid as a depot for the formulation of long-acting drugs. *Plos Biol.* **6**, e17.10.1371/journal.pbio.0060017
- Gupta, S., Chattopadhyay, T., Pal Singh, M., and Suroli, A. (2010) Supramolecular insulin assembly II for a sustained treatment of type 1 diabetes mellitus. *Proc. Natl. Acad. Sci. U.S.A.* **107**, 13246–13251
- Kardos, J., Micsonai, A., Pál-Gábor, H., Petrik, É., Gráf, L., Kovács, J., Lee, Y. H., Naiki, H., and Goto, Y. (2011) Reversible heat-induced dissociation of β 2-microglobulin amyloid fibrils. *Biochemistry* **50**, 3211–3220
- Meersman, F., and Dobson, C. M. (2006) Probing the pressure temperature stability of amyloid fibrils provides new insights into their molecular properties. *Biochim. Biophys. Acta* **1764**, 452–460
- Torrent, J., Balny, C., and Lange, R. (2006) High pressure modulates amyloid formation. *Protein Pept. Lett.* **13**, 271–277
- Hirota-Nakaoka, N., Hasegawa, K., Naiki, H., and Goto Y. (2003) Dissolution of β 2-microglobulin amyloid fibrils by dimethyl sulfoxide. *J. Biochem.* **134**, 159–164
- Legge, F. S., Binger, K. J., Griffin, M. D., Howlett, G. J., Scanlon, D., Treutlein, H., and Yarovsky, I. (2009) Effect of oxidation and mutation on the conformational dynamics and fibril assembly of amyloidogenic peptides derived from apolipoprotein C-II. *J. Phys. Chem. B* **113**, 14006–14014
- Binger, K. J., Griffin, M. D., and Howlett, G. J. (2008) Methionine oxidation

- inhibits assembly and promotes disassembly of apolipoprotein C-II amyloid fibrils. *Biochemistry* **47**, 10208–10217
31. Carulla, N., Caddy, G. L., Hall, D. R., Zurdo, J., Gairi, M., Feliz, M., Giral, E., Robinson, C. V., and Dobson C. M. (2005) Molecular recycling within amyloid fibrils. *Nature* **436**, 554–558
32. Binger, K. J., Pham, C. L., Wilson, L. M., Bailey, M. F., Lawrence, L. J., Schuck, P., and Howlett, G. J. (2008) Apolipoprotein C-II amyloid fibrils assemble via a reversible pathway that includes fibril breaking and rejoining. *J. Mol. Biol.* **376**, 1116–1129
33. Ansari, M. A., Zubair, S., Tufail, S., Ahmad, E., Khan, M. R., Quadri, Z., and Owais, M. (2012) Ether lipid vesicle-based antigens impart protection against experimental listeriosis. *Int. J. Nanomedicine* **7**, 2433–2447
34. Ansari, M. A., Zubair, S., Mahmood, A., Gupta, P., Khan, A. A., Gupta, U. D., Arora, A., and Owais, M. (2011) RD antigen based nanovaccine imparts long term protection by inducing memory response against experimental murine tuberculosis. *Plos One* **6**, e22889
35. Chauhan, A., Zubair, S., Tufail, S., Sherwani, A., Sajid, M., Raman, S. C., Azam, A., and Owais, M. (2011) Fungus-mediated biological synthesis of gold nanoparticles: potential in detection of liver cancer. *Int. J. Nanomedicine* **6**, 2305–2319
36. Santiago, P. S., Carvalho, F. A., Domingues, M. M., Carvalho, J. W., Santos, N. C., and Tabak M. (2010) Isoelectric point determination for *Glossoscolex paulistus* extracellular hemoglobin: oligomeric stability in acidic pH and relevance to protein-surfactant interactions. *Langmuir* **26**, 9794–9801
37. Yamaguchi, K., Kamatari, Y. O., Fukuoka, M., Miyaji, R., and Kuwata, K. (2013) Nearly reversible conformational change of amyloid fibrils as revealed by pH-jump experiments. *Biochemistry* **52**, 6797–6806
38. Castaño, E. M., Ghiso, J., Prelli, F., Gorevic, P. D., Migheli, A., and Frangione, B. (1986) *In vitro* formation of amyloid fibrils from two synthetic peptides of different lengths homologous to Alzheimer's disease β -protein. *Biochem. Biophys. Res. Commun.* **141**, 782–789
39. Kawarabayashi, T., Shoji, M., Younkin, L. H., Wen-Lang, L., Dickson, D. W., Murakami, T., Matsubara, E., Abe, K., Ashe, K. H., and Younkin, S. G. (2004) Dimeric amyloid-protein rapidly accumulates in lipid rafts followed by apolipoprotein E and phosphorylated Tau accumulation in the Tg2576 mouse model of Alzheimer's disease. *J. Neurosci.* **24**, 3801–3809
40. Bieschke, J., Russ, J., Friedrich, R. P., Ehrnhoefer, D. E., Wobst, H., Neugebauer, K., and Wanker, E. E. (2010) EGCG remodels mature α -synuclein and amyloid- β fibrils and reduces cellular toxicity. *Proc. Natl. Acad. Sci. U.S.A.* **107**, 7710–7715
41. Bieschke, J., Herbst, M., Wiglenda, T., Friedrich, R. P., Boeddrich, A., Schiele, F., Kleckers, D., Lopez del Amo, J. M., Grüning, B. A., Wang, Q., Schmidt, M. R., Lurz, R., Anwyll, R., Schnoegl, S., Fändrich, M., Frank, R. F., Reif, B., Günther, S., Walsh, D. M., and Wanker, E. E. (2012) Small-molecule conversion of toxic oligomers to nontoxic β -sheet-rich amyloid fibrils. *Nat. Chem. Biol.* **8**, 93–101
42. Demento, S. L., Cui, W., Criscione, J. M., Stern, E., Tulipan, J., Kaech, S. M., and Fahmy, T. M. (2012) Role of sustained antigen release from nanoparticle vaccines in shaping the T cell memory phenotype. *Biomaterials* **33**, 4957–4964
43. Dwivedi, V., Vasco, A., Vedi, S., Dangi, A., Arif, K., Bhattacharya, S. M., and Owais, M. (2009) Adjuvanticity and protective immunity of *Plasmodium yoelii* nigeriensis blood-stage soluble antigens encapsulated in fusogenic liposome. *Vaccine* **27**, 473–482
44. Atif, S. M., Hasan, I., Ahmad, N., Khan, U., and Owais, M. (2006) Fusogenic potential of sperm membrane lipids: nature's wisdom to accomplish targeted gene delivery. *FEBS Lett.* **580**, 2183–2190
45. Ahmad, N., Deeba, F., Faisal, S. M., Khan, A., Agrewala, J. N., Dwivedi, V., and Owais, M. (2006) Role of fusogenic non-PC liposomes in elicitation of protective immune response against experimental murine salmonellosis. *Biochimie* **88**, 1391–1400
46. Kovacsos-Bankowski, M., Clark, K., Benacerraf, B., and Rock, K. L. (1993) Efficient major histocompatibility complex class I presentation of exogenous antigen upon phagocytosis by macrophages. *Proc. Natl. Acad. Sci. U.S.A.* **90**, 4942–4946
47. Sweredoski, M. J., and Baldi, P. (2009) COBEpro: a novel system for predicting continuous B-cell epitopes. *Protein Eng. Des. Sel.* **22**, 113–120
48. Ansari, H. R., and Raghava, G. P. (2010) Identification of conformational B-cell epitopes in an antigen from its primary sequence. *Immunome Res.* **6**, 1–9
49. Tanaka, N., Morimoto, Y., Noguchi, Y., Tada, T., Waku, T., Kunugi, S., Morii, T., Lee, Y. F., Konno, T., and Takahashi, N. (2011) The mechanism of fibril formation of a non-inhibitory serpin ovalbumin revealed by the identification of amyloidogenic core regions. *J. Biol. Chem.* **286**, 5884–5894
50. Yang, M., and Mine, Y. (2009) Novel T-cell epitopes of ovalbumin in BALB/c mouse: potential for peptide-immunotherapy. *Biochem. Biophys. Res. Commun.* **378**, 203–208
51. Watt, B., van Niel, G., Fowler, D. M., Hurbain, I., Luk, K. C., Stayrook, S. E., Lemmon, M. A., Raposo, G., Shorter, J., Kelly, J. W., and Marks, M. S. (2009) N-terminal domains elicit formation of functional Pmel17 amyloid fibrils. *J. Biol. Chem.* **284**, 35543–35555
52. Harper, D. C., Theos, A. C., Herman, K. E., Tenza, D., Raposo, G., and Marks, M. S. (2008) Premelanosome amyloid-like fibrils are composed of only Golgi-processed forms of Pmel17 that have been proteolytically processed in endosomes. *J. Biol. Chem.* **283**, 2307–2322
53. Casadevall, N., Nataf, J., Viron, B., Kolta, A., Kiladjian, J. J., Martin-Dupont, P., Michaud, P., Papo, T., Ugo, V., Teyssandier, I., Varet, B., and Mayeux, P. (2002) Pure red-cell aplasia and antierythropoietin antibodies in patients treated with recombinant erythropoietin. *N. Engl. J. Med.* **346**, 469–475
54. Locatelli, F., Del Vecchio, L., and Pozzoni, P. (2007) Pure red-cell aplasia “epidemic” mystery completely revealed? *Perit. Dial. Int.* **27**, S303–S307

Amyloid Form of Ovalbumin Evokes Native Antigen-specific Immune Response in the Host: PROSPECTIVE IMMUNO-PROPHYLACTIC POTENTIAL

Saba Tufail, Mohammad Owais, Shadab Kazmi, Renu Balyan, Jasneet Kaur Khalsa, Syed Mohd. Faisal, Mohd. Asif Sherwani, Manzoor Ahmad Gatoo, Mohd. Saad Umar and Swaleha Zubair

J. Biol. Chem. 2015, 290:4131-4148.

doi: 10.1074/jbc.M113.540989 originally published online December 15, 2014

Access the most updated version of this article at doi: [10.1074/jbc.M113.540989](https://doi.org/10.1074/jbc.M113.540989)

Alerts:

- [When this article is cited](#)
- [When a correction for this article is posted](#)

[Click here](#) to choose from all of JBC's e-mail alerts

This article cites 54 references, 15 of which can be accessed free at <http://www.jbc.org/content/290/7/4131.full.html#ref-list-1>

OPEN

Bio-mediated synthesis of 5-FU based nanoparticles employing orange fruit juice: a novel drug delivery system to treat skin fibrosarcoma in model animals

Owais Mohammad¹, Syed Mohd. Faisal¹, Nadeem Ahmad², Mohd. Ahmar Rauf¹, Mohd Saad Umar¹, Anzar Abdul Mujeeb¹, Piyush Pachauri¹, Anees Ahmed³, Mohammad Kashif¹, Mohammad Ajmal⁴ & Swaleha Zubair^{5,6}

Nano-sized drug delivery systems (NDDS) have been widely exploited to achieve targeted delivery of pharmaco-materials. Traditional pharmaceutical approaches, implied in the synthesis of nano-formulations, are obscure owing to the incompatible physico-chemical properties of the core drug as well as some other factors crucial in development of NDDS. Infact, most of the existing methods used in development of NDDS rely on usage of additives or excipients, a special class of chemicals. Barring few exceptions, the usage of synthetic excipients ought to be curtailed because of several associated undesirable features. Such issues necessitate strategies that lead to development of the synthetic excipient free drug delivery system. Plant based extracts have great potential to induce synthesis of nano-sized particles. Considering this fact, here we propose a prototype employing orange fruit juice (OJ) to facilitate bio-mediated synthesis of nano-sized supra-molecular assemblies of 5-fluorouracil (5-FU), a potent anticancer drug. The as-synthesized 5-FU Nanoparticles (NPs) retained the anti-neoplastic efficacy of the parent compound and induced apoptosis in cancer cells. The novel 5-FU NPs formulation demonstrated enhanced efficacy against DMBA induced experimental fibrosarcoma in the mouse model when compared to the micro-sized crystals of parent 5-FU drug.

Recent progression in the field of nanotechnology has made remarkable impact on human health and safety. Several recent reports have described a direct correlation between nanoparticles (NPs) size and higher efficacy of the associated drug^{1,2}. Nanoparticle based drug delivery vehicles have been reported to preferentially accumulate at the site of injury, infection and inflammation, mostly because of endothelial dysfunction and blood vessel fenestration at such locations. The nano-dimensions of the NPs promote their ability to traverse various parts of the body. In general, NPs have tendency to accumulate into liver or spleen (components of reticulo-endothelial system) as well as other vital organs including lungs and brain¹⁻³. Surface modification of NPs with specific ligands such as antibodies as well as aptamers *etc.* can facilitate their homing at desired site inside the host body. Upon gaining access to a specific biological niche, the nano-sized materials tend to interfere with a variety of cellular functions including cell proliferation, cell cycle regulation and various vital metabolic activities, *etc.*

5-Fluorouracil (5-FU), is an anti-metabolite showing broad spectrum anti-cancer activity against solid tumors⁴. Primarily, a pyrimidine analog, 5-FU is a purely 'S-phase' active chemotherapeutic agent (with no activity when cells are in G0 and G1 phase of cell cycle) that acts as a thymidylate synthase inhibitor and thereby interferes with DNA synthesis⁵. However, 5-FU drug has several limitations when used in clinical setting that include its short biological half-life, wide systemic distribution and marked toxic effects on bone marrow⁶. Numerous

¹Interdisciplinary Biotechnology Unit, AMU, Aligarh, India. ²University of Jeddah, Jeddah, Saudi Arabia. ³National Institute of Immunology, New Delhi, India. ⁴Jawaharlal Nehru Medical College, AMU, Aligarh, India. ⁵Present address: Department of Computer Science, AMU, Aligarh, India. ⁶Women's College, AMU, Aligarh, India. Correspondence and requests for materials should be addressed to O.M. (email: owais_lakhnawi@yahoo.com) or S.Z. (email: swalehazubair@yahoo.com)

attempts have been made to reduce 5-FU associated side effects and eventually to enhance its therapeutic potential.

The efficacy of a therapeutic agent depends on its bioavailability that in turn is regulated by pharmacokinetic parameters of the related dosage form. Interestingly, various size associated unique features, associated with NPs of a specific chemotherapeutic agents, offers an extra edge over its free form in exerting a chemotherapeutic effect against a cancer cell population^{7,8}. Unfortunately, in order to develop an effective nanosized delivery system, usage of synthetic excipients; the additives other than active pharmaceutical ingredient of a given drug formulation, is restricted mostly because some of them do possess various detrimental features such as undesirable biodegradability, short plasma half-life, toxicity and activation of host immune response, among others. Moreover, cost related issues of some of the widely used excipients, such as lipids in liposome, also hamper their wider application.

Bio-mediated synthesis of metal and inorganic compound based NPs employing extracts both from single and multi-cellular organisms has been considered as an enticing approach worldwide^{9–11}. Recently available nano-sized drug materials, the so-called self-assembled metal NPs, synthesized by employing plant or microbial extract, have elicited enormous interest in nano-therapeutics^{12–16}. Amazingly, these methods have not been translated into the synthesis of NPs comprising of therapeutically active organic molecules; with the exception of few reports from our group highlighting *Aloe vera* leaf extract mediated fabrication of nano-sized particles or assemblies¹⁷.

It is tempting to speculate that bio-mediated fabrication of 5-FU nano-assemblages employing orange fruit juice (OJ) offers a promising approach in the development of novel class of anticancer drug delivery system. Taking this fact into consideration, we explored OJ for its potential to induce the formation of nano-sized particles from microcrystals of parent 5-FU drug. The crystal habit and size analysis of the as-synthesized 5-FU NPs was characterized by employing transmission electron microscopy (TEM), Nanophox Analyzer, DLS, Zetasizer, and Atomic Force Microscopic studies.

To ascertain slow and sustained release of the parent 5-FU nucleobase, we examined the release kinetics of 5-FU NPs over an extended time period. The anti-cancer potential of as-synthesized 5-FU NPs was established by analyzing the level of various apoptotic markers in both epidermoid cell line (A253) as well as *in vivo* system. Finally, we evaluated the efficacy of as-synthesized 5-FU NPs in treatment of dimethyl-benz- α -anthracene (DMBA) induced fibrosarcoma in BALB/c mice.

Results

Content of orange juice. In the present study, we evaluated the potential of the OJ to facilitate bioconversion of 5-FU micro-sized crystals, into nano-sized tiny particles. Consistent with our earlier finding involving *Aloe vera* leaf extract mediated synthesis of NPs^{17,18}, we found that incubation of 5-FU with OJ leads to the bio-mediated synthesis of 5-FU NPs. Data of the present study establish that newly formed NPs can inhibit cancer cells both *in vitro* as well as in model animals more efficiently when compared to the microcrystals of parent 5-FU drug. The detailed description of the orange juice ingredients and its other constituents is represented in Table. 1 and in Supplementary Figs S2 and S3.

Physico-chemical properties of 5-FU NPs. Figure. 1 illustrates characterization of the synthesized 5-FU NPs. The TEM picture reveals formation of isomorphic hexagonal 5-FU NPs (Fig. 1a and Supplementary Fig. S1c). HRTEM image further highlights the hexagonal shape and size of the formed NPs (inset Fig. 1a). In contrast to role of reducing agents as well as other protein constituents to facilitate synthesis of metal nanoparticle, the obscure composition of OJ complicates the analysis and identification of active species that are responsible for nucleation and growth of organic molecules based NPs. While it is not clear what forces drive the formation of 5-FU based NPs, nevertheless, preliminary studies suggest that particle formation is a result of coalescence of core drug nuclei leading to particle growth. Earlier reports propose that low molecular weight hydrophilic constituents of plants were responsible for bio-mediated synthesis of metal NPs^{16,18}. In order to determine the role of low molecular weight compounds in inducing 5-FU NPs formation, the OJ was dialyzed through a 3 kDa cut off dialysis membrane. We found that the dialyzed extract lost its potential to induce NP synthesis.

We next ruled out nucleic acid or protein-based substances present in OJ for their putative role in NP formation. For this, OJ was treated with Proteinase K, DNase or RNase prior to its use in synthesis of 5-FU NPs. It was observed that the above specified treatment does not affect the ability of the OJ to facilitate the synthesis of 5-FU NPs (Fig. 1). To further rule out involvement of other protein based components, we precipitated the OJ with 80% ammonium sulfate and found that the supernatant left after complete precipitation was still efficient in facilitating 5-FU NP formation (data not shown). We also found that boiling of the OJ for 15 minutes did not alter its potential to form 5-FU NPs, which yet again indirectly rules out the involvement of protein based materials in induction of NPs formation.

In concordance with TEM analysis, particle size determinations employing Nanophox further confirmed the size of 5-FU NPs to be around 30 nm as evident from the single prominent peak in Figure 1b. The size distribution profile, as determined by Dynamic light scattering (DLS), also revealed that the NPs have an average size of 30 ± 5 nm as shown in Fig. 1c. Upon incubation of 5 ml of 10^{-3} M 5-FU with 5 ml of 30% w/v of OJ stock (stock solution: 30 g pulp in 100 ml of water) of OJ showed spontaneous synthesis of 5-FU NPs. The synthesis of a myriad of hexagonal shaped NPs was observed in 2D AFM microscopy as shown in Fig. 1d and Supplementary Fig. S1d. The 3D AFM image of as-synthesized 5-FU NPs has been depicted in the Supplementary File (Fig. S1e). All the employed studies unequivocally established size dimensions of the synthesized particles in the range of 25–35 nm. Zeta potential of the 5-FU NPs was found to be around -39.6 ± 2.10 mV as revealed by Zetasizer Nano potential analyzer. The high negative zeta potential value conferred stability to NPs and prevents their aggregation (Fig. 1e).

Ingredients of Orange Juice	Activity	Target and Mechanism of action
Naringenin	Anti-inflammatory	Down regulated ROS production by effecting the NF- κ B via EGFR-PI3K-Akt/ERK MAP Kinase signalling pathway ⁴⁷ .
Hesperetin	Anti-carcinogenic	Induced cytotoxicity in various cancers by down-regulating Bcl-2 expression and enhanced expression of Bax and Caspase-3 ⁴⁸ .
Hydroxycinnamic acid derivatives (Flavones)	Anti-oxidant	They have a potent free radical scavenger ability ⁴⁰ .
D-Limonene (Limonoids)	Anti-proliferative	Suppressed Bcl-2 expression level, upregulated Bax level while caspase-9 was activated and inhibited the Akt activation via intrinsic mitochondrial apoptosis signaling pathway ⁴⁹ .
Ascorbic acid (Vit C)	Anti-oxidant	Highly antioxidant power to recycle vitamin E in membrane and lipoprotein lipid peroxidation ⁵⁰ .
Coumarins and Bioactive amines	Anti-carcinogenic and anti-thrombotic activities	Effect various pathways leading to cancer development such as kinase inhibition, cell cycle arrest, telomerase inhibition, antimitotic activity, carbonic anhydrase inhibition ⁵¹ .
Folate	DNA synthesis, repair and methylation	It modulates the risk of developing cancer in various tissues ⁵² .

Table 1. Various constituents of Orange Juice and its effects on the progression of cancer.

Release kinetics of 5-FU NPs. To establish that 5-FU NPs can work as a depot system of the parent drug, we performed a release kinetic study. The release kinetics data indicate stability of the NPs under various experimental conditions. We found that NPs endure their entity for a time period of more than 120 hours and released approx., 60% of the total drug in PBS as well as Histidine medium. Around 40% of the original drug was released in the surrounding medium when 5-FU NPs were co-incubated with serum (Fig. 2a).

FT-IR spectra of 5-FU NPs. The IR spectrum of an organic molecule deciphers its chemical entity in terms of various functional groups present. The IR spectra of 5-FU NPs showed characteristic peaks of the parent drug (Fig. 2b). The spectral region ranging from 400–600 showed bending of ring halogen bonds in aromatic fluoro compounds, a characteristic peak of fluoro group. The peaks at 1100 to 1700 cm^{-1} represented the stretching vibrations of the C=O, –COO–, –CN and C=C functional groups. There was an increase in the band width in the range 3300–3500 cm^{-1} , characteristic for hydrogen-bonded molecules (–OH••••HO–). The formation of molecular pores in the as-synthesized 5-FU NPs could be related to the influence of the hydroxyl groups, where corresponding bands appear in the region of deformational vibrations of the C–O bond. The bands in the range of 1450–1100 cm^{-1} are associated with stretching vibrations (deformation of C–O and C–O–C bonds) as well as C–H vibrations.

The FTIR spectrum of 5-FU nanoparticle exhibits characteristics peaks that correspond well to the peaks of parent pure 5-FU micro-crystals of drug except for minor differences that can be correlated with local environment or ambiance generated upon formation of the nanoparticle. The splitting of the peak increases in the nanoparticle spectrum when compared to pure 5-FU micro-crystals. This is because of the orange juice ingredient might have interacted with parent 5-FU molecules during the formation/synthesis of the nano-particulate form of the 5-FU drug. An enhancement in the intensity of the peak in the nanoparticle as compared to pure 5-FU micro-crystals is again an indication of the incorporation of orange juice ingredients into the nanoparticle. The FTIR spectrum of 5-FU nanoparticle showed the presence of a peak at $\sim 740 \text{ cm}^{-1}$ corresponding to the C–H out of plane vibration of CF=CH in addition to the peaks observed for the nanoparticle. An enhancement in the intensity of the N–H bending at $\sim 1655 \text{ cm}^{-1}$ and a shift of the O–H and N–H stretching and a shift from $\sim 3400 \text{ cm}^{-1}$ to $\sim 3456 \text{ cm}^{-1}$ is observed. All these observations confirm the presence of active component 5-FU in as-synthesized nanoparticles.

XRD pattern and DSC analysis of 5-FU NPs. Figure 2c shows X-ray diffraction (XRD) patterns of both microcrystals as well as NP form of 5-FU. All the observed diffraction peaks can be indexed using standard data, which exhibits clear crystalline nature of as-synthesized NPs. Moreover, no impurity peaks were detected in the pattern of both forms of the drug, which suggest the high phase purity of the samples. The 2θ value of the most intense peak has been observed at $\sim 37^\circ$.

Differential Scanning Calorimetry (DSC) is a thermoanalytical technique where the difference, between the amounts of heat required to increase the temperature of a sample and reference, is measured as a function of temperature and time^{19,20}. Differential scanning calorimetry technique has been used previously for determination of crystallinity, purity, degradation and/or presence of drug in various pharmaceutical formulations as well^{19,20}. The DSC thermogram suggests that microcrystals of precursor 5-FU drug show good thermal stability up to its melting point. DSC thermogram showed characteristic sharp peak of parent 5-FU microcrystal sample at around 235–255 °C with peak maximum at 249 °C (Fig. 2d). The thermogram corresponding to Nano-formulation, depicted two different peaks in the range of 25–130 °C and 240–270 °C with peak maxima at 74 °C (inset Fig. 2d) and 264 °C respectively. The broad peak corresponding to microcrystalline 5-FU changed significantly by $\sim 15^\circ \text{C}$ in as-synthesized NPs. The observed change in thermal behaviour could be attributed to alteration in physical form of 5-FU in as-synthesized NPs. It also suggests higher stability of the formed NPs that may cause release of parent drug in slow and sustained manner.

The observed peak shift in DSC thermogram indicates that it requires a great amount of energy to break crystal structure of synthesized NPs when compared to microcrystals of parent 5-FU drug. Overall thermal analysis study suggests that the formed NPs are consisted of 5-FU mainly. The emergence of extra peak in thermogram suggests entanglement of 5-FU molecules associated with some putative components of OJ in the formed NPs²¹.

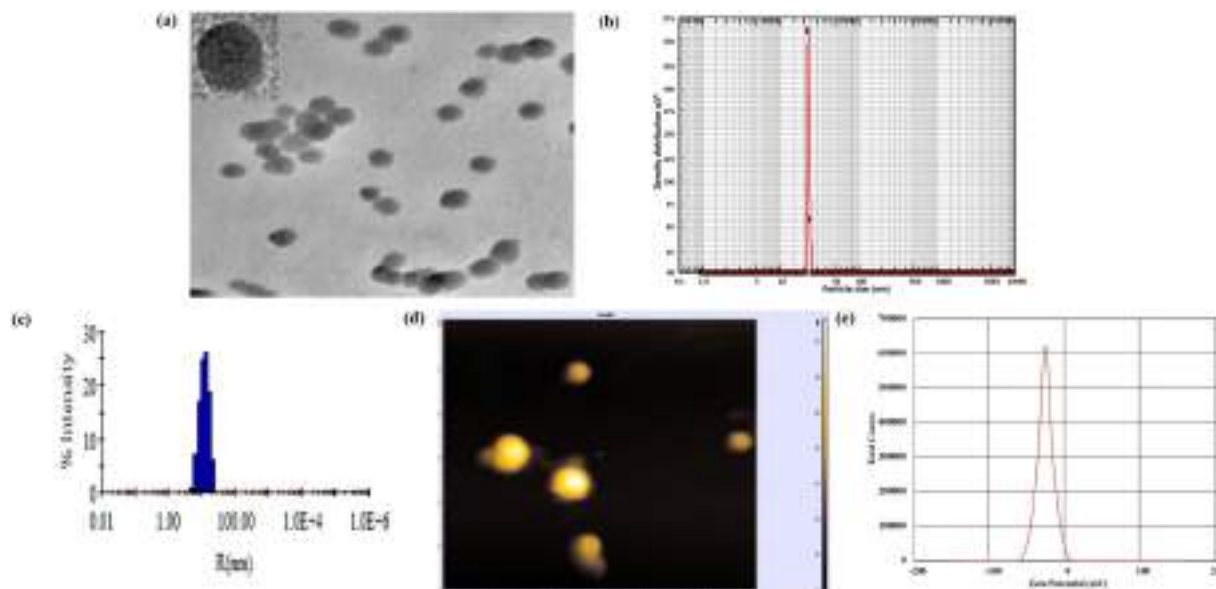


Figure 1. Characterization of 5-FU NPs employing TEM, HRTEM, Nanophox Particle Sizing, DLS, AFM and Zeta-potential analyses. **(a)** TEM analysis of 5-FU NPs synthesized by incubating 5 ml of 10^{-3} M 5-FU solution with 5 ml of OJ for 48 h. HRTEM image of the hexagonal 5-FU NPs (inset **1a**). **(b)** Corresponding particle analysis data as obtained by Nanophox particle analyzer, confirmed the average particle size of 5-FU NPs to be around 25 nm as evident from the single prominent peak **(c)** As analysed by Dynamic Light Scattering size distribution profile, the average size of 5-FU NPs was found to be 25 nm **(d)** Representative 2D Image of 5-FU NPs as revealed by Atomic Force Microscopy **(e)** Zeta potential of 5-FU NPs was found to be -39.6 ± 2.10 mV as revealed by Zetasizer analysis. The dialyzed OJ (2 Kd membrane cut off) failed to induce 5-FU nanoparticle formation. Treatment with proteinase, DNase or RNase did not affect potential of OJ to induce 5-FU NPs.

Anticancer potential of as-synthesized 5-FU NPs. 5-FU NPs up-regulate Bax and p53wt expression in skin fibrosarcoma cells. We tried to unravel the pathway responsible for 5-FU NPs mediated modulation of both pro and anti-apoptotic proteins in epidermoid cells. 5-FU NPs significantly up-regulate expression of pro-apoptotic proteins p53 and Bax and down regulate Bcl-2 when compared to the parent drug. The enhanced expression of Bax can be attributed to the 5-FU NP mediated activation of mitochondria dependent apoptotic pathway. Reduction of mitochondrial membrane potential ensues in Cytochrome-C release that in turn leads to caspase activation²². The p53 protein induces expression of various subsets of genes leading to cell cycle arrest^{23,24}. Further, it works as a transcription factor that interacts with a p53-specific DNA consensus sequence, required for the enhanced expression of p21 molecule^{24–26}. The as-synthesized 5-FU NPs modulated both intrinsic as well as extrinsic pathways to induce apoptosis.

After establishing operative apoptotic pathway in epidermoid cancer cell line, next we elucidated anticancer potential of 5-FU NPs against skin fibrosarcoma in animal model. Animals, with established skin fibrosarcoma (DMBA-induced), were randomly divided in to four different groups and treated with various 5-FU formulations. Animals treated with 5-FU NPs demonstrated an elevated expression of p53wt as compared to those treated with the free form of the parent 5-FU drug ($**p < 0.01$) (Fig. 3). Moreover, 5-FU NPs strongly down-regulated expression of p53mut ($p < 0.01$), thereby enhancing apoptosis of cancer cells in model animals. The expression of pro-apoptotic and anti-apoptotic proteins was not significantly altered in control groups (animal groups treated with cream base or OJ), this proposes that regulation of p53mut gene expression is not because of orange fruit juice constituents or the cream base used as a carrier.

Intrinsic pathway mediated release of mitochondrial cytochrome-C switches on caspase9/apoptosome to activate effector caspase-3, which cleaves many of the major constituents of the cell cytoskeleton and is important for the programmed dismantling of vital cellular structures^{27,28}. Considering, caspases are canonically pivotal mediators of apoptosis, we determined the expression level of caspase-9 in various treated groups. Results shown in Fig. 4 demonstrate significantly enhanced expression of caspase-9 in 5-FU NPs treated group as compared to the group that received microcrystals of free 5-FU drug only ($p < 0.01$). There was relatively lower expression of caspase-9 in OJ (alone) as well as cream base only treated control groups. The data suggests that 5-FU NPs demonstrate remarkable efficacy in up-regulation of caspase-9 and facilitating apoptosis of fibrosarcoma in mouse model.

One can argue that cream base used for ease and presentation of as-synthesized 5-FU NPs can alter anticancer potential of the formulation. To rule out this possibility we applied 5-FU NPs suspended in normal saline on the fibrosarcoma harboring animals. We found that 5-FU NPs suspended in normal saline, in a manner similar to 5-FU NPs suspended in cream base, showed same degree of fibrosarcoma regression as well as modulation of various factors viz. p53wt, Bax and Bcl2 in Balb/c mice (Fig. S5).

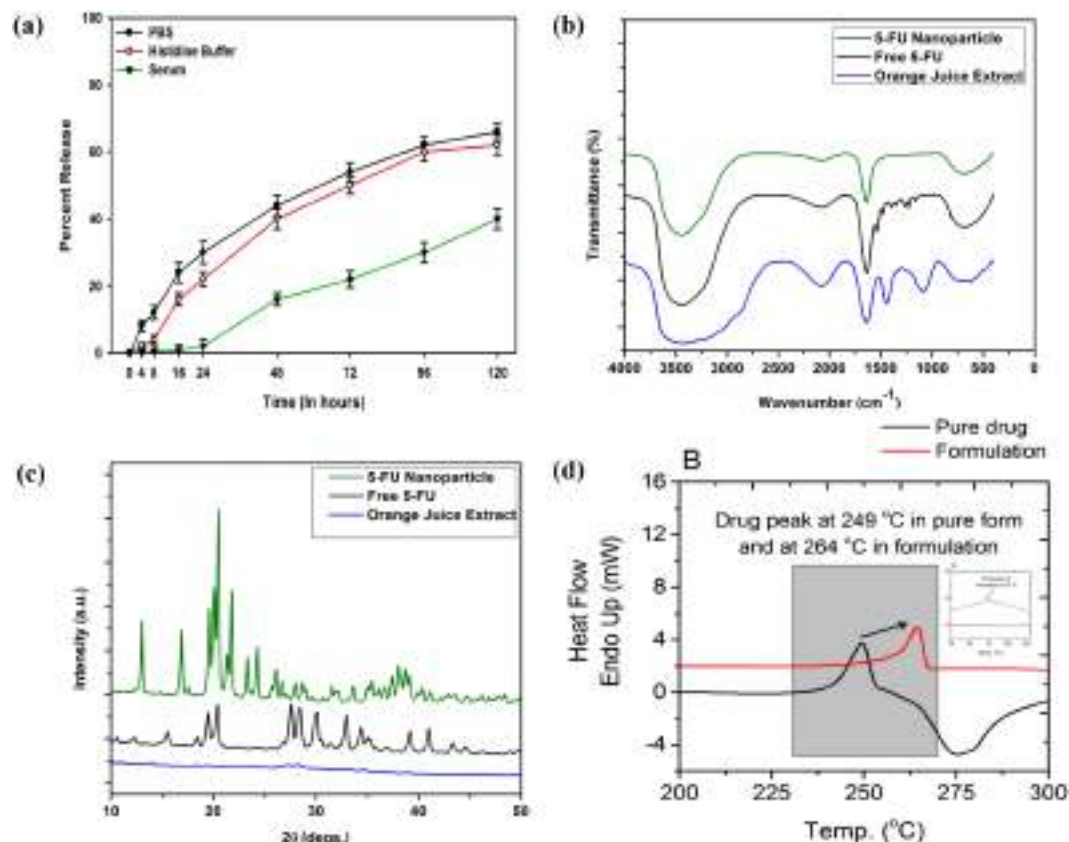


Figure 2. Assessment of purity and stability of as-synthesized 5-FU NPs employing FTIR, DSC, XRD analyses; To analyze stability of 5-FU NPs, multiple samples of the formulation were dispensed into various micro vials. After stipulated time period, the suspension was centrifuged and an aliquot of supernatant was analyzed to determine release pattern of the parent 5-FU molecules in the medium as described in Materials and Methods section; (a) stability of as-synthesized 5-FU NPs was determined by following release kinetics in PBS, histidine buffer as well as serum as incubation medium, (b) FTIR spectra, (c) XRD pattern and, (d) DSC thermograph of 5-FU NPs as determined by following method as described in ‘Methods’.

5-FU NPs mediated DNA fragmentation. 5-FU NPs mediated activation of endo-nucleases, during the apoptosis, ensues in DNA fragmentation. The nucleases break the higher order structure of chromatin into smaller fragments and finally into smaller DNA strands. Efficacy of 5-FU NPs was observed by BrdU tunnel analysis using FACS and fluorescence microscopy. The enzyme TdT catalyzes a template dependent addition of Br-dUTP to 3-hydroxyl ends of double and single stranded DNA. After incorporation, DNA breaks were identified by a FITC-labeled anti-BrdU mAb. Apoptosis induction was found to be significantly enhanced (** $p < 0.001$) in 5-FU NPs treated animals (Fig. 5a,b) as compared to the group treated with microcrystals of free 5-FU drug (* $p < 0.05$) (Fig. 5a,b), while both “OJ only in cream base” treated group as well as ‘cream base only treated control group’ showed fewer number of fluorescent labelled cells as revealed in Fig. 5a.

Apoptosis mediated loss of phospholipid asymmetry in the plasma membrane was observed using FITC Annexin-V staining. Apoptosis is significantly augmented in cells representing the 5-FU NPs treated group (Fig. 6a,b) when compared to that of microcrystals of free 5-FU drug treated animals (Fig. 6a). There was no significant augmentation of apoptosis in cells obtained from cream base treated mice as well as from the OJ along with cream base treated group (Fig. 6a), respectively).

Anticancer efficacy of 5-FU NPs against DMBA-induced fibrosarcoma. Kaplan-Mier Curve for survival analysis was used to evaluate the efficacy of as-synthesized 5-FU NPs against DMBA-induced fibrosarcoma in model animals (Fig. 7b). The survival of mice inflicted with fibrosarcoma was determined at various time intervals. Treatment with cream base alone or OJ in combination with cream base was not of much help as the animals did not survive for more than 8–9 weeks. On the other hand, survival rate at 12 weeks increased up to 45% in 5-FU microcrystals drug treated animals. Interestingly, 5-FU NPs treated animals showed dramatic increase in survival rate (68%) (** $p < 0.001$) when compared to control untreated group.

Effect of 5-FU NPs on the regression in tumor volume was also measured. The mean tumor volume per animal was significantly lower in animals treated with 5-FU NPs (40.4 mm³, $p < 0.001$) compared to those treated with the microcrystals form of drug (73.1 mm³, $p < 0.001$). On the other hand, treatment with a mixture of OJ in cream base and cream base alone (vehicle) resulted in much higher mean tumor volume compared to nano-assembled 5-FU drug (Fig. 7c).

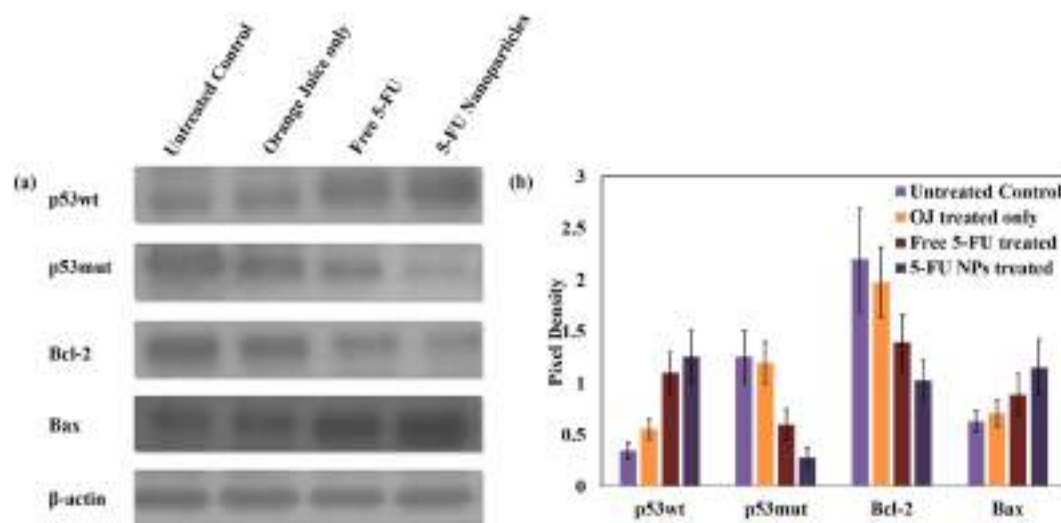


Figure 3. Effect of 5-FU NPs on expression of pro/anti apoptotic factors in tumor tissues from various experimental animal groups. **(a)** Cell lysates were prepared as described in Materials and Methods and analysed for expression of various proteins using specific antibodies. To ensure equal loading, the membranes were also probed with β -actin antibody. Densitograms show relative pixel density of p53wt, p53mut, Bcl-2 and Bax after treatment with various formulations as mentioned below. Lane 1, Untreated control (with cream base only); Lane 2, OJ along with cream base; Lane 3, Microcrystals of free 5-FU drug along with cream base; and Lane 4, 5-FU NPs prepared by mixing of 5-FU (10^{-3} M) solution with 5 ml of OJ (along with cream base). All the SDS-PAGE gels were run under similar experimental conditions. **(b)** Representative densitometry graph of the western blot. Pixel density of each band was quantified by using GS-800 Calibrated Imaging Densitometer. Statistical significance was calculated using unpaired student's t-test. $p \leq 0.05$ is considered statistically significant (Free 5-FU vs 5-FU NPs $p < 0.05$, Free 5-FU vs untreated control $p < 0.01$ and 5-FU NPs vs untreated control $p < 0.001$). Data represented as mean \pm Standard Deviation

The histo-pathological analysis of the excised tissue from various treated experimental groups further confirmed higher efficacy of 5-FU NPs. Healthy control animals showed normal skin with epidermal pegs, dermal papillae, and healthy pilosebaceous units with uniform thickness of epidermis and its associated keratinization (Fig. 8a). Untreated animals with cancer (Fig. 8b) showed papillary and cauliflowers like growth with remarkable increase in epidermal thickness and keratinization. Animals treated with cream base (carrier) or OJ along with cream base demonstrated papillomatous growth, moderate acanthosis and mild keratosis, complex fibro vascular core with congested vessels and loss of pilosebaceous units (Fig. 8c). Animals treated with microcrystals of free 5-FU drug showed papillomatous change, heavy acanthosis as well as keratosis (Fig. 8d). On the other hand, mice treated with 5-FU NPs resulted in sessile to pedunculated papillomatous change with heavy acanthosis and marked keratosis (Fig. 8e).

Discussion

Among various novel drug delivery systems, NPs have emerged as a suitable drug vehicle in regulating pharmacokinetics, pharmacodynamics and eventually the bioactivity of the active core compound^{1,28}. NPs entail enroute shielding/protection of the associated drug molecules and eventually facilitate their targeted delivery to the active site^{1,28,29}. In spite of their widely acclaimed potential for sustained drug release and potential to accumulate at the desired site, NPs do come across with series of barriers that impede attainment of desirable therapeutic outcome^{28–30}.

In the present study, we have established that orange juice extract (OJ) can induce formation of 5-FU NPs with exceptional physico-chemical attributes. The OJ constituents seems to regulate synthesis of as-synthesised 5-FU NPs in intriguing fashion. The incubation with relatively less OJ content (1 ml OJ with 5 ml of 10^{-3} M 5-FU solution; final volume of reaction mixture 10 ml) resulted in decrease in the absorbance. Incubation of drug with relatively larger ratio of OJ (3 ml OJ; 5 ml of 10^{-3} M 5-FU solution in final volume of the 10 ml) ensued in resurrection of characteristics 5-FU peaks. Further increase in OJ content (5 ml OJ; 5 ml of 10^{-3} M 5-FU solution keeping final volume upto 10 ml) resulted in restoration of the absorbance peak that tends to overlap with the peak height of the microcrystals of free 5-FU drug (data not shown). This clearly suggests that higher concentration of the active components of OJ facilitates ready formation of 5-FU NPs without changing the chemical structure of the parent nucleobase.

The UV absorption spectrum suggests that the microcrystals of free 5-FU drug absorbs maximally at 271 nm (Fig. S1d). Interaction of microcrystalline 5-FU with OJ resulted in significant quenching in absorbance of characteristic peaks belonging to 5-FU. Interestingly, longer incubation of 5-FU with OJ resulted in resurgence of absorbance with significant increase in intensity of various characteristic peaks in a time dependent manner. The resurrection of characteristic peaks with time suggests that chemical nature of 5-FU molecules is preserved during the synthesis of NPs. The significant higher absorption at ~ 245 nm contributed by C=O chromophore

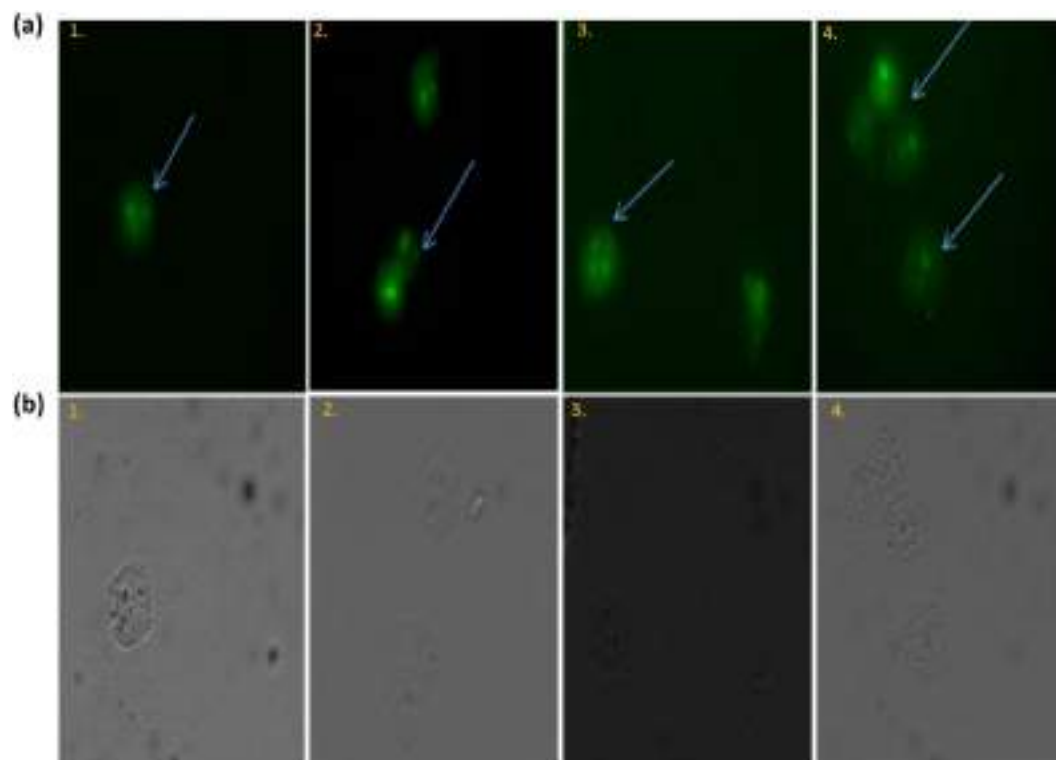


Figure 4. 5-FU NPs treatment results in Caspase-9 mediated apoptosis of fibrosarcoma cells as revealed by fluorescence microscopy. **(a)** Fluorescence micrographs **(b)** Phase contrast micrographs. Untreated group served as control (panel 1), the other experimental groups are: (panel 2) OJ with cream base, (panel 3) Microcrystals of free 5-FU drug with cream base, and (panel 4) 5-FU NPs with cream base. Cells obtained from the various experimental groups were visualized under a fluorescence microscope at 40X magnification (excitation at 488 nm, emission at 505–530 nm).

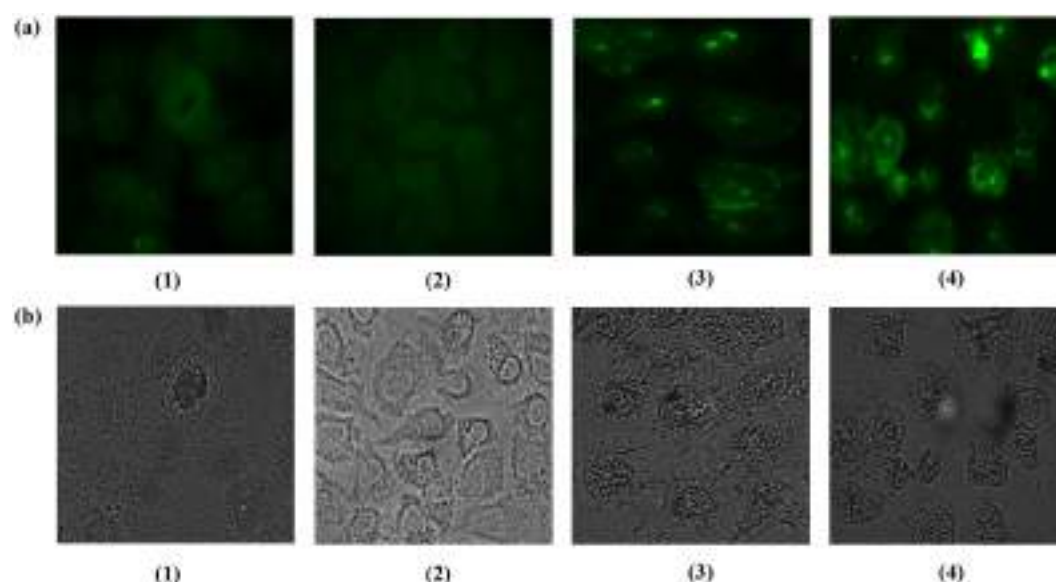


Figure 5. 5-FU NPs induce enhanced apoptosis potential in the treated animals as revealed by DNA fragmentation. **(a)** Fluorescence micrographs **(b)** Phase contrast. Nanoparticle mediated DNA fragmentation as observed by Apo-BRDU analysis by employing fluorescence microscopy. 5-FU NPs treated cells harbour large numbers of DNA breaks when compared with the parent 5-FU drug. While group (1) served as control (untreated), the other treated groups are: (2) OJ with cream base, (3) Microcrystals of free 5-FU drug with cream base, and (4) 5-FU NPs with cream base. Cells obtained from the various experimental groups were scanned under a fluorescence microscope at 40X magnification (excitation at 488 nm, emission at 505–530 nm).

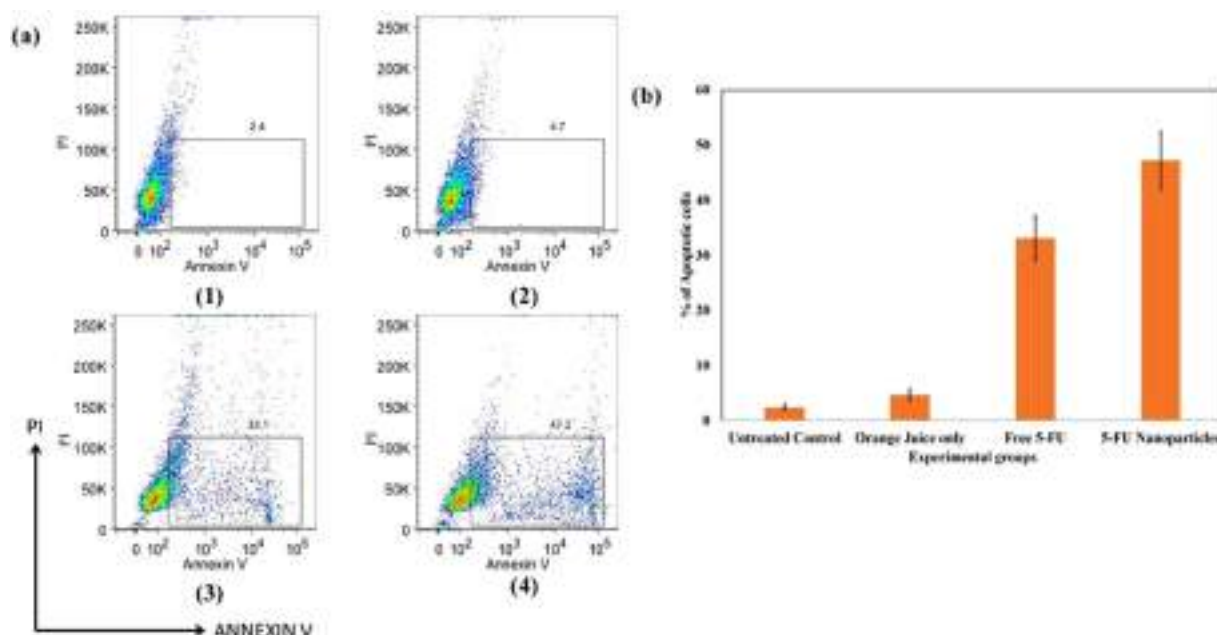


Figure 6. Effects of as-synthesized 5-FU NPs on the induction of apoptosis as analysed by Annexin V binding study. (a) Annexin V apoptosis detection employing FACS analysis. Apoptosis induction was assessed in the cells isolated from various experimental groups. As revealed by Annexin V binding, apoptosis is significantly augmented in cells belonging to 5-FU NPs treated mice when compared to microcrystals of free 5-FU drug treated mice. While group (1) served as control (untreated), the other treated groups are: (2) OJ with cream base, (3) Microcrystals of free 5-FU drug with cream base, and (4) 5-FU NPs with cream base. (b) The percentage of apoptotic cells was significantly enhanced in the 5-FU NPs (5-FU-NPs vs untreated control $p \leq 0.001$) treated group of animals when compared to parent 5-FU drug (Free 5-FU vs untreated control $p \leq 0.05$) as represented in the form of Histogram.

remains unscathed during NP synthesis. (Fig. S1d). Similarly, absorption peak at ~ 192 nm, which is contributed by hetero atom ($-N$) containing pyrimidine ring, also remained intact in the as-formed 5-FU NPs. The blue shift of peak at 272 nm suggests that chromophore actively participate in non-covalent bonding of parent 5-FU molecules in as-synthesised NPs. The microenvironment of a chromophoric groups of a given chemical compound affects the $S\pi$ life-span by tuning the relative energy of the $S\pi$ state and the closely lying S_n dark state³¹. The stability of $\pi-\pi^*$ transition (in the case of 5-FU; it is the transfer of an electron from the lone pair of oxygen or nitrogen atom towards the more diffuse π^* orbital) increases both with the polarity and hydrogen bonding ability of 5-FU with the external milieu. It seems that, the external milieu of an individual 5-FU molecule, in a given nanoparticle, modulates both $\pi-\pi^*$ as well as $n-\pi^*$ transitions^{32,33}.

Dietary flavonoids specifically naringenin, hesperetin and quercetin *etc.*³⁴ present in OJ have great potential in suppressing synthesis of DNA, RNA and proteins and demonstrate a detrimental effect on rapidly growing cells including cancerous cells. Interestingly, various secondary metabolites present in OJ have been categorically reported to possess strong anticancer potential against skin fibrosarcoma and colon carcinogenesis amongst others (Table 1).

One can argue that as-synthesized 5-FU NPs may contain OJ components incorporated during their synthesis. Considering it a desirable feature, as OJ has been reported to contain plethora of antioxidant substances with anticancer potential, we performed FT-IR, DSC and XRD analysis of as-formed 5-FU NPs to elucidate this possibility. Incidentally, because of overlapping chemical characteristics of the 5-FU with that of OJ components (small molecules with aromatic nucleus), the FT-IR data fail to reveal much about presence of OJ components in the as-synthesized 5-FU NPs. Nevertheless, specific wave numbers corresponding to a given functional group moiety suggests presence of very small amount of OJ contents in as-formed NPs. In contrast, DSC analysis suggests that while 5-FU molecules form the core of as-synthesized NPs. There was an additional peak corresponding to much less temperature. It seems this peak refers to the energy needed to break bonding of 5-FU drug molecules (intra-particle) present in a given as-synthesized 5FU-NP, that remain associated with each other as well as with residual OJ constituents still present in the NPs, via non-covalent bonds.

It can be speculated that the residual OJ contents still present in 5-FU NPs may exert their anti-cancer effects and help in effective suppression of DMBA induced skin cancer in the experimental mice. In addition, the fabricated 5-FU NPs release the active drug for an extended time period. The particles remain intact even in the presence of plasma components and released around 60% of the entrapped drug in 5 days. It seems OJ mediated 5-FU NP synthesis progresses via a self-nucleation process initially that eventually ensues in formation of primary particles³². The as-formed primary nuclei function as a seed to facilitate particle growth accompanied by an increase in the thermodynamic stability. The synthesis of NPs further followed heterogeneous nucleation and growth; a process referred to as Ostwald ripening. In process of NP fabrication, higher oligomers trap the monomers in their native orientation and inhibit structural rearrangements^{31–33}. It can, therefore, be stipulated that the

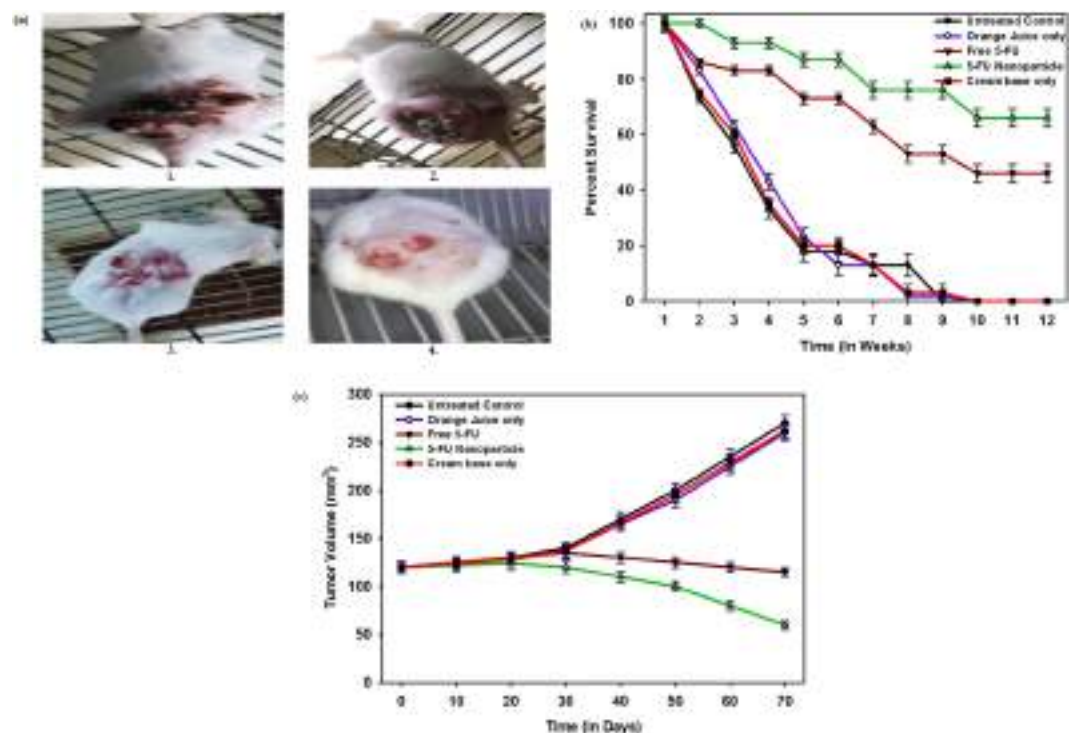


Figure 7. Efficacy of the as-synthesized 5-FU NPs as revealed by survival, regression in tumor volume and fibrosarcoma suppression. (a) 5-FU NPs mediated suppression of DMBA induced fibrosarcoma in BALB/c mice. BALB/c mice were exposed to DMBA to induce fibrosarcoma following method as described in methodology section. The animals with fibrosarcoma were divided in four groups viz. Group (1) represent untreated control animals while other groups are (2) OJ along with cream base, (3) Microcrystals of free 5-FU drug along with cream base, (4) 5-FU NPs along with cream base, (b) Effect of various formulation on survival of BALB/c mice with fibrosarcoma. Survival data depicting efficacy of 5-FU NPs formulation in terms of percent survival at various time points (post treatment). While group (1) served as control (untreated), the other treated groups were: (2) OJ with cream base, (3) Microcrystals of free 5-FU drug with cream base, and (4) 5-FU NPs with cream base. The animals treated with 5-FU NPs showed significantly better survival ($p < 0.001$) as compared to control groups. p value < 0.001 ; 5FU-NPs vs untreated control and p value < 0.01 , free 5-FU (microcrystalline) vs untreated control group. (c) Tumor volume regression in animals with fibrosarcoma after treatment with various formulations of 5-FU drug. p value ≤ 0.01 ; 5-FU NPs vs untreated group.

5-FU dimers/tetramers can act as seeding point (nucleus) for the condensation of monomers and eventually lead to the formation of super-aggregated NPs. The contents of OJ function both as a driving force as well as stabilizing agent in the whole process.

Nanoparticle based drug formulation occupies a special status as a means to increase the efficacy of parent drug molecules. In order to study the efficacy of synthesized 5-FU NPs we carried out various apoptosis related studies employing different *in vitro* assays on epidermoid cancer cell lines (A253) viz. MTT assay (Fig. S4A), Western blot analysis of cell cycle regulating proteins *etc.* (Fig. S4B). The *in vitro* data establishes higher efficacy of formed 5-FU NPs and also suggest that the observed anti-cancer effects are mediated by physical presence of NPs and not by the controlled delivery route that may result in a greater amount of free drug reaching the tumor cells (Fig. S4C to E).

The real anti-cancer potential of 5-FU NPs, described in the present study, cannot be achieved without performing *in-vivo* studies. Therefore, in the next set of experiments, the anticancer potential of 5-FU NPs was evaluated by analyzing the expression levels of various pro and anti-apoptotic factors in the fibrosarcoma skin tissues of model animals. p53, a tumor suppressor gene that integrates various signals that regulate cell cycle is manipulated in cancer cells^{25,35}. The failure of p53 expression (*cf.* p53mut induction) generally ensues in tumor development. Interestingly, treatment of the model animals with as-synthesized 5-FU NPs was successful in restoring expression of p53 as compared to treatment with the free form of 5-FU drug ($*p < 0.05$). Intriguingly, the treatment with as-synthesized 5-FU NPs also augmented expression of Bax, a p53 target that Trans-activates numerous factors during p53-dependent apoptosis, in the fibrosarcoma tissue.

The high pro-apoptotic efficacy of as synthesized 5-FU NPs was also confirmed by analyzing expression level of p53mut and Bcl-2 in the cancerous tissues of the treated animals^{22,24,36,37}. The 5-FU NPs markedly down regulate expression of both Bcl-2 and p53mut. Annexin V apoptosis analysis that detects the presence of phosphatidyl-serine in the outer leaflet of cancer cells further confirms apoptosis induction by treatment with 5-FU NPs.

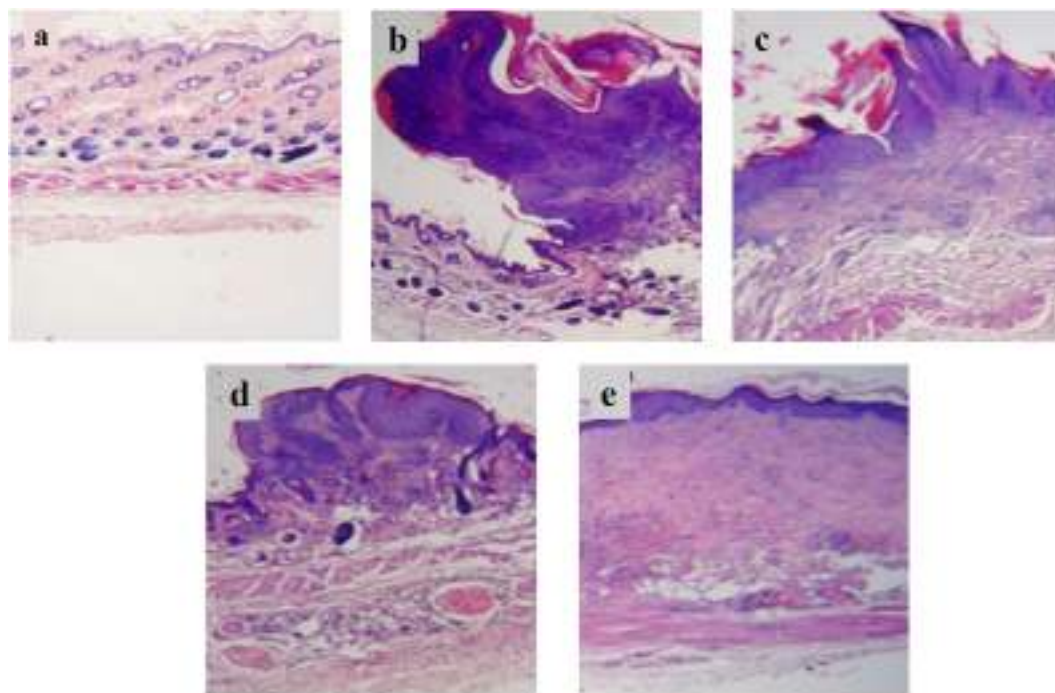


Figure 8. Histopathological analysis of excised tissue isolated from 5-FU NP-treated experimental animals. The histo-pathological results of the excised tissue from various treated experimental groups. (a) Healthy control animals showed normal skin with epidermal pegs, dermal papillae, healthy pilosebaceous units with uniform thickness of epidermis and its associated keratinization, (b) Untreated animals with cancer or animals treated with cream base (carrier) only, (c) Animals treated with OJ along with cream base, (d) Animals treated with microcrystals of free 5-FU drug showed papillomatous change, heavy acanthosis as well as keratosis, and (e) Animals treated with Nano-assembled 5-FU NPs resulted in sessile to pedunculated papillomatous change with heavy acanthosis and marked keratosis.

The observed higher efficacy of 5-FU NPs can be correlated with better penetration and retention of 5-FU NPs as compared to parent 5-FU drug. Upon their application to the skin, the internalized NPs release their payload (active drug) into the cells that consequently forms the basis of better efficacy over the free form (microcrystalline) of the drug. The histopathological studies support the theory that 5-FU NPs facilitate efficient killing of cancer cells as compared to parent 5-FU drug (Fig. 8).

The excipient-free Nanoparticle based novel drug delivery system, introduced in the present study, holds great promise in release of the drug molecules in slow and sustained manner. This effectively influences the cell cycle check points, thereby causing effective killing of the cancer cells and significantly reduce the level of mortality in fibrosarcoma animals.

Conclusions

The present study reports orange juice content mediated synthesis of 5-FU NPs. The biophysical characterization suggests synthesis of homogenous population of 5-FU NPs with nano-meter size dimensions. The 5-FU NPs were found to kill epidermoid cancer cells more efficiently as compared to the micro-sized crystals of 5-FU. Both *in vitro* as well as *in vivo* studies proposed that 5-FU NPs modulate various components of cell cycle to induce apoptosis of target cancer cells. The as-synthesized NPs successfully increase efficacy of parent 5-FU drug in curing experimental murine fibrosarcoma in Balb/c mice.

Methods

Reagents. Reagents used in the experiments were of high purity. 5-Fluorouracil, bicinechonic acid (BCA), dialysis tubing cellulose membrane (cut off size MW = 3kD), syringe-driven filters of 0.22 μ m size were procured from HiMedia Laboratories Pvt. Ltd India. Antibodies for the apoptosis detection were purchased from BD Biosciences India and Santa Cruz biotechnology, Inc. Rabbit anti-mouse p53wt, rabbit anti-mouse p53mut, rabbit anti-mouse Bcl-2, rabbit anti-mouse Bax, rabbit anti-mouse β -actin, FITC labelled Annexin-V, caspase-9 p35 antibody and goat anti-rabbit IgG-FITC conjugated secondary antibody were the product of Sigma-Aldrich, USA.

Ethical conduct of research. Inbred female BALB/c mice (6–8 weeks old, 20 ± 2 g) were obtained from the Animal House Facility of Interdisciplinary Biotechnology Unit, Aligarh Muslim University. The BALB/c mice were housed in commercially available polypropylene cages and maintained under controlled temperature conditions on a 12 hr light-dark cycle and had free access to food and water ad libitum. All experimental procedures involving animals were approved by the Institutional Animal Ethics Committee (IAEC) of the Interdisciplinary

Biotechnology Unit, Aligarh Muslim University, Aligarh, India (Approval ID: 332/CPCSEA). All the animal experiments were performed according to the National Regulatory Guidelines issued by the Committee for the Purpose of Control and Supervision of Experiments on Animals (CPCSEA), Government of India.

Preparation of orange juice. Edible juicy part (30 g) of orange was chopped into small pieces and blended in a food grinder³⁷. Briefly, (30 g) of orange pulp was mixed with 100 ml of double distilled water then it was grounded in mixer. The obtained extract was boiled for several minutes till its volume was reduced to 1/3 of initial volume. The boiled extract was filtered through Whatman filter and the filtrate was stored at -20°C till further use.

Preparation of Nano-drug formulation employing orange juice (OJ). The synthesis of 5-FU nano-drug formulation was executed employing orange fruit extract. The increasing volumes [1–5 ml of 30% w/v stock solution (Stock solution: 30 g pulp in 100 ml of water)] of extract were added to 5 ml of 1 mM solution of 5-FU and the volume was made up to 10 ml by deionized water. The mixture was incubated for a given time period at 25°C , followed by centrifugation at 1,00,000 g for 2 hr to pellet the 5-FU nanoparticles. The pellet obtained was lyophilized to obtain free flowing powder. The nanoparticles were suspended in 1 ml of PBS (10 mM phosphate, 150 mM NaCl, pH 7.4) and further characterized by various spectrophotometric and microscopic techniques.

Characterization of 5-FU NPs. *Transmission electron microscopy.* A JEOL Transmission Electron Microscope (JEOL, Tokyo, Japan) was used for Imaging of in-house synthesized 5-FU Nanoparticle. Briefly, samples were prepared following a published method by drying a drop of synthesized NPs on a carbon coated copper grid. TEM micrographs were acquired with an accelerating voltage of 100/120 kV.

Particle size distribution and Zeta-potential. Particle size distribution of the synthesized NPs was analyzed using dynamic light scattering on DynaPro-TC-04 DLS instrument (Protein Solutions, Wyatt Technology, Santa Barbara, CA) the size distribution of as-synthesized NPs was also observed by Nanophox particle size analyzer (Sympatec GmbH, Clausthal-Zellerfeld, Germany). To evaluate the stability and surface charge of the as synthesized 5-FU NPs, zeta potential was determined using DTS software (Malvern Instruments, Worcestershire, UK) based on M3-PALS technology following a method standardized in our laboratory³⁸. 5-FU NPs were suspended in phosphate buffer (10 mM, pH 7.4) and thoroughly mixed in a cyclo-mixer for 1 min and used for zeta sizing as well as surface charge determination.

UV-spectrophotometric analysis. Biomimetically synthesized 5-FU NPs were analyzed for surface plasmon resonance by employing double beam UV-Visible spectrophotometer (Perkin Elmer, Boston, MA) and scanned in 180–700 nm wavelength range using 10 mm optical path length quartz cuvettes.

Atomic Force Microscope (AFM) Imaging. AFM was performed by using Perkin-Elmer digital AFM microscope equipped with a Nano-scope controller following published protocol³⁹. 5-FU NPs were suspended in 1 ml (10 mM PBS, pH 7.4) of followed by brief ultra-sonication to agitate particles in a solution in order to prevent agglomeration of NPs. Subsequently, a drop of the diluted 5-FU NPs was put onto the Si (III) disc for AFM imaging.

Differential scanning calorimetry (DSC). DSC study was carried out on dried samples of pure 5-FU (control) and formulation containing 5-FU. Briefly, 3–5 mg dried powder was placed in an aluminium pan. Empty aluminium pan was used as reference. The sample pan and reference pan were heated at constant flow rate of $10^{\circ}\text{C}/\text{min}$ within the temperature range of $10\text{--}350^{\circ}\text{C}$ (Simultaneous Thermal Analyser (STA) 8000, Perkin Elmer, USA). Nitrogen gas was continuously purged (Flow rate = 20 ml/min) throughout the experiment. The data obtained was smoothened and corrected for baseline using Origin Pro (64 bit, Sr3, b275, OriginLab Corporation, Northampton, MA01060, USA)^{19,20}.

Evaluation of in-vitro Nano-drug release kinetics. Release kinetics of 5-FU NPs, was examined by dispensing multiple samples of the formulation into various micro vials following the protocol as standardized in our lab. To each vial, 1.0 ml of release medium was dispensed along with 0.01% of sodium azide to prevent microbial growth. At stipulated time period, an aliquot (40 μl) of supernatant was removed after centrifugation at 1×10^5 for 10 minutes at 25°C . The aliquots were replenished with fresh buffer to maintain constant volume of the suspension. HPLC of 5-FU was performed following a published method that was modified in our lab⁴⁰. Briefly, chromatographic separation was carried out using symmetry C18, 5 μm (3.9×150 mm) column. Mobile phase consisted of 40 mM phosphate buffer, pH 7.0 with 10% (w/v) potassium hydroxide. Flow rate was kept 1.0 ml/min and detection wavelength was 260 nm. At every time point, 20 μl of sample was injected and Absorbance was recorded. Drug concentration of the sample was calculated from the calibration curve prepared using pure drug mixed in release medium.

Tumor induction. Male BALB/c mice in the resting phase of hair cycle were included for the induction of skin fibrosarcoma. The animals were shaved in the dorsal portion over an area of $2\text{--}3\text{ cm}^2$ employing electric clippers followed by the exposure to DMBA (52 μg in 200 μl acetone) that was applied topically three times a week for 12 weeks. At the end of 12 weeks, the mice which had $\sim 120\text{ mm}^3$ tumor size were used in the study.

Treatment schedule. To assess the anticancer efficacy of 5-FU NPs, animals were divided in four various groups each consisting of 25 animals. Group I consisted of DMBA exposed BALB/c mice (having papilloma growth) that were subsequently treated with carrier only and served as a control group. The remaining three groups consisted of animals that were earlier exposed to DMBA and had papilloma growth on their skin. Group II was treated with OJ along with cream base (5% v/v of OJ stock solution in cream base). The tumor bearing animals belonging to

group III were treated with microcrystals of parent 5-FU drug along with cream base (5% w/v of microcrystal of parent 5-FU drug in cream base). Group IV was treated with 5-FU NPs along with cream base (5% w/v of 5-FU NPs in cream base).

Determination of tumor volume. The measurement of tumor diameter of the treated groups of animals was performed by employing Vernier Caliper and the tumor size was calculated by the following formula:

$$V = D^2 \times d^2 \times \pi/6$$

where V is the measure of tumor volume, D is the measure of biggest dimension of the tumor and d is the measure of smallest dimension of the tumor. The tumor tissues were excised from the animals and underwent entire skin examination.

Histopathological studies. To assess efficacy of 5-FU NPs against the tumor development, skin tumor tissues were sliced from three mice of each group and fixed in 10% formaldehyde solution, dehydrated in ascending grades of ethyl alcohol, cleared in xylol and mounted in molten paraplast at 58–62 °C. The finely cut thin sections were stained with hematoxylin and eosin and examined for any morphological change under an Olympus BX40 microscope (PA, USA).

Isolation of nuclear fraction from the tumor tissues. The tumor tissues were aseptically excised from skin of animals belonging to various treated groups. Briefly, the tissues were homogenized in a REMI homogenizer (REMI Laboratory Instruments, New Delhi, India) to prepare nuclear fraction in the presence of protease inhibitor cocktail and PMSF following published method as modified in our laboratory⁴¹.

Expression level of various apoptotic markers upon treatment with 5-FU Nano-particles. Western blot was performed for the analysis of expression of various apoptotic markers like p53wt, p53mut, Bcl-2 and Bax in tumor tissues of the treated groups⁴². Before resolving expressed protein employing SDS-PAGE, protein content of each sample was estimated using a Bicinchoninic Acid solution kit (Sigma-Aldrich, Co., USA)⁴³. Briefly protein (30 µg/lane) was loaded and resolved by electrophoresis on 10% sodium dodecyl sulfate-polyacrylamide gel and transferred onto PVDF membrane. After blocking in 5% non-fat dry milk prepared in phosphate-buffered saline (PBS) with Tween-20 (PBS-T), the membrane was washed three times with PBST and incubated for 2 hrs at 37 °C with rabbit anti-mouse p53wt, rabbit anti-mouse p53mut, rabbit anti-mouse Bax and rabbit anti-mouse Bcl-2 primary antibodies. After incubation and stipulated washing steps, the membrane was further incubated with HRP conjugated goat-anti-mouse secondary antibody (1:5000) for 1 hr at 37 °C. Blots were developed with the ECL (Enhanced chemi-luminescence) detection system (Bio-Rad). The pixel density of the bands was quantified using GS-800 Calibrated Imaging Densitometer (Bio Rad, India).

Assessment of apoptosis potential of 5-FU NPs employing Fluorescence microscopy. The DMBA induced fibrosarcoma tissues were removed from the treated mice of respective experimental groups. Briefly, excised tissue was cut into small pieces with scalpel, dissociated with the frosted slides and suspended in the petri-dish containing 1 ml of collagenase P (3 mg/ml) dissolved in 15 ml of RPMI media containing 10% FBS. Incubated at 37 °C with gentle shaking and after 3 hr of incubation passed through cell strainer. Single cell suspension of $1-2 \times 10^6$ cells was prepared by pelleting down cells at $1600 \times g$ for 5 min at 4 °C. Cell suspension was fixed in 1% paraformaldehyde in PBS (pH 7.4) and placed on ice for 30 min. Cells were settled down at $300 \times g$ for 5 min and washed with 5 ml of PBS (pH 7.4). Pelleted cells were re-constituted in 50 µl PBS (pH 7.4) and fixed in 2 ml of 70% chilled ethanol. Suspension was again washed twice with 1 ml of wash buffer and pelleted cells were re-constituted in 50 µl of DNA labeling solution and incubated for 60 min at 37 °C. After incubation, cells were washed and re-suspended in FITC-conjugated anti-bromodeoxyuridine (BrdU) antibody at 25 °C for 30 min. The cell suspension was washed and further dissolved in 1 ml of PBS and 50 µg/ml PI/RNase was added to antibody-labeled cells, which were further incubated at 37 °C for 30 min. Stained cells were finally analyzed by Zeiss, AxioCam Imager MRM M2(Thornwood, NY United States)⁴⁴.

Determination of caspase-9 level in apoptotic cells post 5-FU Nanoparticle treatment. Single cell suspensions of the excised tissue from the various respective group were fixed with 1% paraformaldehyde plus 0.19% picric acid in PBS (pH 7.4) for 1 hour at RT. Subsequently, the fixed cells were treated with permeabilizing solution containing 0.1% SDS in PBS incubated for 10 min at RT and stained with a primary antibody (caspase-9 p35 antibody) that specifically binds with the p35 subunit of caspase-9 and further incubated with a goat anti-rabbit IgG-FITC conjugated secondary antibody (Sigma-Aldrich, USA)⁴⁵. Fluorescence imaging was conducted using a Zeiss, AxioCam Imager MRM M2(Thornwood, NY United States).

Apoptosis detection employing FITC labeled annexin-V binding analysis. To evaluate the apoptotic potential of 5-FU NPs, skin samples from animals belonging to various treated groups, were collected. Single cell suspension was prepared as described elsewhere and analyzed with commercial FITC labelled Annexin-V (BD Pharmingen) according to the manufacturer's instructions. The cells were incubated with 5 µl FITC Annexin-V. Apoptosis was analyzed by Annexin-V FITC and PI staining by flow cytometry. AnnexinV[−], PI[−] represent live cells, annexinV⁺, PI[−] represent early apoptotic cells, and annexin V⁺, PI⁺ cells represent late apoptotic cells. The total cell undergoing apoptosis can be represented as annexin V⁺. Cells were gently vortexed and incubated at room temperature for 15 min. Finally, 400 µl of 1X binding buffer was added and cells were analyzed using BD FACSVERSE flow cytometer, (BD Biosciences, United States)⁴⁶.

Statistical analysis. Results were expressed as the mean \pm SEM and data were analysed by means of one way analysis of variance (ANOVA) and two-way ANOVA to assess the differences among various groups. Statistical calculations were performed with the help of Graph-Pad prism version 6.0, Graphpad software Inc San Diego, California, USA. Significance was indicated as *** for $P < 0.001$; ** for $P < 0.01$ and * for $P < 0.05$. Student T-test was used to study difference in biochemical parameters between different treatment groups. The difference with $P < 0.05$ considered to be significant. Kaplan-Mier Curve was used for survival analysis of the treated groups.

References

1. Blanco, E., Shen, H. & Ferrari, M. Principles of Nanoparticle design for overcoming biological barrier to drug delivery. *Nature biotechnology* **33**, 941–951 (2015).
2. Edward, S. A. *et al.* Nanoparticle exposure in animals can be visualized in the skin and analysed via skin biopsy. *Nature communications* **5**, 3796 (2013).
3. Wilhelm, S. *et al.* Analysis of Nanoparticle delivery to tumors. *Nature Reviews. Materials* **1**, 16014 (2016).
4. Li, L., Gu, W., Chen, J., Chen, W. & Xu, Z. P. Co-delivery of siRNAs and anti-cancer drugs using layered double hydroxide nanoparticles. *Biomaterials* **35**(10), 3331–9 (2014).
5. A Baudino, T. Targeted cancer therapy: the next generation of cancer treatment. *Current drug discovery technologies* **12**(1), 3–20 (2015).
6. Qu, C.-Y. *et al.* Engineering of lipid prodrug-based, hyaluronic acid-decorated Nanostructured lipid carriers platform for 5-fluorouracil and cisplatin combination gastric cancer therapy. *International journal of Nanomedicine* **10**, 3911 (2015).
7. Luo, C. H., Shanmugam, V. & Yeh, C. S. Nanoparticle biosynthesis using unicellular and subcellular supports. NPG Asia. *Materials*. **7**(8), e209 (2015).
8. Peer, D. *et al.* Nanocarriers as an emerging platform for cancer therapy. *Nature Nanotechnology* **2**, 751–760 (2007).
9. Huang, N. *et al.* Optical Epitaxial Growth of Gold Nanoparticle Arrays. *Nano letters* **15**, 5841–5845 (2015).
10. Hussain, I. *et al.* Green synthesis of nanoparticles and its potential application. *Biotechnology letters*. **38**(4), 545–60 (2016).
11. Basavegowda, N. *et al.* Plant mediated synthesis of gold nanoparticles using fruit extracts of Ananas comosus (L.) (Pineapple) and evaluation of biological activities. *Advanced materials letters* **4**(5), 332–7 (2013).
12. Sundrarajan, M., Ambika, S. & Bharathi, K. Plant-extract mediated synthesis of ZnO nanoparticles using Pongamia pinnata and their activity against pathogenic bacteria. *Advanced powder technology* **26**(5), 1294–9 (2015).
13. Klekotko, M. *et al.* Bio-mediated synthesis, characterization and cytotoxicity of gold nanoparticles. *Physical Chemistry Chemical Physics* **17**(43), 29014–9 (2015).
14. Xie, J. *et al.* Bio-mediated synthesis and antibacterial activity against aquatic pathogens of silver nanoparticles decorated titania nanosheets in dark and under solar-light irradiation. *Materials Technology* **6**, 1–1 (2018).
15. Prasanna kumar, J. B. *et al.* Bio-mediated route for the synthesis of shape tunable Y2O3: Tb3+ nanoparticles: Photoluminescence and antibacterial properties. *Spectrochimica Acta Part A: Molecular and Biomolecular Spectroscopy* **5**(151), 131–40 (2015).
16. Roy, S., Das, T. K., Maiti, G. P. & Basu, U. Microbial biosynthesis of nontoxic gold nanoparticles. *Materials Science and Engineering: B* **203**, 41–51 (2016).
17. Chauhan, A. *et al.* Aloe vera induced biomimetic assemblage of nucleobase into Nanosized particles. *PloS one* **7**, e32049 (2012).
18. Chandran, S. P. *et al.* Synthesis of gold Nano triangles and silver NPs using Aloe vera plant extract. *Biotechnology progress* **22**, 577–583 (2006).
19. Singh, P. *et al.* Thermal stability studies of 5-fluorouracil using diffuse reflectance infrared spectroscopy. *Drug testing and analysis* **1**, 240–244 (2009).
20. Clas, S. D., Dalton C. R. & Hancock B. C. Encyclopedia of Pharmaceutical Technology. Marcel Decker Inc. 2002:289 (2002).
21. Arias, J. L. Novel strategies to improve the anticancer action of 5-fluorouracil by using drug delivery systems. *Molecules* **13**(10), 2340–2369 (2008).
22. Große, L. *et al.* Bax assembles into large ring-like structures remodeling themitochondrial outer membrane in apoptosis. *EMBO J* **35**, 4, 402–413 (2016).
23. Hollstein, M. *et al.* p53 mutations in human cancers. *Science* **253**, 5015, 49–53 (1991).
24. Amson, R. B. *et al.* Isolation of 10 differentially expressed cDNAs in p53-induced apoptosis: activation of the vertebrate homologue of the drosophila seven in absentia gene. *Proceedings of the National Academy of Sciences* **93**, 3953–3957 (1996).
25. Levine Arnold, J. p53, the cellular gatekeeper for growth and division. *Cell* **88**, 3, 323–331 (1997).
26. Cohen, G. M. Caspases: the executioners of apoptosis. *Biochemical Journal* **326**, 1, 1–16 (1997).
27. Tait, S. W. G. & Douglas, R. G. Mitochondria and cell death: outer membrane permeabilization and beyond. *Nature reviews Molecular cell biology* **11**, 9, 621–632 (2010).
28. Davis, M. E. & Dong, M. S. Nanoparticle therapeutics: an emerging treatment modality for cancer. *Nature reviews Drug discovery* **7**, 9, 771–782 (2008).
29. Sun, T. *et al.* Engineered NPs for drug delivery in cancer therapy. *Angewandte Chemie International Edition* **53**, 46, 12320–12364 (2014).
30. Sahoo, S. K. & Fahima Dilnawaz, S. K. Nanotechnology in ocular drug delivery. *Drug discovery today* **13**, 3, 144–151 (2008).
31. Xia, Y. *et al.* Shape controlled synthesis of metal nanostructures: The case of silver. *Chem Eur J* **11**, 454–463 (2005).
32. Santoro, F. *et al.* Solvent Effect on the Singlet Excited-State Lifetimes of Nucleic Acid Bases: A Computational Study of 5-Fluorouracil and Uracil in Acetonitrile and Water. *J Am Chem Soc* **128**, 16312–16322 (2006).
33. Zia, Q., Mohammad, O., Rauf, M. A., Khan, W. & Zubair, S. Biomimetically engineered Amphotericin B nano-aggregates circumvent toxicity constraints and treat systemic fungal infection in experimental animals. *Sci. Rep.* **7**, 11873 (2017).
34. Erlund, I. Review of the flavonoids quercetin, hesperetin, and naringenin. *Dietary sources, bioactivities, bioavailability, and epidemiology. Nutrition Research* **24**, 10, 851–874 (2004).
35. Jacobson, M. D. & Martin, C. R. Programmed cell death and Bcl-2 protection in very low oxygen. *Nature* **374**, 814–816 (1995).
36. Oltval, Z. N., Curt, L. M. & Stanley, J. Korsmeyer. Bcl-2 heterodimerizes *in vivo* with a conserved homolog. Bax, that accelerates programmed cell death. *Cell* **74**, 4, 609–619 (1993).
37. Valente, A. *et al.* Development of an orange juice in-house reference material and its application to guarantee the quality of vitamin C determination in fruits, juices and fruit pulps. *Food chemistry* **154**, 71–77 (2014).
38. Farazuddin, M. *et al.* Anticancer efficacy of perillyl alcohol-bearing PLGA microparticles. *International journal of Nanomedicine* **7**, 35–47 (2012).
39. Sun, S. *et al.* Monodisperse FePtNPs and ferromagnetic FePt Nanocrystal superlattices. *Science* **287**, 5460, 1989–1992 (2000).
40. Teixeira, J. *et al.* Hydroxy-cinnamic acid antioxidants: an electrochemical overview. *Bio Med research international* **2013**, 11, <https://doi.org/10.1155/2013/251754> (2013).
41. Khan, A. *et al.* Potential of diallyl sulfide bearing pH-sensitive liposomes in chemoprevention against DMBA-induced skin papilloma. *Molecular Medicine* **13**, 7–8, 443–451 (2007).

42. Sherwani, M. A. *et al.* Dendrimer-PLGA based multifunctional immuno-Nanocomposite mediated synchronous and tumor selective delivery of siRNA and cisplatin: potential in treatment of hepatocellular carcinoma. *RSC Advances* **5**, 39512–39531 (2015).
43. Smith, P. K. *et al.* Measurement of protein using bicinchoninic acid. *Analytical biochemistry* **150**, 1, 76–85 (1985).
44. Kishimoto, H. & Sprent, J. Strong TCR ligation without co-stimulation causes rapid onset of Fas-dependent apoptosis of naive murine CD4+ T cells. *The Journal of immunology* **163**, 4, 1817–1826 (1999).
45. Li, P. *et al.* Cytochrome c and dATP-dependent formation of Apaf-1/caspase-9 complex initiates an apoptotic protease cascade. *Cell* **91**, 4, 479–489 (1997).
46. Bossy-Wetzel, E. & Douglas, R. G. Detection of apoptosis by annexin V labeling. *Methods in enzymology* **322**, 15–18 (2000).
47. Yang, J. *et al.* Naringenin attenuates mucous hypersecretion by modulating reactive oxygen species production and inhibiting NF- κ B activity via EGFR-PI3K-Akt/ERK MAPKinase signaling in human airway epithelial cells. *Molecular and cellular biochemistry* **351**(1–2), 29–40 (2011).
48. Cincin, Z. B. *et al.* Anti-proliferative, apoptotic and signal transduction effects of hesperidin in non-small cell lung cancer cells. *Cellular Oncology* **38**, 3, 195–204 (2015).
49. Jia, S.-S. *et al.* Induction of apoptosis by D-limonene is mediated by inactivation of Akt in LS174T human colon cancer cells. *Oncology reports* **29**, 1, 349–354 (2013).
50. Hamilton, I. M. J. *et al.* Interactions between vitamins C and E in human subjects. *British Journal of Nutrition* **84**, 3, 261–267 (2000).
51. Thakur, A., Singla, R. & Jaitak, V. Coumarins as anticancer agents: A review on synthetic strategies, mechanism of action and SAR studies. *European journal of medicinal chemistry* **101**, 476–495 (2015).
52. Vergote, I. B., Marth, C. & Robert, L. Coleman. Role of the folate receptor in ovarian cancer treatment: evidence, mechanism, and clinical implications. *Cancer and Metastasis Reviews* **34**, 1, 41–52 (2015).

Acknowledgements

The authors are thankful to the Coordinator of Interdisciplinary Biotechnology Unit, AMU, Aligarh, India for providing the institute's research facilities. The authors gratefully acknowledge the financial support by the Indian Council of Medical Research and DBT, Govt. of India (BMS/NTF/9/10/11 and TATA Innovation (DBT, GOI) fellowship to M.O.). Syed Mohd Faisal is thankful to the Department of Biotechnology, Govt. of India for providing him a DBT-SRF Fellowship.

Author Contributions

M.O., S.M.F. and S.Z. conceived and designed the experiments. S.M.F., M.A.R., M.S.U., P.P. and A.A. performed the experiments. M.A. performed the histopathological analysis. S.M.F., M.K., A.A.M., M.A.R. and N.A. analyzed the data, M.O. and S.Z. contributed reagents/materials/analysis tools and S.M.F. wrote the first draft of the manuscript.

Additional Information

Supplementary information accompanies this paper at <https://doi.org/10.1038/s41598-019-48180-7>.

Competing Interests: The authors declare no competing interests.

Publisher's note: Springer Nature remains neutral with regard to jurisdictional claims in published maps and institutional affiliations.



Open Access This article is licensed under a Creative Commons Attribution 4.0 International License, which permits use, sharing, adaptation, distribution and reproduction in any medium or format, as long as you give appropriate credit to the original author(s) and the source, provide a link to the Creative Commons license, and indicate if changes were made. The images or other third party material in this article are included in the article's Creative Commons license, unless indicated otherwise in a credit line to the material. If material is not included in the article's Creative Commons license and your intended use is not permitted by statutory regulation or exceeds the permitted use, you will need to obtain permission directly from the copyright holder. To view a copy of this license, visit <http://creativecommons.org/licenses/by/4.0/>.

© The Author(s) 2019